QUANTIFYING FATIGUE CRACK DAMAGE IN POLYETHYLENE TIBIAL INSERTS OF PROSTHETIC KNEE JOINTS

by

Carly Anne Lockard

A thesis submitted to the faculty of
The University of Utah
in partial fulfillment of the requirements for the degree of

Master of Science

Department of Mechanical Engineering

The University of Utah

May 2015

The University of Utah Graduate School

STATEMENT OF THESIS APPROVAL

The thesis of **Carly Anne Lockard**

has been approved by the following supervisory committee members:

Bart Raeymaekers, Chair **Dec. 19, 2014**
Date Approved

Brittany Coats, Member **Nov. 17, 2014**
Date Approved

Andrew Merryweather, Member **Nov. 17, 2014**
Date Approved

and by **Tim Ameel**, Chair/Dean of

the Department/College/School of **Mechanical Engineering**

and by David B. Kieda, Dean of The Graduate School.

ABSTRACT

Total knee arthroplasty (TKA) is the gold-standard treatment for degenerative and arthritic knee diseases. TKA replaces the damaged knee articular surfaces with a prosthetic knee joint composed of a metal femoral component and polyethylene tibial insert. In 2013, approximately 650,000 primary TKA procedures were performed in the U.S., with approximately 10% requiring revision surgery necessitated by the 10 – 15 years limited lifetime of the prosthetic knee joint. A major limiting factor to the longevity of a prosthetic knee joint is fatigue crack damage of the tibial insert. The objective of this work is to address the problem of fatigue crack damage through: (1) experimentally quantifying fatigue crack damage in polyethylene tibial inserts and (2) predicting fatigue crack damage through finite element modeling.

We have developed a novel subsurface fatigue crack damage measurement method based on specimen transillumination and used this method to measure fatigue crack damage in two tibial inserts. We have also developed a dynamic finite element simulation of the stress in the tibial insert under knee simulator wear test conditions, for an entire gait cycle. Two polyethylene material models, linear elastic and linear viscoelastic, were compared. It was observed that choice of material model has a substantial effect on the maximum von Mises stress. The location of maximum von Mises, principal, and shear stress in the tibial insert were compared to the experimentally measured fatigue crack damage to determine whether the simulation accurately predicts fatigue crack damage in the tibial insert. It was observed that the von Mises stress alone is a poor predictor of fatigue crack damage, while the locations of maximum tensile principal stress and shear stress correspond closely to the locations where fatigue crack damage occurred.

TABLE OF CONTENTS

CHAPTERS

APPENDICES

LIST OF TABLES

Tables

ACKNOWLEDGEMENTS

I would like to thank Dr. Bart Raeymaekers for guiding and challenging me throughout the research process and for patiently providing feedback and direction during the writing of this thesis. I would also like to thank my other committee members, Dr. Andrew Merryweather and Dr. Brittany Coats, for sharing their expertise and giving valuable feedback.

Special thanks to Dr. Coats and the members of the Pediatric Injury Biomechanics Lab for their generosity in allowing me to use the lab's Abaqus license and providing guidance in implementation and interpretation. I would also like to thank Dr. Tony Sanders for sharing his knowledge of orthopaedic implants and knee simulator testing, as well as for his assistance in obtaining images of the knee simulator for this thesis.

Finally, thank you to my husband for his endless patience and support over the last two and a half years, to my sister for always finding ways to make me laugh during times of stress, and to my fellow graduate students and friends here at the U for the much appreciated advice and moral support.

CHAPTER 1

INTRODUCTION

1.1 Significance and Motivation

Total knee arthroplasty (TKA) is the current gold-standard surgical treatment for degenerative [1–3] and rheumatologic knee diseases [2,3]. During a primary TKA the damaged joint surfaces of the knee are replaced with a prosthetic knee joint that replaces the function of the natural joint [2,3]. A prosthetic knee joint typically comprises a metal femoral component that is attached to the femur and articulates with a polyethylene tibial insert, which is constrained in a metal tibial plateau that is anchored in the tibia (see also section 1.2). When a prosthetic knee joint wears out, a revision TKA is performed to replace the original prosthetic knee joint with a new one. Approximately 650,000 primary TKA procedures and 63,000 revision TKA procedures are performed annually (2008 data) in the United States [4]. This represents more than $9 billion in annual health care cost [1]. The number of procedures per year has increased at a compound annual growth rate of approximately 8% [5]. This increased demand for prosthetic knee joints is driven by growth of the over-65 [6,7] and obese populations [1,7], both of which experience increased incidence of osteoarthritis compared to the general population [7]. Additionally, increased demand for prosthetic knee joints from younger, high-activity patients exists [1,7,8], who place high strain on their prosthetic knee joints compared to low-activity patients, and are more likely to require revision TKA [3,6,8–10].

The longevity of prosthetic knee joints extends typically between 10-15 years of use [11,12]. Longevity is oftentimes expressed as statistical survivorship, i.e., the fraction of a population of implants that is still in use after a certain time. It is well documented that the statistical survivorship of prosthetic knee joints declines dramatically after 15 years of use [13–18]. Figure 1.1 shows the primary causes of prosthetic knee joint failure, which include aseptic loosening where bone tissue death from factors not related to infection leads to loosening at the implant-bone interface, instability, infection, polyethylene wear, arthrofibrosis (fibrous tissue growth in and around the joint), and malalignment [19]. Damage to the polyethylene component creates biologically active wear debris that may be absorbed in the bone tissue around the implant, which weakens the bone (osteolysis) and may over time result in aseptic loosening of the metal components [11,20,21]. It also results in accelerated deterioration of the prosthetic joint and may alter the prosthetic knee joint kinematics [22,23]. Failure of the metal components themselves is primarily due to malalignment during surgery and is much less common than failure of the metal component-bone interface by aseptic loosening [19]. Occasional failure of metal components due to fatigue fracture have been reported, but occurrence is also very low (0.5 to 3.3% for femoral components [22,24–28] and for tibial plateaus [29]). Metal components may also experience corrosion, which impacts smooth joint operation and increases the likelihood of arthrofibrosis [30]. From Figure 1.1 we observe that polyethylene wear and aseptic loosening that results from polyethylene wear, contribute to approximately 40% of the total failure incidence [19,31]. Thus, wear of the polyethylene tibial insert is the main cause of prosthetic knee joint failure [3] and reducing wear of the tibial insert could substantially increase prosthetic knee joint longevity. Presently, prosthetic knee joints have an increased probability of failure after 15 years of use, with statistical survivorship declining to between 95% [14] and 80% [13,14] after 15 years of use and to between 90% [14] and < 80% after 20 years of use [15]. The average TKA patient in the US is approximately 65 years of age [32] with a life expectancy of approximately 80 years [33]. This means that the average patient has a significant likelihood of undergoing risky and costly revision surgery [34]. Patients who undergo TKA at less than 60 years of age experience an even higher risk of TKA failure [14], with 15 year survivorship ranging between

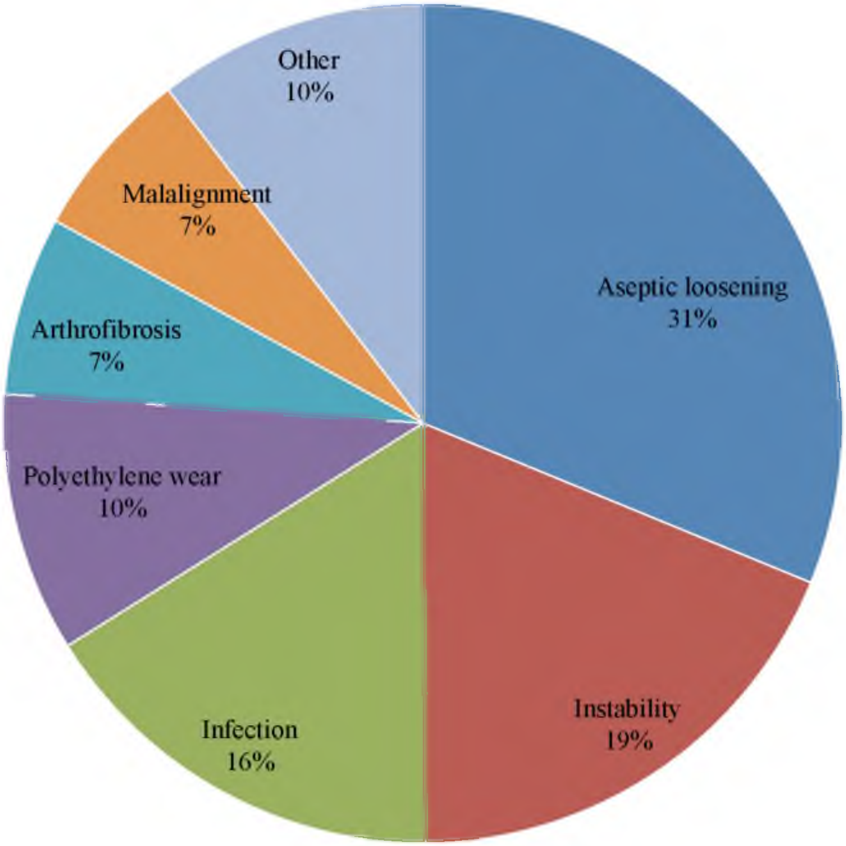

Figure 1.1: Failure modes of prosthetic knee joints (Data obtained from [19]).

approximately 70% and 85% [16,34]. Figure 1.2 shows the breakdown of TKA patient age ranges, illustrating the large portion (43%) of TKA patients who are under the age of 65. Note that TKA under the age of 44 is mostly related to trauma, rather than degenerative or rheumatologic diseases. As the fraction of TKA patients in the age cohort under 65 increases, the incidence of failure and revision surgery is also expected to rise [6]. Revision surgery commonly results in additional bone loss, postoperative pain, activity restriction during the recovery period, and poses a risk of infection [5,35]. In addition, revision surgery represents a significant healthcare cost, with an economic impact often exceeding that of the original TKA procedure [5]. Presently, the incidence of revision for primary TKA is between 5% and 9% for all primary TKA procedures [36]. The combined effects of an increasing number of primary TKA procedures per year and the predicted increase in the percentage of procedures that require

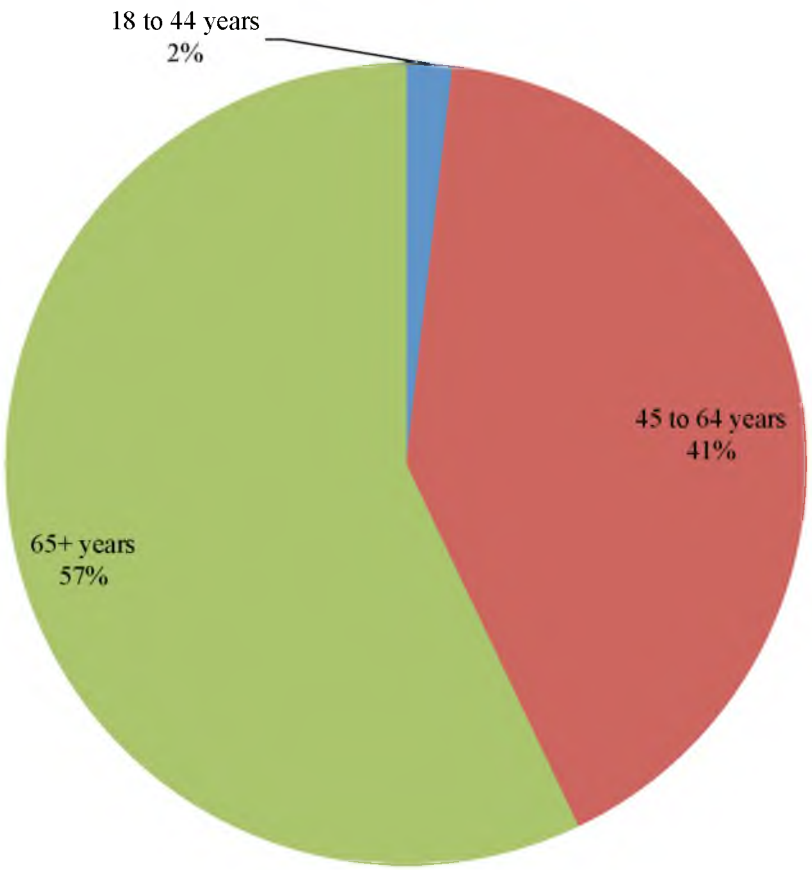

Figure 1.2: Prosthetic knee joint recipients aged 18 and older, broken down by age range (Data obtained from [1]).

revision means that revision surgery costs will grow more burdensome unless prosthetic knee longevity can be increased. Since polyethylene wear of the tibial insert is the main cause of prosthetic knee joint failure, this area represents the greatest potential for improving prosthetic knee joint longevity. The work described in this thesis addresses one specific mode of polyethylene wear (subsurface fatigue crack formation) by relating results from experimental wear testing of prosthetic knee joint components to simulated stresses in the same components.

1.2 Terminology

The purpose of TKA is to replace the damaged natural articular surfaces in the knee with artificial components, and restore the function of the damaged knee joint. In a healthy knee, articular cartilage covers the articulating surfaces of the knee joint [37]. These articulating surfaces include the three separate joints of the knee, which are the femoropatellar joint between the femur and patella and the two tibiofemoral joints (medial and lateral) between the condyles and menisci of the tibia and the condyles of the femur [37]. Although TKA typically involves all three joints, including replacement of the patellar, femoral, and tibial surfaces, the tibiofemoral joint is the primary joint of interest when looking at damage to the tibial insert of the prosthetic knee joint. Figure 1.3 shows a schematic of the anatomy of the human knee joint.

Articular cartilage covers the contacting surfaces of the tibiofemoral joint of the knee. The articulating surfaces include the medial and lateral condyles of the femur and the corresponding condyles and menisci of the tibia [37]. Articular cartilage consists of a thin (< 1 mm to 7 mm) layer of smooth hyaline cartilage that covers the opposing bone surfaces [37,38]. This cartilage serves to cushion the joints [37], distribute load over the joint surfaces to reduce contact stresses [38] and to minimize friction between the articulating surfaces [38]. Figure 1.3 also shows the medial and lateral menisci that cover the tibial condyles. The menisci are composed of fibrocartilage, a fibrous, highly compressible variety of cartilage, and serve to stabilize and cushion the tibiofemoral joint [37]. Figure 1.4 shows schematically a before and after view of the knee subject to TKA. Figure 1.4 A shows the natural knee joint, while Figure 1.4 B shows the same knee joint after TKA.

The most common type of prosthetic knee joint consists of a metal femoral component, typically a cobalt chromium (CoCr) alloy, which articulates with a polyethylene component [39,40]. Figure 1.5 shows these articulating surfaces. The polyethylene articulating surface is joined to the tibia either directly or via a tibial plate, which provides a metal backing for the polyethylene component [41]. The polyethylene component or its metal backing plate is secured to the tibia. This component-bone attachment is accomplished using bone cement fixation [42,43], bony ingrowth [43], and/or mechanical fixation such as screws or stems that extend into the surrounding bone [43].

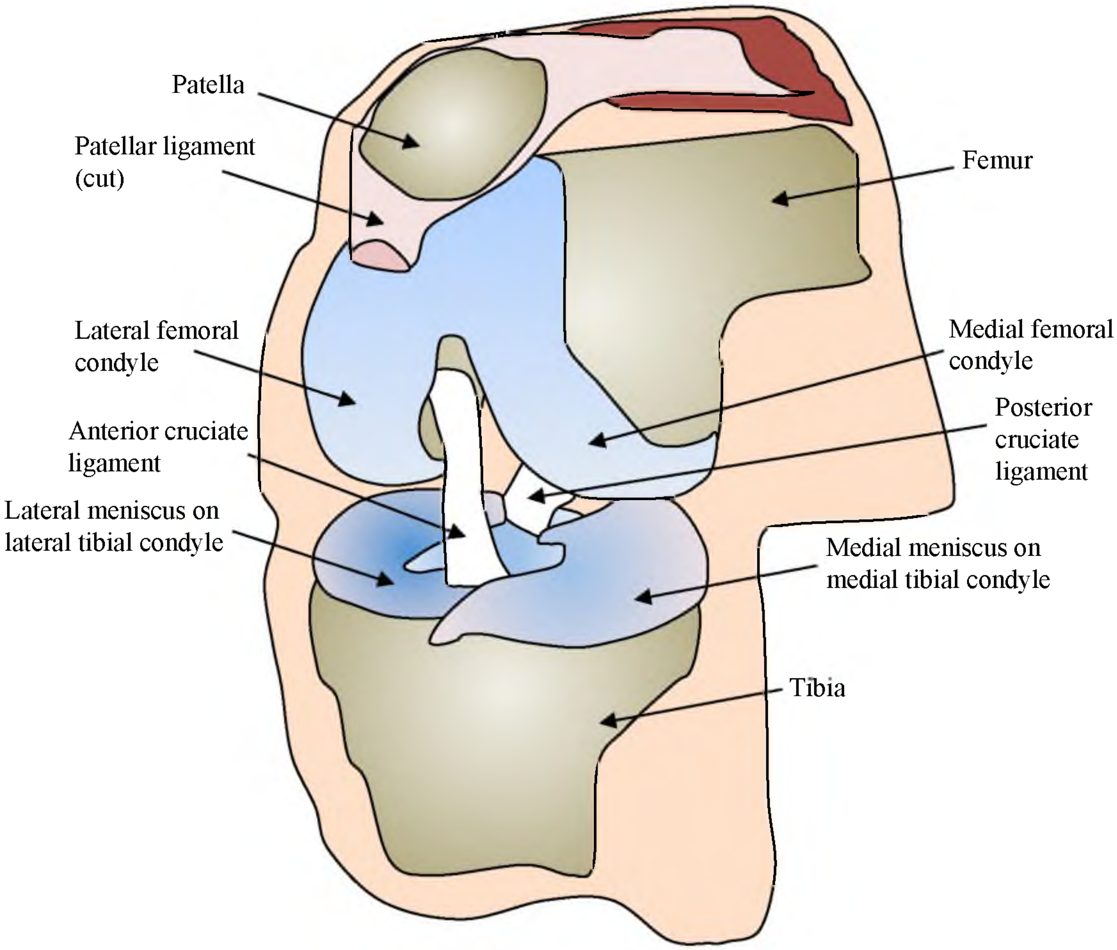

Figure 1.3: Anatomy of the (right) knee with emphasis on the tibiofemoral joint.

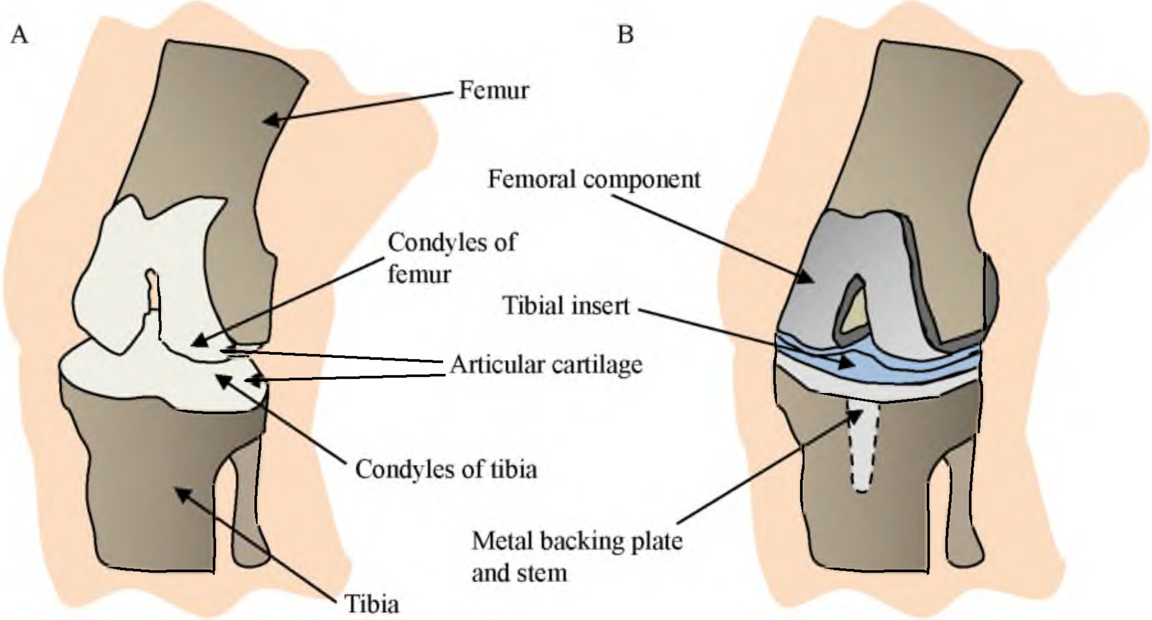

Figure 1.4: Left knee joint and the relevant anatomy (A) before and (B) after total knee arthroplasty.

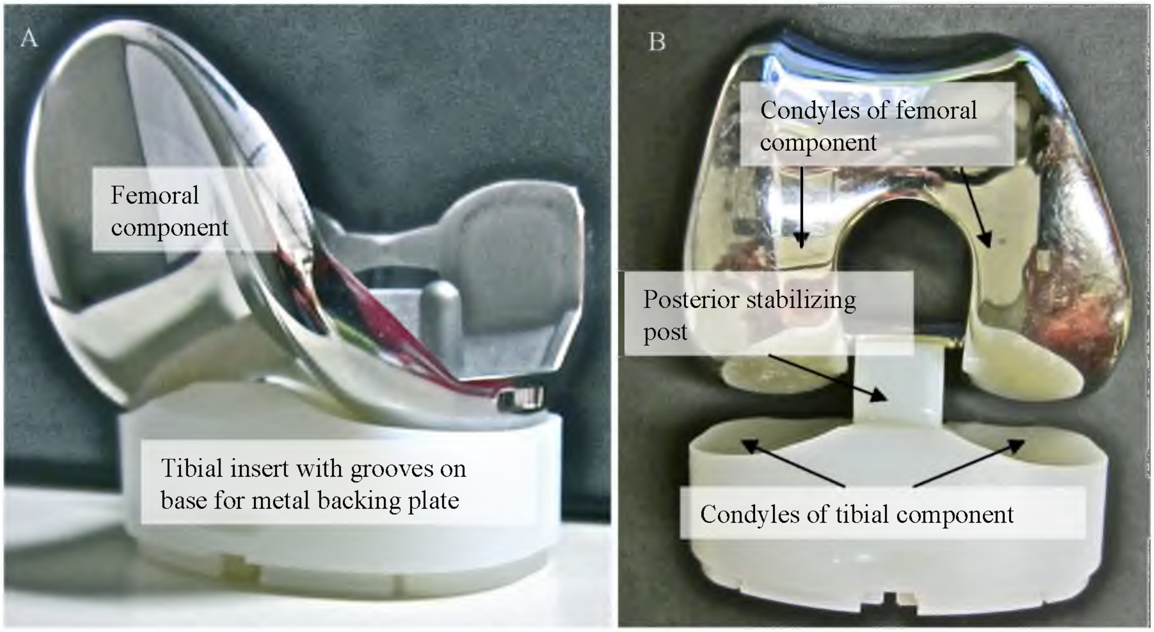

Figure 1.5: TKA components for a right knee. (A) Isometric view of components in anatomically neutral position, i.e., joint position assumed when standing with no flexion, hyperextension, or rotation of the knee. (B) Anterior view of components in position of femoral flexion and distraction to expose the articular surfaces.

1.3 Knee Biomechanics

The biomechanics of the prosthetic knee joint are important for describing the environment of kinetics and kinematics to which the prosthetic knee joint is exposed. Figure 1.6 illustrates the six degrees of freedom at the tibiofemoral joint of the prosthetic knee [37,38], including 1) flexion-extension rotation, 2) internal-external rotation, 3) anterior-posterior translation, 4) medial-lateral translation, 5) varus-valgus rotation, and 6) compression-distraction translation. Figure 1.6 shows these degrees of freedom with senses of each degree of freedom oriented appropriately for a left prosthetic knee joint. During walking gait the tibiofemoral joint

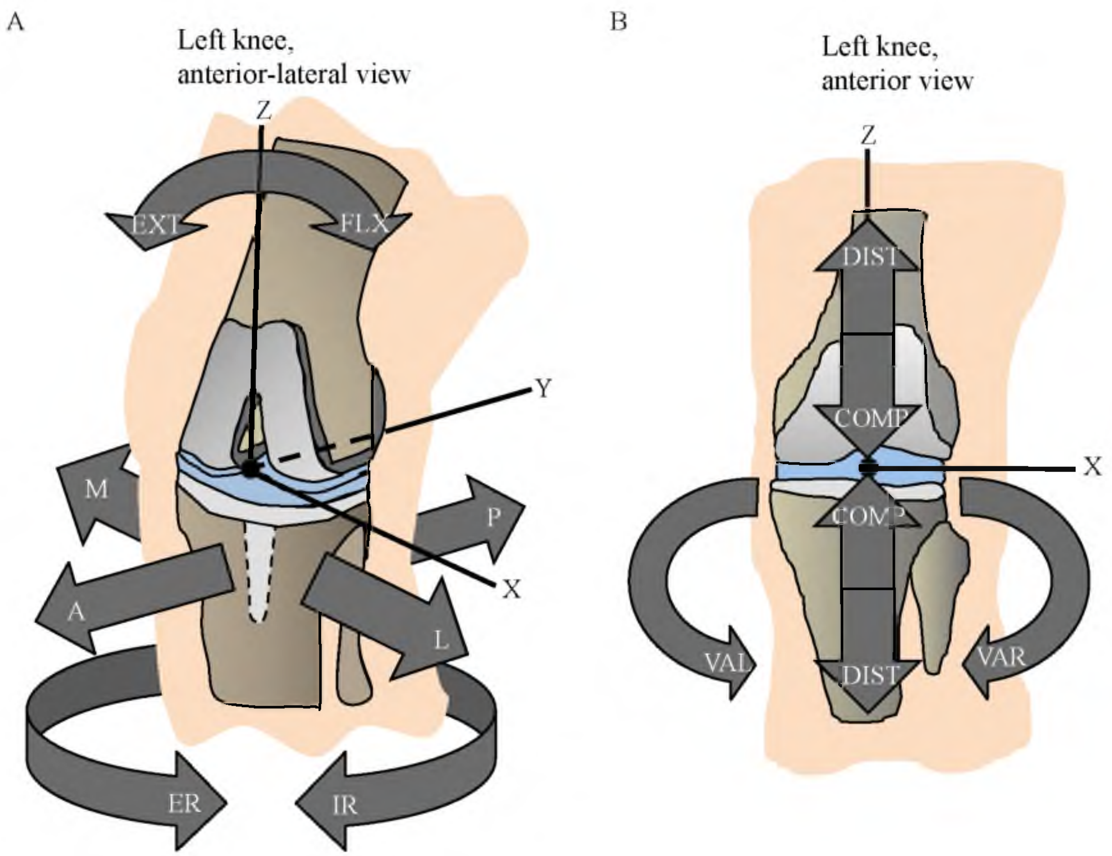

Figure 1.6: Degrees of freedom of a (left) prosthetic knee joint. (A) Isometric view of the left prosthetic knee joint. The degree of freedom designations are as follows: A (anterior), P (posterior), M (medial), L (lateral), ER (external rotation), IR (internal rotation), EXT (extension), and FLEX (flexion). (B) Anterior view of the left prosthetic knee joint. The degree of freedom designations are as follows: DIST (distraction), COMP (compression), VAR (varus rotation of tibia), VAL (valgus rotation of tibia.)

of the knee moves primarily in flexion and extension [37]. Figure 1.7 shows a sagittal (side) view of the right leg during a full gait cycle from heel strike to heel strike. This sagittal view illustrates the flexion and extension of the knee joint during each phase of the gait cycle. Although flexion and extension are the most visible knee motions during gait, the true action of the knee is actually much more complex, involving motion in all six degrees of freedom [38].

The noticeable flexion and extension action that occurs during gait is accompanied by a small but significant internal-external rotation [38]. Specifically, the tibia rotates internally relative to the femur during flexion of the tibiofemoral joint and rotates externally relative to the femur during extension of the tibiofemoral joint [38]. This action occurs about the z-axis shown in Figure 1.6. In the stance phase of the gait cycle when the foot of the right leg is in contact with the ground, the majority of this rotation takes place as rotation of the femur since the rotation of the tibia is constrained by the planted foot [38]. The opposite occurs during the swing phase when the foot of the right leg is not planted [38]. In either case the internal-external rotation is described as tibial motion relative to the stationary femoral reference coordinate system of Figure 1.6. This convention will be used in describing all motions other than flexion-extension, which is described as femoral motion in reference to the tibial coordinate system, from this point forward.

Flexion and extension at the tibiofemoral joint is also accompanied by relative anterior-posterior displacement of the condyles through a combination of rolling and sliding tibiofemoral contact [38]. The contact point between the femoral component and tibial insert moves posterior anterior (and vice versa) approximately 40% of the length of the tibial plateau, over the entire range of flexion and extension [38]. The amount of anterior-posterior displacement is typically greater for the lateral condyle than for the medial condyle [38] due to the internal-external rotation of the knee. Part of the anterior-posterior displacement of the contact point is due to a rolling contact motion created by the flexion-extension rotation, while the remainder is accomplished via anterior-posterior sliding contact. The specific amount of rolling and sliding is dependent on individual knee biomechanics and the degree of condylar congruency between the

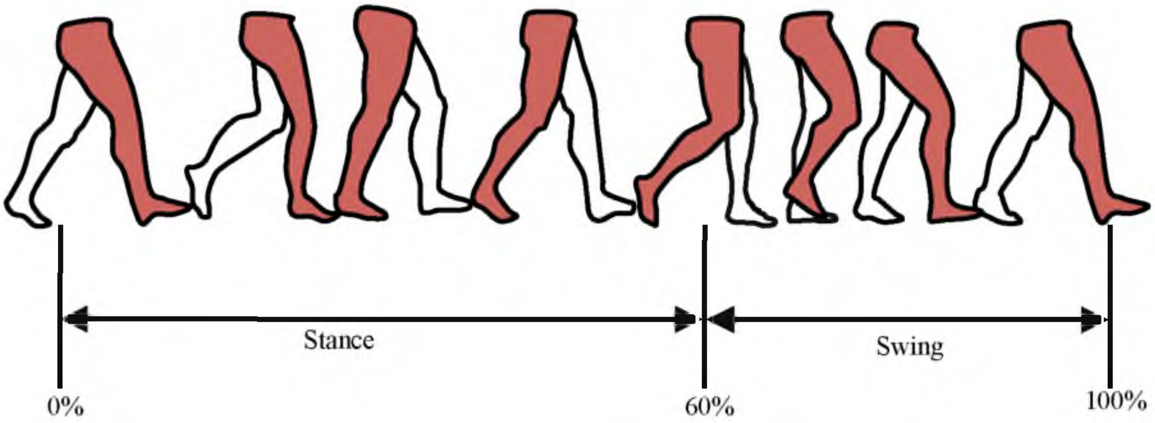

Figure 1.7: Walking gait cycle. Phases and percent of cycle refer to right leg (shaded).

tibial and femoral TKA components [44,45]. It is relevant to tibial insert damage because sliding contact tends to cause more severe wear than rolling contact [45].

Knee kinetics, or forces acting on the knee, also play an important role in the performance of prosthetic knee joints. During routine daily activities a knee joint will experience forces of up to seven times a person's bodyweight [45,46]. The contact stress between the articulating surfaces is minimized through distribution of the forces over the highly congruous menisci and cartilage coatings of the articular surfaces [26]. However, the contact area of the tibiofemoral joint decreases from approximately 765 - 1150 mm^2 in a natural knee joint to approximately 80 – 300 mm^2 in a prosthetic knee joint [47], which increases the contact stress in a prosthetic knee compared to in a natural knee joint.

Peak contact stresses in prosthetic knee joints have been calculated to range between 30 and 60 MPa, exceeding the yield strengths of most polyethylene formulations, which are documented to range between 13 and 32 MPa [47]. The specific forces acting at the knee will be discussed in Chapter 2.

1.4 Polyethylene Wear

The tibial insert is prone to the four basic wear mechanisms: 1) adhesive wear, 2) abrasive wear, 3) oxidative wear and 4) fatigue crack damage [30]. Adhesive wear is defined as wear in which material is transferred from the tibial insert surface to the femoral component [30]. During sliding contact, the polyethylene asperities deform plastically and create asperity junctions, or adhesions, between the tibial insert and the femoral component. The junction material is then pulled off of the tibial insert and adheres to the femoral component [48]. The transferred material may remain attached to the femoral component, detach as loose wear particles, or transfer back onto the tibial insert [49]. In abrasive wear, asperities on the femoral component cause plastic deformation of the tibial insert, creating grooves (ploughing) and removing polyethylene material [30,48,50]. This removed material can then create further abrasive damage via third-body wear [48]. Oxidative wear typically refers to the degradation of the polyethylene tibial insert as a result of oxygen bonding with free radicals. Fatigue wear involves periods of alternating loading and unloading, such as those occurring in the knee joint during gait, which may result in the formation of subsurface cracks that eventually lead to wear particles being formed [30]. It is this last wear mechanism that is of particular interest in this thesis.

Tibial inserts traditionally consist of ultra-high molecular weight polyethylene (UHMWPE) [51], which was introduced for use in orthopaedic implants in 1962 [52]. The introduction of cross-linked and highly cross-linked UHMWPE [53–55] has improved the adhesive and abrasive wear resistance of joint replacement components [55,56]. To create molecular cross-linking the UHMWPE is irradiated with gamma rays, which causes some of the bonds in the chain-like polymer molecules to break [51]. These broken bonds result in the formation of radicals, or highly reactive atoms and molecules with unpaired valence electrons. The two main types produced by UHMWPE irradiation with gamma rays are H radicals, where a carbon-hydrogen bond is broken on the side of a polymer molecule, and macroradicals, where a polymer molecule is split into two or more separate molecules [51]. The radicals covalently bond to the radicals of adjacent polymer molecules to form the namesake cross-links [51]. In addition, radicals can also interact with oxygen to damage the UHMWPE molecules, which results in oxidation of the UHMWPE [51]. Cross-linking results in branched polymer molecules with high molecular weights and improved resistance to plastic deformation at the articulating surface [57,58]. This in turn reduces the material's susceptibility to adhesive and abrasive wear [59,60].

However, several reports document that the fatigue resistance of cross-linked UHMWPE is reduced compared to noncross-linked UHMWPE [53,56,61–72]. This reduced fatigue resistance is especially critical in prosthetic knee joints due to the high cyclic stresses experienced in the knee joint during gait [56]. Most recently vitamin E-blended and cross-linked UHMWPE has been introduced in commercial prosthetic knee joints to reduce long-term oxidative damage to the tibial insert [73]. Oxidation reduces the fatigue resistance of UHMWPE through the destructive interaction between free radicals and the UHMWPE molecules [73], reducing tensile strength, ductility, and toughness [73,74]. Vitamin E, an antioxidant, neutralized free radicals, thereby reducing oxidation and deterioration of the fatigue resistance of the material [73,75].

1.5 Objective

Although the use of vitamin E has been found to reduce the fatigue resistance degradation occurring in cross-linked UHMWPE [73], fatigue wear remains a challenge to tibial insert longevity. The increased emphasis on fatigue cracking as a failure mechanism due to the development of cross-linked UHMWPE and fatigue crack wear's potential for producing severe tibial insert damage highlights the importance of studying fatigue crack wear in UHMWPE tibial inserts. The work described in this thesis addresses the problem of fatigue crack wear by focus on quantification and prediction of fatigue cracking. Specifically, the objectives of this research are: (1) quantification of fatigue crack damage in polyethylene tibial inserts and (2) development of a corresponding finite element model to predict fatigue crack damage.

1.6 References

[1] Losina, E., Thronhill, T. S., Rome, B. N., Wrights, J., and Katz, J. N., 2012, "The dramatic increase in total knee replacement utilization rates in the United States cannot be fully explained by growth in population size and the obesity epidemic," J. Bone Joint Surg. Am., **94**(3), pp. 201–207.

[2] McTighe, T., and Clarke, I., 2009, "Failure mechanism on total knee arthroplasty," Joint Implant Surgery & Research Foundation, Chagrin Falls, OH. [Online]. Available: http://www.jisrf.org/pdfs/failure-mechanism-on-total-knee-arthroplasty.pdf. [Accessed: 7-Mar-2015].

[3] Kasahara, Y., Majima, T., Kimura, S., Nishiike, O., and Uchida, J., 2013, "What are the causes of revision total knee arthroplasty in Japan?" Clin. Orthop., **471**, pp. 1533–1538.

[4] Kurtz, S. M., Ong, K. L., Lau, E., Widmer, M., Maravic, M., Gomez-Barrena, E., de Fatima de Pina, M., Manno, V., Torre, M., Walter, W. L., de Steiger, R., Geesink, R. G. T., Peltola, M., and Roder, C., 2011, "International survey of primary and revision total knee replacement," Int. Orthop., **35**, pp.1783-1789.

[5] Kurtz, S. M., Ong, K. L., Lau, E., Mowat, F., and Halpern, M., 2007, "Projections of primary and revision hip and knee arthroplasty in the United States from 2005 to 2030," J. Bone Jt. Surg., **89-A**(4), pp. 780–785.

[6] Kurtz, S. M., Lau, E., Ong, K., Zhao, K., Kelly, M., and Bozic, K., 2009, "Future young patient demand for primary and revision joint replacement: National projections from 2010 to 2030," Clincal Orthop. Relat. Res., **467**(10), pp. 2606–2612.

[7] Crowninshield, R. D., Rosenberg, A. G., and Sporer, S. M., 2006, "Changing demographics of patients with total joint replacements," Clin. Orthop., **443**, pp. 266–272.

[8] Weinstein, A. M., Rome, B. N., Reichmann, W. A., Collins, J. E., Burbine, S. A., Thornhill, T. S., Wright, J., Katz, J. N., and Losina, E., 2013, "Estimating the burden of total knee replacement in the Unites States," J. Bone Joint Surg. Am., **95**(5), pp. 385–392.

[9] Pabinger, C., Berghold, A., Boehler, N., and Labek, G., 2013, "Revision rates after knee replacement: Cumulative results from worldwide clinical studies versus joint registers," Osteoarthritis Cartilage, **21**, pp. 263–268.

[10] Graichen, H., 2014, "TKA revision - reasons, challenges and solutions," J. Orthop., **11**(1), pp. 1–4.

[11] Fang, H. W., Hsu, S. M., and Sengers, J. V., 2003, NIST Special Publication 1002: Ultra-high Molecular Weight Polyethylene Wear Particle Effects on Bioactivity, National Institute of Standards and Technology, Washington, D.C.

[12] Sharkey, P. F., Hozack, W. J., Rothman, R. H., Shastri, S., and Jacoby, S. M., 2002, "Why are total knee arthroplasties failing today?" Clin. Orthop., **404**, pp. 7–13.

[13] Stiehl, J. B., Hamelynck, K. J., and Voorhorst, P. E., 2006, "International multi-centre survivorship analysis of mobile bearing total knee arthroplasty," Int. Orthop., **30**(3), pp.

190–199.

[14] Heyse, T. J., Ries, M. D., Bellemans, J., Goodman, S. B., Scott, R. D., Wright, T. M., Lipman, J. D., Schwarzkopf, R., and Figgie, M. P., 2014, "Total knee arthroplasty in patients with juvenile idiopathic arthritis," Clin. Orthop., **472**(1), pp. 147–154.

[15] Heyse, T. J., 2013, "Poster #184," American Academy of Orthopaedic Surgeons Annual Meeting, Chicago, IL.

[16] Taylor, J., Rorabeck, C. H., Bourne, R. B., and Inman, K., 2000, "Paper No. 185: Total knee arthroplasty in patients under the age of 50: Long-term follow-up," Program and Abstracts of the 67th Annual Meeting of the American Academy of Orthopaedic Surgeons, Orlando, FL.

[17] Diduch, D. R., Insall, J. N., Scott, W. N., Scuderi, G. R., and Font-Rodriguez, D., 1997, "Total knee replacement in young, active patients. Long-term follow-up and functional outcome," J. Bone Joint Surg. Am., **79**(4), pp. 575–582.

[18] Rodriguez, J. A., Bhende, H., and Ranawat, C. S., 2000, "Paper No. 188. Total condylar knee arthroplasty: A 20 year follow-up study," Program and Abstracts of the 67th Annual Meeting of the American Academy of Orthopaedic Surgeons, Orlando, FL.

[19] Schroer, W. C., Berend, K. R., Lombardi, A. V., Barnes, C. L., Bolognesi, M. P., Berend, M. E., Ritter, M. A., and Nunley, R. M., 2013, "Why are total knee failing today? Etiology of total knee revision in 2010 and 2011," J. Arthroplasty, **28**(Suppl. 1), pp. 116–119.

[20] Gupta, S. K., Chu, A., Ranawat, A. S., Slamin, J., and Ranawat, C. S., 2007, "Review article: Osteolysis after total knee arthroplasty," J. Arthroplasty, **22**(6), pp. 787–799.

[21] Van Kempen, R. W. T. M., Schimmel, J. J. P., van Hellemondt, G. G., Vandenneucker, H., and Wymenga, A. B., 2013, "Reason for revision TKA predicts clinical outcome: Prospective evaluation of 150 consecutive patients with 2-years followup," Clincal Orthop. Relat. Res., **471**, pp. 2296–2302.

[22] Harman, M. K., Banks, S. A., and Hodge, W. A., 2001, "Polyethylene damage and knee kinematics after total knee arthroplasty," Clin. Orthop., **392**, pp. 383–393.

[23] Williams, J. L., Knox, D. A., Teeter, M. G., and Holdsworth, D. W., 2010, "Evidence that in vivo wear damage alters kinematics and contact stresses in a total knee replacement," J. Long. Term Eff. Med. Implants, **20**(1), pp. 43–48.

[24] Cook, S. D., and Thomas, K. A., 1991, "Fatigue failure of noncemented porous-coated implants: A retrieval study," J Bone Jt. Surg Br, **73**(1), pp. 20–24.

[25] Whiteside, L. A., Fosco, D. R., and Brooks Jr, J. G., 1993, "Fracture of the femoral component in cementless total knee arthroplasty," Clin. Orthop., (286), pp. 71–77.

[26] Wada, M., Imura, S., Bo, A., Baba, H., and Miyazaki, T., 1997, "Stress fracture of the femoral component in total knee replacement: A report of 3 cases," Int. Orthop., **21**(1), pp. 54–55.

[27] Swarts, E., Miller, S. J., Keogh, C. V., Lim, G., and Beaver, R. J., 2001, "Fractured Whiteside Ortholoc II knee components," J. Arthroplasty, **16**(7), pp. 927–934.

[28] Saito, S., Tokuhashi, Y., Ishii, T., Mori, S., Hosaka, K., Ryu, K., and Suzuki, G., 2011, "Bilateral fatigue fracture of the femoral components in a cruciate-retaining cementless total knee prosthesis," Orthopedics, **34**(10), pp. e688–e691.

[29] Clarke, H. D., and Trousdale, R. T., 1999, "Component fracture in total knee arthroplasty," The Knee, **6**(4), pp. 261–267.

[30] Hallab, N. J., Jacobs, J. J., and Katz, J. L., 2004, "Orthopaedic Applications," Biomaterials Science: An Introduction to Materials in Medicine, Ratner, B. D., Hoffman, A. S., Schoen, F. J., and Lemons, J. E., eds., Elsevier Academic Press, San Diego, CA, pp. 527–555.

[31] Hossain, F., Patel, S., and Haddad, F. S., 2010, "Midterm assessment of causes and results of revision total knee arthroplasty," Clin. Orthop. Relat. Res., **468**, pp. 1221–1228.

[32] Porucznik, M. A., 2012, "Online extra: TKA in younger patients: It's happening, but is it reasonable?" AAOS Now, **6**(4), 1-5.

[33] OECD, Health at a Glance 2013: OECD Indicators, OECD Publishing.

[34] Vessely, M. B., Whaley, A. L., Harmsen, W. S., Schleck, C. D., and Berry, D. J., 2006, "The Chitranjan Ranawat Award: Long-term survivorship and failure modes of 1000 cemented condylar total knee arthroplasties," Clin. Orthop., **452**, pp. 28–34.

[35] Oduwole, K., Molony, D. C., Walls, R. J., Bashir, S. P., and Mulhall, K. J., 2010, "Increasing financial burden of revision total knee arthroplasty," Knee Surg. Sports Traumatol. Arthrosc., **18**(7), pp. 945–949.

[36] Taylor, M., Bryan, R., and Galloway, F., 2013, "Accounting for patient variability in finite element analysis of the intact and implanted hip and knee: A review," Int. J. Numer. Methods Biomed. Eng., **29**, pp. 273–292.

[37] Marieb, E. N., and Hoehn, K., 2007, Human Anatomy & Physiology, Pearson Education, Inc, San Francisco, CA. United States of America.

[38] Hamill, J., and Knutzen, K. M., 2009, Biomechanical Basis of Human Movement, Lippincott Williams & Wilkins, Philadelphia, PA.

[39] Rahaman, M. N., Yao, A., Bal, B. S., Garino, J. P., and Ries, M. D., 2007, "Ceramics for prosthetic hip and knee joint replacement," J. Am. Ceram. Soc., **90**(7), pp. 1965–1988.

[40] Malikian, R., Maruthainar, K., Stammers, J., Wilding, C. P., and Blunn, G. W., 2013, "Four station knee simulator wear testing comparing titanium niobium nitride with cobalt chrome," J. Bioeng. Biomed. Sci., **3**(3), pp. 1–5.

[41] Hyldahl, H., Regner, L., Carlsson, L., Karrholm, J., and Weidenhielm, L., 2005, "All-polyethylene vs. metal-backed tibial component in total knee arthroplasty: A randomized RSA study comparing early fixation of horizontally and completely cemented tibial components," Acta Orthop., **76**(6), pp. 769–777.

[42] Gandhi, R., Tsvetkov, D., Davey, J. R., and Mahomed, N. N., 2009, "Survival and clinical function of cemented and uncemented prostheses in total knee replacement: A meta-analysis," J. Bone Jt. Surg., **91-B**(7), pp. 889–895.

[43] Lombardi Jr, A. V., Berasi, C. C., and Berend, K. R., 2007, "Evolution of tibial fixation in total knee arthroplasty," J. Arthroplasty, **22**(4), pp. 25–29.

[44] Blunn, G. W., Joshi, A., Minns, R. J., Lidgren, L., Lilley, P., Ryd, L., Engelbrecht, E., and Walker, P. S., 1997, "Wear in retrieved condylar knee arthroplasties: A comparison of wear in different designs of 280 retrieved condylar knee prostheses," J. Arthroplasty, **12**(3), pp. 281–290.

[45] Blunn, G. W., Walker, P. S., Joshi, A., and Hardinge, K., 1991, "The dominance of cyclic sliding in producing wear in total knee replacements," Clin. Orthop., (274), pp. 253–260.

[46] Currier, J. H., Duda, J. L., Sperling, D. K., Collier, J. P., Currier, B. H., and Kennedy, F. E., 1998, "In vitro simulation of contact fatigue damage found in ultra-high molecular weight polyethylene components of knee prostheses," Proc. Inst. Mech. Eng. Part H, **212**, pp. 293–302.

[47] D'Lima, D. D., Steklov, N., Fregly, B. J., Banks, S. A., and Colwell Jr., C. W., 2008, "In vivo contact stresses during activities of daily living after knee arthroplasty," J. Orthop. Res., **26**, pp. 1549–1555.

[48] Rabinowicz, E., 1995, Friction and Wear of Materials, Wiley, New York.

[49] Cruse, T. A., 1997, Reliability-Based Mechanical Design, Marcel Dekker, Inc., New York, NY.

[50] Gnecco, E., and Meyer, E., eds., 2007, Fundamentals of Friction and Wear, Springer, Berlin.

[51] Kurtz, S. M., ed., 2009, UHMWPE Biomaterial Handbook: Ultra High Molecular Weight Polyethylene in Total Joint Replacement and Medical Devices, Elsevier Academic Press, New York, NY.

[52] Baykal, D., Siskey, R. S., Haider, H., Saikko, V., Ahlroos, T., and Kurtz, S. M., 2014, "Advances in tribological testing of artificial joint biomaterials using multidirectional pin-on-disk testers," J. Mech. Behav. Biomed. Mater., **31**, pp. 117–134.

[53] Atwood, S. A., Van Critters, D. W., Patten, E. W., Furmanski, J., Ries, M. D., and Pruitt, L. A., 2011, "Tradeoffs amongst fatigue, wear, and oxidation resistance of cross-linked ultra-high molecular weight polyethylene," J. Mech. Behav. Biomed. Mater., **4**(7), pp. 1033–1045.

[54] Popoola, O. O., Yao, J. Q., Johnson, T. S., and Blanchard, C. R., 2010, "Wear, delamination, and fatigue resistance of melt-annealed highly crosslinked UHMWPE cruciate-retaining knee inserts under activities of daily living," J. Orthop. Res., **28**, pp. 1120–1126.

[55] Kurtz, S. M., Gawel, H. A., and Patel, J. D., 2011, "History and systematic review of wear

and osteolysis outcomes for first-generation highly crosslinked polyethylene," Clincal Orthop. Relat. Res., **469**(8), pp. 2262–2277.

[56] Simis, K. S., Bistolfi, A., Bellare, A., and Pruitt, L. A., 2006, "The combined effects of crosslinking and high crystallinity on the microstructural and mechanical properties of ultra high molecular weight polyethylene," Biomaterials, **27**, pp. 1688–1694.

[57] Edidin, A. A., Pruitt, L. A., Jewett, C. W., Crane, D. J., Roberts, D., and Kurtz, S. M., 1999, "Plasticity-induced damage layer is a precursor to wear in radiation-cross-linked UHMWPE acetabular components for total hip replacement," J. Arthroplasty, **14**(5), pp. 616–627.

[58] Wang, A., Sun, D. C., Yau, S. S., Edwards, B., Sokol, M., Essner, A., Polineni, V. K., Stark, C., and Dumbleton, J. H., 1997, "Orientation softening in the deformation and wear of ultra-high molecular weight polyethylene," Wear, **203**, pp. 230–241.

[59] Muratoglu, O. K., Bragdon, C. R., O'Connor, D. O., Jasty, M., Harris, W. H., Gul, R., and McGarry, F., 1999, "Unified wear model for highly crosslinked ultra-high molecular weight polyethylenes (UHMWPE)," Biomaterials, **20**(16), pp. 1463–1470.

[60] McKellop, H., Shen. F. W., Lu, B., Campbell, P., and Salovey, R., 1999, "Development of an extremely wear-resistant ultra high molecular weight polyethylene for total hip replacements," J. Orthop. Res., **17**(2), pp. 157–167.

[61] Gencur, Sara J., Rimnac, Clare M., and Kurtz, S.M., 2006, "Fatigue crack propagation resistance of virgin and highly crosslinked thermally treated ultra-high molecular weight polyethylene," Biomaterials, **27**, pp. 1550–1557.

[62] Gomell, A., Wanich, T., and Bellare, A., 2002, "J-integral fracture toughness and tearing modulus measurement of radiation cross-linked UHMWPE," J. Orthop. Res., **20**, pp. 1152–1156.

[63] Oral, E., Malhi, A. S., and Muratoglu, O. K., 2006, "Mechanisms of decrease in fatigue crack propagation resistance in irradiated and melted UHMWPE," Biomaterials, **27**, pp. 917–925.

[64] Kurtz, S. M., Pruitt, L. A., Jewett, C. W., Foulds, J. R., and Edidin, A. A., 1999, "Radiation and chemical crosslinking promote strain hardening behavior and molecular alignment in ultra high molecular weight polyethylene during multi-axial loading conditions," Biomaterials, **20**(16), pp. 1449–1462.

[65] Gencur, S. J., Rimnac, C. M., and Kurtz, S. M., 2003, "Failure micromechanisms during uniaxial tensile fracture of conventional and highly crosslinked ultra-high molecular weight polyethylenes used in total joint replacements," Biomaterials, **24**, pp. 3947–3954.

[66] Gillis, A. M., Schmiegg, J. J., Bhattacharyya, S., and Li, S., 1999, "An independent evaluation of the mechanical, chemical and fracture properties of UHMWPE crosslinked by 34 different conditions," Proceedings of the 45th Annual Meeting of the Orthopaedic Research Society, Anaheim, CA, p. 908.

[67] Baker, D. A., Hastings, R.S., and Pruitt, L. A., 1999, "Study of fatigue resistance of

chemical and radiation crosslinked medical grade ultrahigh molecular weight polyethylene," J. Biomed. Mater. Res., **46**(4), pp. 573–581.

[68] O'Connor, D. O., Muratoglu, O. K., Bragdon, C. R., Lowenstein, J., Jasty, M., and Harris, W. H., 1999, "Wear and high cycle fatigue of highly crosslinked UHMWPE," Transactions of 44th Annual Meeting of the Orthopaedic Research Society, Anaheim, CA, p. 816.

[69] Krzypow, D. J., Bensusan, J., Sevo, K., Haggard, W., Parr, J., Goldberg, V., and Rimnac, C. M., 2000, "The fatigue crack propagation resistance of gamma radiation or peroxide crosslinked UHMW polyethylene," Transactions of Sixth World Biomaterials Congress, HI, p. 382.

[70] Baker, D. A., Hastings, R. S., and Pruitt, L. A., 2000, "Compression and tension fatigue resistance of medical grade ultra high molecular weight polyethylene: The effect of morphology, sterilization, aging and temperature," Polymer, **41**(2), pp. 795–808.

[71] Baker, D. A., Bellare, A., and Pruitt, L. A., 2003, "The effects of degree of crosslinking on the fatigue crack initiation and propagation resistance of orthopedic grade polyethylene," J. Biomed. Mater. Res., **66A**, pp. 146–154.

[72] Duus, L. C., Walsh, H. A., Gillis, A. M., Noisiez, E., and Li, S., 2000, "The effect of resin grade, manufacturing method, and cross linking on the fracture toughness of commercially available UHMWPE," Trans. Orthop. Res. Soc., **25**, p. 544.

[73] Bracco, P., and Oral, E., 2011, "Vitamin E-stabilized UHMWPE for total joint implants: A review," Clin. Orthop., **469**(8), pp. 2286–93.

[74] Kennedy, F. E., Currier, B. H., Van Critters, D. W., Currier, J. H., and Collier, J. P., "Oxidation of ultra-high molecular weight polyethylene and its influence on contact fatigue and pitting of knee bearings," Tribol. Trans., **46**(1), pp. 111–118.

[75] Shibata, N., and Tomita, N., 2005, "The anti-oxidative properties of α-tocopherol in γ-irradiated UHMWPE with respect to fatigue and oxidation resistance," Biomaterials, **26**(29), pp. 5755–5762.

CHAPTER 2

KNEE SIMULATOR WEAR TESTING AND SUBSURFACE CRACK MEASUREMENT

2.1 Background

2.1.1 Fatigue Wear Testing

One of the most severe symptoms of fatigue wear in a prosthetic knee joint is fatigue cracking of the tibial insert. UHMWPE tibial inserts are particularly prone to fatigue crack damage [1–4] when compared to other UHMWPE prosthetic joint components such as acetabular liners [1,2]. Fatigue crack damage is defined as progressive and localized damage resulting from cyclic loading [2]. It initiates as microstructural changes of the material that progress into microscale cracks. These small cracks grow as a result of cyclic loading, eventually coalescing into macroscale cracks [3]. Stable growth of these macroscale cracks proceeds until structural instability or fracture occurs [2]. Fracture of the UHMWPE tibial insert in which a portion of the articulating surface separates from the bulk of the tibial insert is referred to as delamination [5]. The susceptibility of the tibial insert to fatigue crack damage stems from the limited congruency between the articulating surfaces of the different components of the prosthetic knee joint, which creates high contact stress directly beneath the surface of the tibial insert condyles. This, in combination with cyclic loading and sliding contact, induces high cyclic stress in the UHMWPE, which may lead to fracture [1,3].

Fatigue testing of UHMWPE formulations generally takes the form of standard specimen testing, such as cyclic stress or strain tests for stress or strain life and fatigue crack propagation resistance [2] and fatigue punch testing [6]. These standardized tests can be used to determine the fatigue life of specific UHMWPE resins. Fatigue testing and fatigue crack propagation resistance testing can be performed with standard unnotched fatigue specimens and notched fracture specimens, respectively, under cyclic loading [2]. Fatigue punch testing consists of cyclic loading of an UHMWPE specimen in a small punch test apparatus until fracture occurs, to determine the crack propagation resistance [6]. Pin-on-disk wear testing is also used to examine the fatigue wear resistance of UHMWPE using a simplified approximation of the combined sliding and rolling contact that occurs in the prosthetic knee joint in vivo [7]. Results from these three standard fatigue tests can be used to compare fatigue resistance of different UHMWPE resins and treatments such as cross-linking with annealing [8] or vitamin E infusion [9] on fatigue crack propagation resistance. However, because these standard tests ignore the combination of loading and kinematic effects that occurs in vivo, more complex fatigue testing methods have been developed. One widely used, and highly complex, method is knee simulator testing [7]. This method is used to measure polyethylene wear of the tibial insert under simulated walking gait loads, kinematics, and knee joint synovial lubrication [7]. It considers the entire prosthetic knee joint as a system, incorporating the tibial insert, tibial plateau, and femoral component. Knee simulator experiments are most often run at 1 Hz frequency to mimic walking gait [10]. Hence, long duration knee simulator wear experiments covering several million cycles may take months to complete, and are very costly to run.

During walking gait the prosthetic knee is subject to active forces from the muscles acting across the knee joint, passive forces from the connective tissues that constrain knee movement, and ground reaction forces transferred through the leg [11]. In vivo knee loading is extremely complex due to the multiple muscles and connecting ligaments acting across the knee joint. The knee simulator simplifies this complex loading, applying resultant forces in the anterior-posterior and axial directions, and resultant torques in the internal-external and flexion-extension directions [7]. Figure 2.1 shows an anterior-lateral view of a prosthetic knee joint

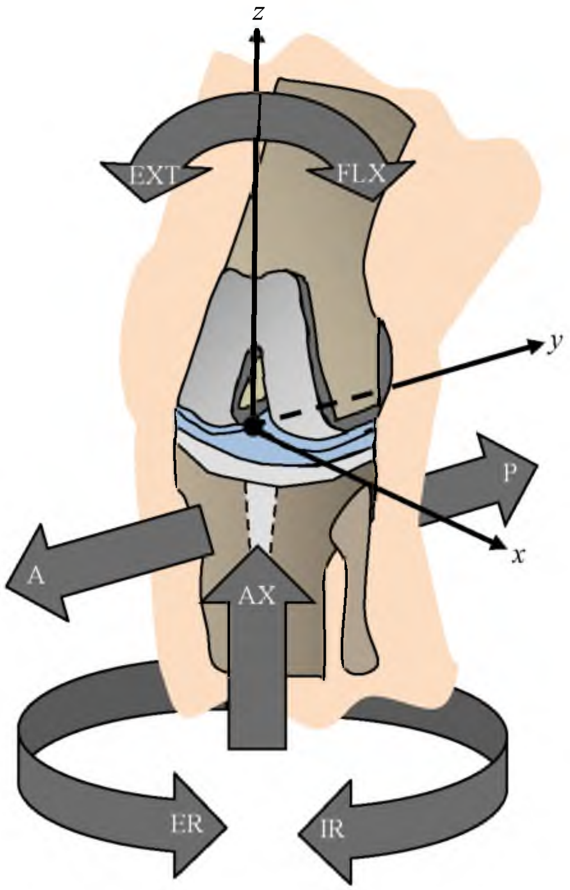

Left knee, anterior-lateral view

Figure 2.1: Anterior-lateral view of a left prosthetic knee joint with the directions of applied forces and torques marked with arrows. A = anterior, P = posterior, AX = axial, ERT = external rotation, IRT = internal rotation, EXT = extension, FLX = flexion.

implanted in a left knee. Figure 2.1 uses arrows to illustrate the four degrees of freedom in which force or displacement actuation is applied. These degrees of freedom are anterior-posterior (A and P), axial (AX), internal-external rotation (IR and ER), and flexion-extension (FLX and EXT) in relation to the left prosthetic knee joint. No displacement is allowed in the medial-lateral degree of freedom, and the varus-valgus degree of freedom is unconstrained. These two degrees of freedom receive no force or displacement actuation from the knee simulator.

In most knee simulators the loading is applied through a combination of pneumatic or hydraulic actuators that mimic muscle actions, and springs that mimic connective tissue constraints [7]. The knee simulator mimics all polyethylene wear modes, and is not restricted to only simulating fatigue crack damage. Typically, adhesive and abrasive wear is measured by the change in mass of the UHMWPE tibial insert before and after the test [10]. Fatigue crack damage resistance is determined by attempting to detect and measure developing fatigue crack damage [12], which is not a straightforward task.

2.1.2 Subsurface Fatigue Crack Damage Measurement in UHMWPE Tibial Inserts

Several researchers have focused on examining and classifying tibial insert wear [1,2,4,5,13–17]. However, few satisfactory methods have been developed for measuring subsurface fatigue crack damage. The measurement of subsurface fatigue cracking in UHMWPE tibial inserts provides valuable information about the development of fatigue crack damage and allows comparison between fatigue crack damage for different prosthetic knee joints. Previous studies of subsurface cracking in UHMWPE tibial inserts have presented primarily qualitative results, failing to precisely measure the area of subsurface fatigue cracks [12,13,18,19]. Existing fatigue crack detection techniques include: 1) freeze fracturing and optical microscopy [18], 2) thin-slice microscopy [20], 3) scanning acoustic tomography (SAT) [21], 4) microscale computed tomography (Micro-CT) [22], and 5) optical microscopy using indirect illumination [13].

Freeze fracturing and optical microscopy involves freeze fracturing fatigue crack specimens to allow optical microscopy examination of the fatigue crack surface. Optical microscopy is a common technique for measuring fatigue crack propagation in notched compact tensile specimens [23] and retrieved prosthetic joint components [18]. Figure 2.2 shows a compact tension specimen after fatigue crack development. Liquid nitrogen is applied to reduce the ductility of the tested material, allowing for brittle fracture of the crack ligament when force is

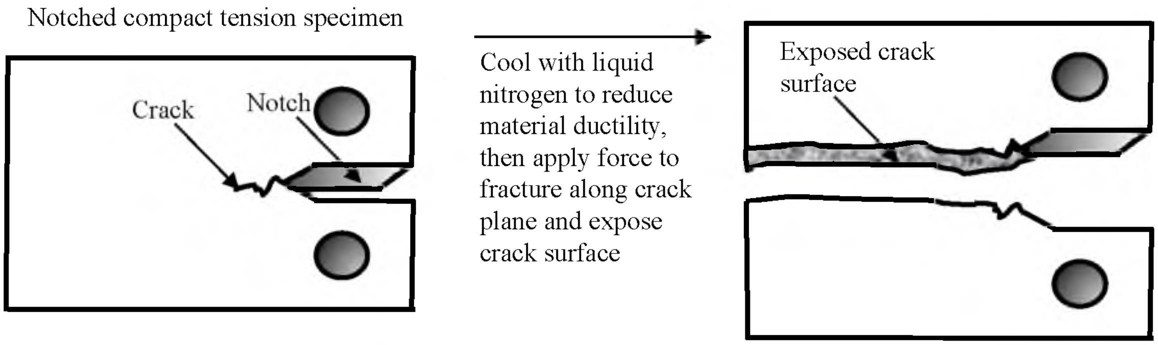

Figure 2.2: Preparation of a fatigue crack specimen for microscopy using freeze fracturing of a compact tension specimen.

applied to the ligament with a sharp instrument and mallet [24]. Freeze fracturing is effective only for cracks that extend to the surface of the specimen, as the crack ligament must be visible for effective force application and fracturing. Additionally, this crack measurement technique is destructive, which is often undesirable when examining fatigue crack growth over time.

Thin-slice microscopy provides the ability to view subsurface crack profiles through the depth of the material via sectioning. Figure 2.3 shows a left tibial insert with a subsurface crack, the cutting plane along which thin slices are obtained, and one resulting slice as viewed under a light microscope. Thin-slice microscopy requires the tibial insert specimen to be sliced extremely thinly. Typically a microtome, a specialized cutting instrument for creating very thin slices of material, is used. For relatively soft material such as UHMWPE the specimen is first cooled with liquid nitrogen to limit deformation during slicing with the microtome [25]. The sections are inspected via dark or light field microscopy. In dark field microscopy the specimen is illuminated through diffraction and cracks in the material are visible as contrasting nonilluminated areas [20]. In light field microscopy the specimen partially blocks the transmitted light, while cracks are visible as fully lit areas [26]. Thin-slice microscopy is superior to surface microscopy because it allows crack length measurement even if the crack has not propagated to the surface. However, this method is also destructive, and the possibility of creating crack artifacts during the slicing process exists.

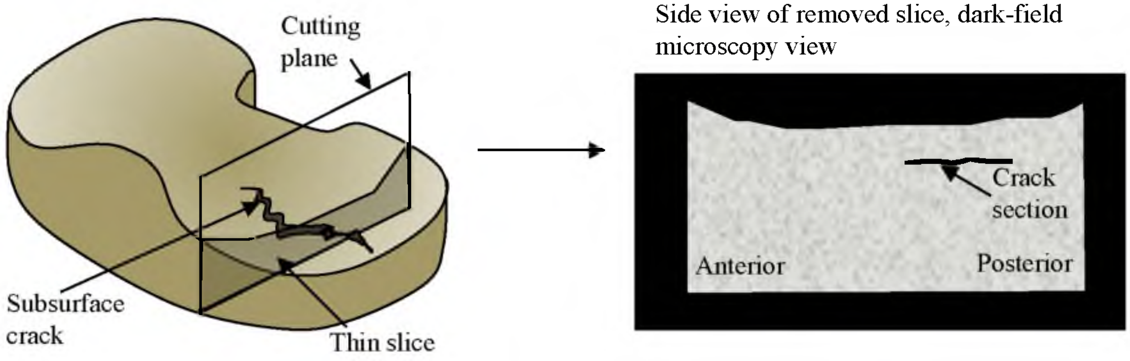

Figure 2.3: Thin-slice microscopy of a left knee tibial insert containing a subsurface crack.

Scanning acoustic tomography (SAT) presents a nondestructive alternative to freeze fracturing and thin-slice microscopy for subsurface crack detection and measurement based on the use of high-frequency acoustic waves to map local differences in acoustic impedance in a specimen [27]. Figure 2.4 shows the positioning of the SAT apparatus relative to an UHMWPE specimen in a water bath and a resulting processed image of the subsurface fatigue cracks. Figure 2.4 illustrates the SAT-technique, which works by transmitting acoustic waves into a specimen and creating an image of cracks within the specimen based on the attenuation and reflection of these waves. The transducer transmits acoustic waves into the specimen material, where they gradually attenuate as they pass through pristine, homogeneous portions of material, which are of constant acoustic impedance. A portion of the acoustic wave is reflected at the interface between regions of different acoustic impedance, as created by voids and cracks [27], thus allowing subsurface cracks to be detected and mapped [21]. SAT can theoretically detect very small cracks, down to voids of 5 nm for air-filled gaps [28]. However, the detectable crack size decreases with sample thickness and varies depending on the material and medium with which the void is filled, as well as the surface roughness of the sample. Practically, any void size smaller than the surface roughness features, such as the roughness produced by adhesive and abrasive wear, cannot be detected [28].

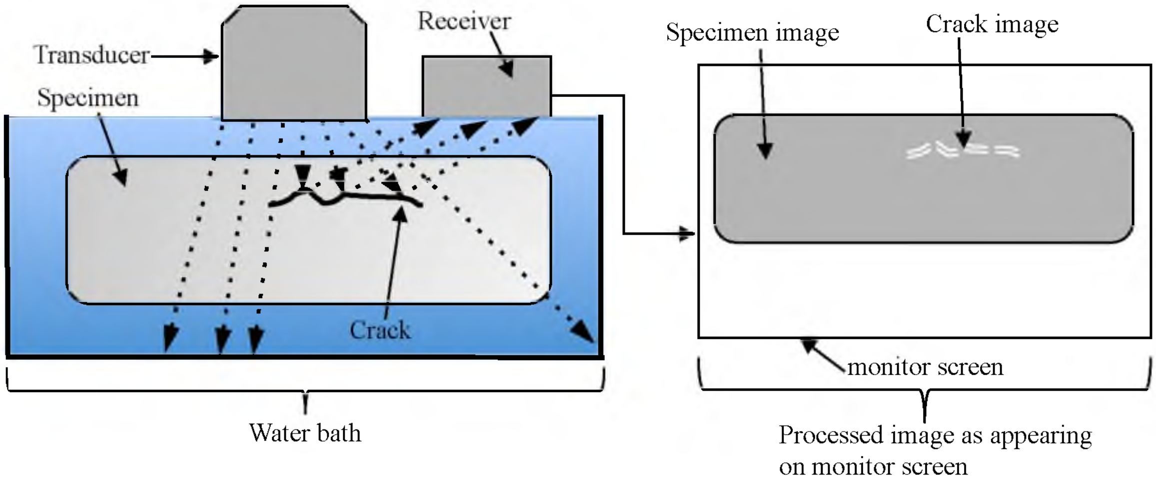

Figure 2.4: SAT of an UHMWPE specimen in a water bath.

With SAT, subsurface cracking can be detected in a nondestructive manner and information about fatigue crack growth as a function of time during knee simulator testing can be obtained [9]. However, due to the resolution constraints related to the surface roughness of the test specimen, the method generally provides low-resolution images and has not yet been successfully employed to quantify the size of subsurface cracks.

Microscale computed-tomography (micro-CT) is another technique for quantitative evaluation of subsurface cracking. The technique uses x-ray scanning of a specimen to obtain sequential thin slice images of the specimen. The information contained in the thin slice images is assembled into a 3D representation of the specimen. Figure 2.5 shows a specimen being scanned with x-rays, the resulting thin-slice images, and the final 3D specimen image. Micro-CT provides high-resolution (sub-1 μm to 100 μm) detection of cracks in three dimensions [29], enabling measurement of crack development even during initial small crack development [22]. Because micro-CT is a 3D imaging technique, it allows measurement of cracks that have propagated into complex 3D shapes. This is particularly advantageous, because subsurface cracks do not necessarily follow any 2D plane inside the tibial insert. However, micro-CT represents a potentially costly procedure, making alternative subsurface crack measurement methods desirable.

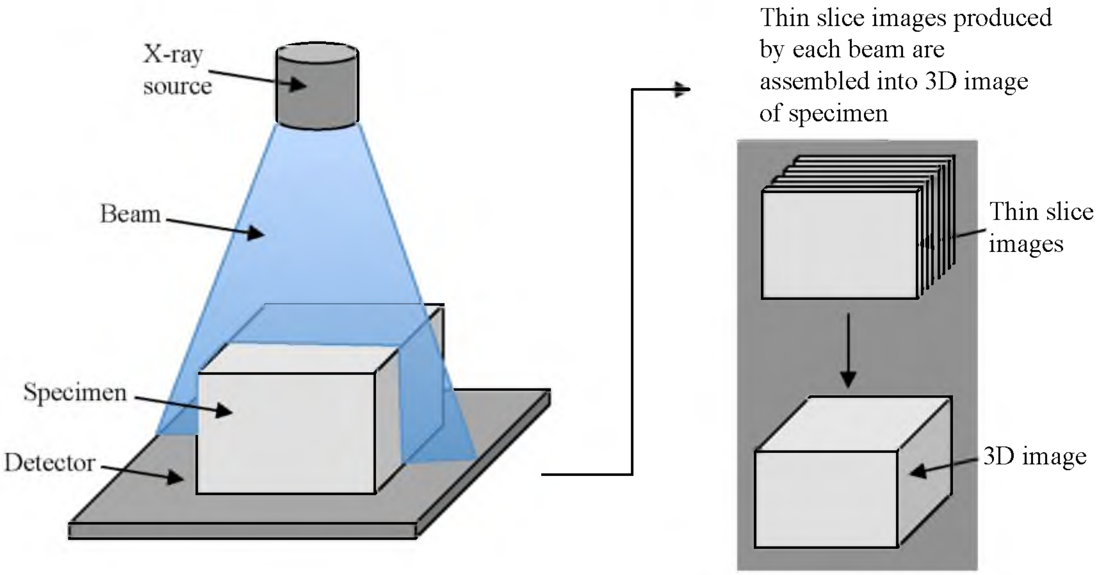

Figure 2.5: Schematic of micro-CT of a specimen showing scanning process and integration of thin slice images into a 3D image of the specimen.

Optical microscopy using indirect illumination allows low cost, nondestructive examination of surface damage and represents a less costly alternative to micro-CT when 3D measurements are unnecessary. This technique uses indirect illumination to enhance visualization of surface damage on a specimen during examination with an optical microscope. Figure 2.6 shows a specimen lit at an oblique angle under a microscope camera and the resulting view of the highlights and shadows created by surface damage features. This method has been combined with image digitization to measure surface damage on UHMWPE tibial inserts [13]. Harman et al. [13] evaluated the articular surfaces of eight retrieved UHMWPE tibial inserts at 10 to 30 times magnification to detect surface damage regions. Using their technique the regions that display superficial damage are then further magnified to between 30 and 174 times magnification under indirect illumination and digital images of the magnified regions are obtained. The damage regions in the digital images are traced following the method used in earlier work by Harman et al. to trace damage on the surface of articular cartilage [30]. This tracing method is accurate within 1 mm for determining the damage area centroid and within 50 mm^2 for measuring the damage area [13]. No information about the depth of the surface damage is provided.

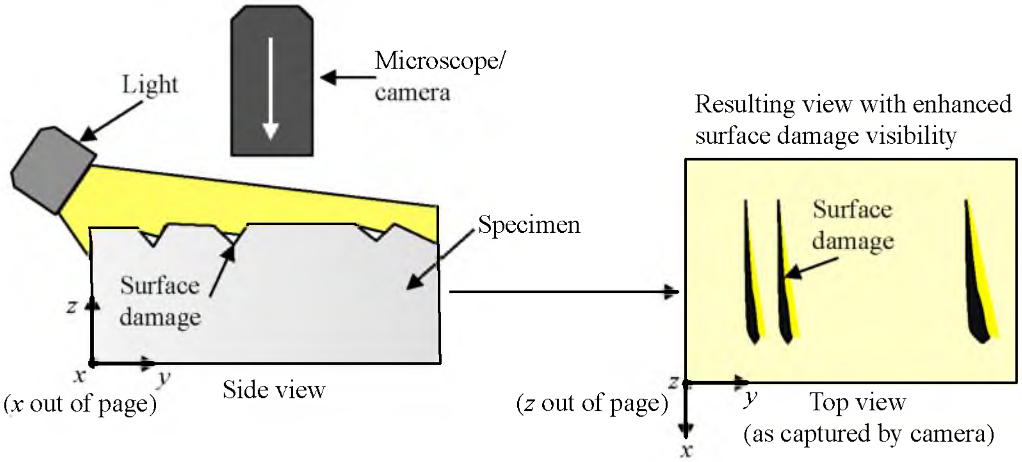

Figure 2.6: Indirect illumination of a specimen surface and resulting view of damage.

The indirect illumination microscopy method has also been used to identify shallow cracks in UHMWPE acetabular liners [18]. Indirect illumination creates enhanced visualization of features, such as a lack of plastic deformation at the feature edges, which distinguish cracks from shallow scratches. Identified cracks can then be more precisely examined via other methods, e.g., scanning electron microscopy [18]. Indirect illumination provides good contrast visualization of surface features such as cracks, scratches, and pitting because light directed towards the test specimen under an oblique angle creates cast shadows and highlights adjacent to raised and indented surface areas [18]. However, it is not effective at enhancing visualization of subsurface fatigue crack damage, due to the lack of raised or indented surface areas.

In this thesis we propose, develop and implement an alternative fatigue crack damage visualization and measurement method. This new method uses transillumination to enhance visualization of subsurface fatigue crack damage, and employs digital imaging and semi-automated area measurement to quantify the size of the detected subsurface cracks. This technique combines the desirable qualities of indirect illumination microscopy, such as cost-effectiveness and simplicity, with the ability to view and measure subsurface fatigue crack damage. This new method differs from previously used methods in its ability to measure subsurface fatigue crack damage nondestructively while using a simple and cost-effective bench-top set-up. Transillumination has been used previously for qualitative illustration of the existence of subsurface cracks [12], but has not been used for the purpose of measuring the size of subsurface cracks. Similarly, digital imaging and image processing have been employed in existing studies for measuring surface damage, but have been limited by reliance on hand-tracing of damage regions [13,19], subjective identification damage [31], and focus on surface damage measurement [19,31,32].

The fatigue crack damage measurement method employed in this work addresses these limitations, allowing precise and objective measurement of subsurface fatigue crack damage areas. Table 2.1 summarizes the advantages and disadvantages of each existing fatigue crack damage measurement method and identifies the advantages of the new transillumination method relative to each existing method.

2.2 Materials and Methods

2.2.1 Overview

We have experimentally mimicked the fatigue crack damage-inducing loading and kinematic conditions in a knee-simulator testing machine. The resulting subsurface fatigue crack damage in the tibial insert is quantified through our novel transillumination and image processing method. We hypothesize that the locations of subsurface fatigue cracking in the tibial insert correspond to the locations that experience the highest mechanical stress magnitudes throughout the knee simulator gait cycle.

To demonstrate the relationship between mechanical stress and subsurface cracking we have implemented a finite element method (FEM) simulation to model the local stress in the tibial insert during articulation with the femoral component through a full gait cycle. We then correlate the locations of maximum stress (model) to the locations of subsurface cracking (experiment).

Table 2.1: Advantages and disadvantages of existing subsurface fatigue crack damage measurement methods and how the new transillumination method addresses each existing method's disadvantages.

Existing subsurface fatigue crack damage measurement method	Main advantages	Main disadvantages	Advantages of the transillumination method
Thin-slice microscopy	• Commonly used	• Destructive • Artifacts created through slicing process	• Nondestructive
SAT	• Nondestructive	• Unable to detect voids smaller than the scale of surface roughness	• Visibility of surface roughness is reduced through transillumination
Micro-CT	• Nondestructive • High resolution • Three-dimensional measurement	• May be cost prohibitive	• Low-cost
Visual methods, including optical microscopy using indirect illumination	• Nondestructive • Relatively simple methods and equipment	• Primarily suitable for measurement of surface damage • Hand-tracing introduces subjectivity and imprecision	• Eliminates subjectivity and imprecision associated with hand-tracing • Optimized for subsurface, rather than surface, measurement

2.2.2 Knee Simulator Testing of the Tibial Inserts

2.2.2.1 Tibial Insert Properties

A tibial insert from a state-of-the-art, commercially available prosthetic knee joint is obtained from the manufacturer (manufacturer identity withheld to maintain testing confidentiality). Figure 2.7 shows the tibial insert after knee simulator testing, which caused visible subsurface fatigue crack damage. The insert is a posterior-stabilized/cruciate sacrificing type (identified by the large tab), size 1, and 7 mm thick. The tibial insert is left sided, i.e., for implantation in the left knee. The insert is machined from compression molded Ticona GUR 1050 UHMWPE, and 25-40 kGy gamma irradiation sterilized in a vacuum followed by nitrogen flush packaging. The nitrogen flush packaging reduces the amount of oxygen available for free-radical production, preventing oxidative damage. The tibial insert was shelf aged for two weeks after sterilization prior to knee simulator testing in accordance with the standard accelerated aging procedure for gamma irradiated UHMWPE [33]. A slice has been removed for oxidation analysis.

2.2.2.2 Knee Simulator Test Protocol

The tibial insert is tested at the University of Nebraska Medical Center Orthopaedic Biomechanics Laboratory, Omaha, NE. using a 4-station modified Instron-Stanmore Model KC knee simulator (Instron Corp., Norwood, MA.) in accordance with International Organization for Standardization (ISO) standard 14243-1 [10]. Knee simulators are costly and specific expertise

Figure 2.7: Top view of tibial insert after knee simulator testing, showing a slice that was removed for oxidation testing and a fatigue crack damage zone.

is needed to obtain reliable and repeatable results. Figure 2.8 shows a left knee femoral component and tibial insert loaded in a single station of the knee simulator. Key components include the container for holding the bovine calf serum used to lubricate the prosthetic knee joint components, the pivot point for varus-valgus rotation, the load cells used to measure the applied forces and torques, the tibial insert enclosure, and the attachments for the femoral component and tibial insert of the prosthetic knee joint. Lubrication between the articulating surfaces of the prosthetic knee joint is provided by bovine calf serum diluted with deionized water to a protein mass concentration of 20 g/l, as prescribed in ISO standard 14243-1 [10]. Diluted calf serum mimics the properties of synovial fluid, which is the natural lubricant in the knee. Specimen mounting and alignment is performed in accordance with ISO 14243-1 [10].

Figure 2.9 shows the direction of the knee simulator axial, anterior-posterior, and internal-external force control and flexion-extension motion control. It also shows the passive spring element movement restraint in the anterior-posterior, and internal-external directions [10]. These force and motion directions follow the standard anatomical reference directions defined in Figure 1.6. The knee simulator does not allow any medial-lateral displacement, while varus-valgus rotation is unconstrained. The machine frame and the bovine serum container, as shown in Figure 2.7, are removed in Figure 2.8 for clarity. Figures 2.8 and 2.9 show the two pivot points through which the knee simulator transmits axial loading to the tibial insert. One pivot point is positioned at the anterior and one at the posterior of the tibial insert, both offset medially from the anterior-posterior midline of the tibial insert by a distance of 7% of the tibial insert width [10]. These pivots allow rotation in the varus-valgus direction, mimicking the slight varus-valgus angle changes that occur during in vivo gait. Recording the varus-valgus angle is not required during the knee simulator testing and was not reported in this case. The anterior-posterior force is applied to the tibial insert with respect to the tibial insert's local anterior-posterior axis. This local anterior- posterior axis is defined as the axis that connects the anterior and posterior pivot points shown in Figure 2.9.

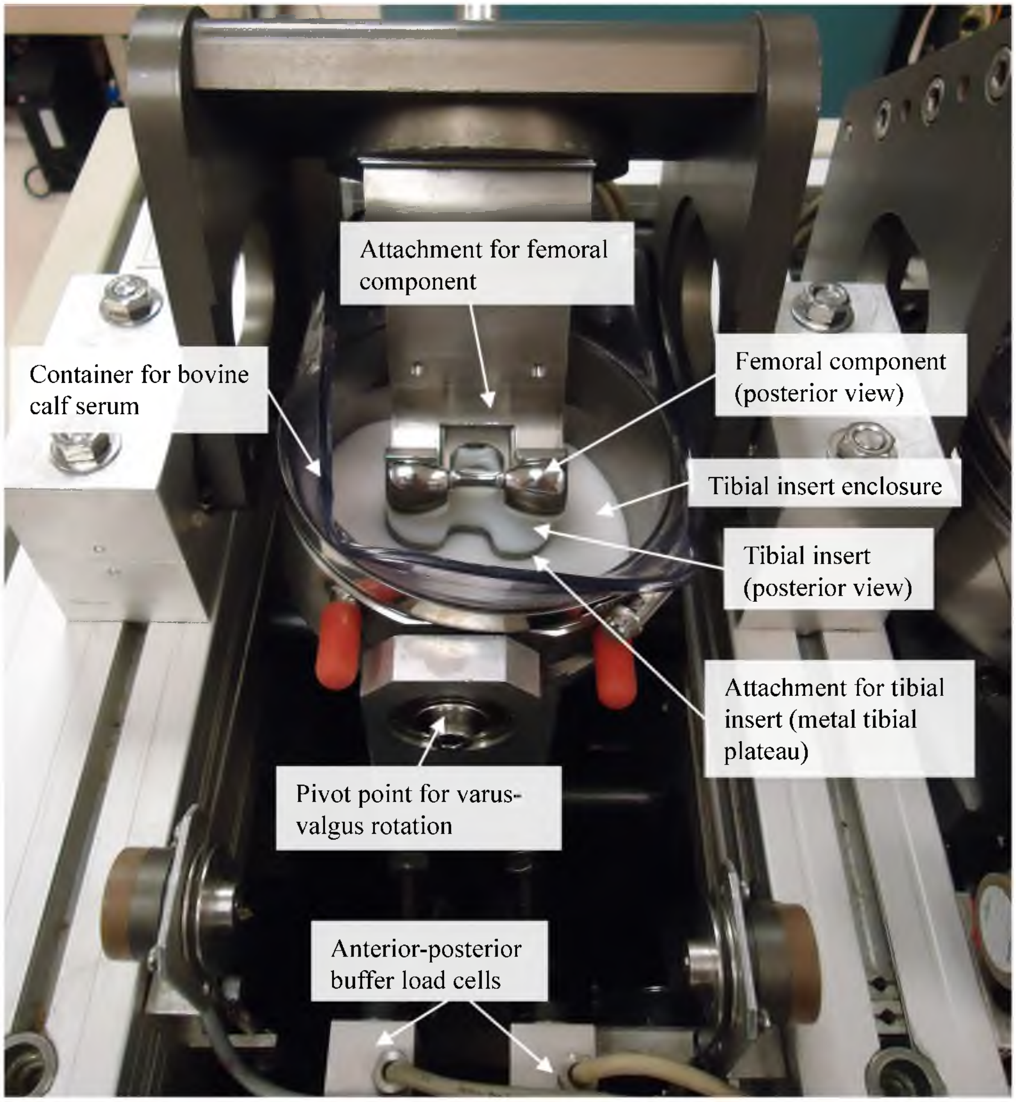

Figure 2.8: Left femoral component and tibial insert loaded for testing in a knee simulator.

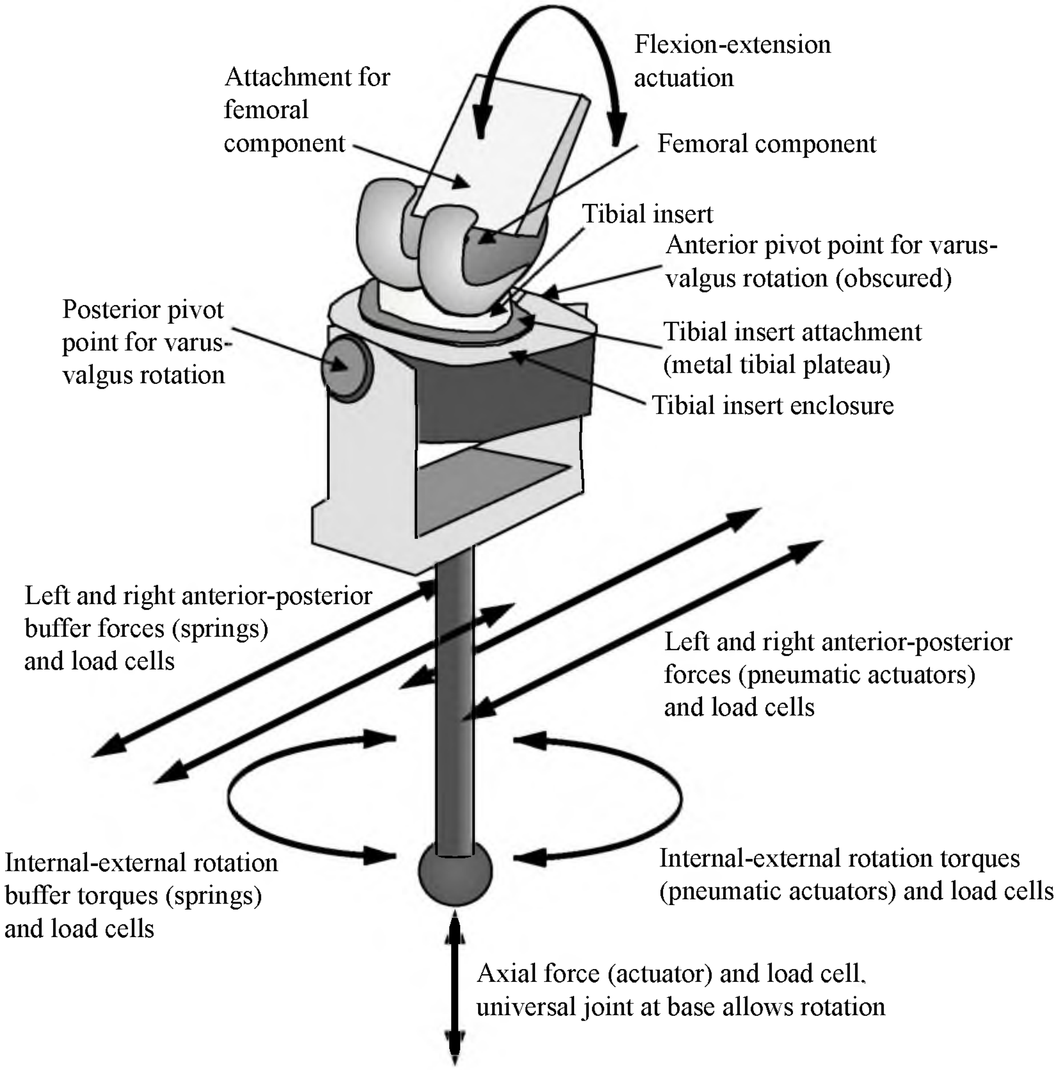

Figure 2.9: Posterior-medial view of the force and motion control as it applies to the (left) prosthetic knee joint.

A passive restraint, or buffer spring force, is applied in the same local anterior-posterior direction. The restraining force within ± 2.5 mm of the neutral position is zero, with an increase to 9.3 ± 0.5 N/mm outside of this range for a cruciate-sacrificing prosthetic knee joint. Figure 2.10 shows the load (axial, anterior-posterior, and internal-external) and motion (flexion-extension) as a function of the fraction of the gait cycle prescribed by ISO standard 14243-1 [10]. The loading includes both the pneumatically driven forces and torques and the forces and torques enforced by the passive movement restraint system. The movement restraint system mimics the

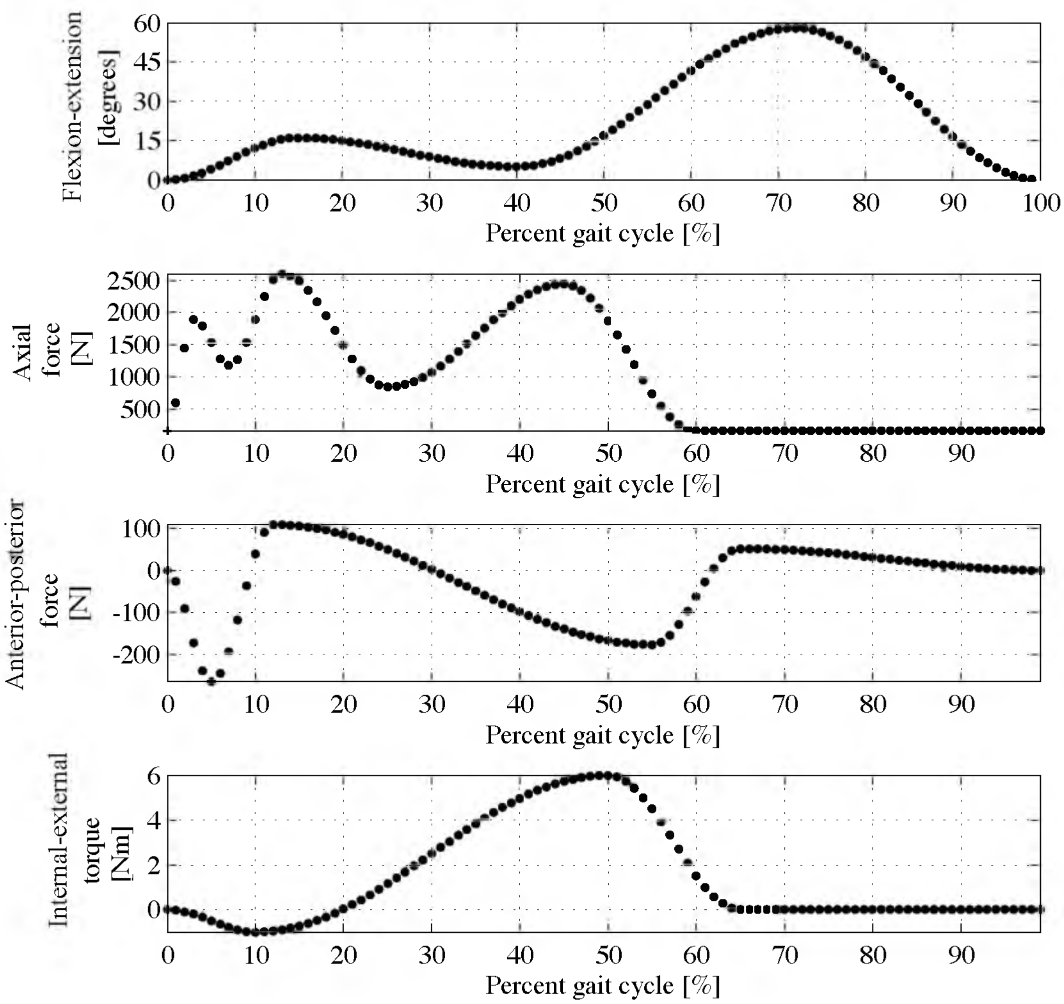

Figure 2.10: Motion and force control curves as prescribed by ISO 14243-1 (Data obtained from [10]).

soft tissues of the knee by using springs to resist the motion created by the pneumatically applied forces, as described in detail by Haider [7] and DesJardins et al. [34]. All pneumatically applied forces and displacements have a tolerance of ± 5% of the respective maximum value [10]. The internal-external torque acts about the tibial insert's axial force axis, which is oriented along the axial force actuator in Figure 2.8, perpendicular to and intersecting the tibial insert's anterior-posterior axis. A buffer torque also acts in the internal-external direction. This passive resistive torque is provided by buffer springs with a spring constant of zero at rotations of less than ± 6 degrees and a spring constant of 0.13 ± 0.01 Nm/degree at $\geq$ 6 degrees for the posterior cruciate ligament (PCL) sacrificing prosthetic knee joint tested in this work. Figure 2.11 shows the pneumatically created force and torque magnitudes specific to this testing as a function of gait cycle percentage and Figure 2.12 shows the test-specific buffer spring force and torque magnitudes for the same gait cycle.

Knee simulator testing is conducted at a frequency of 1 Hertz for 75,177 simulated gait cycles, when tibial insert polyethylene wear is evaluated. The gait cycle data, including prosthetic knee joint pneumatic and buffer spring loading data and kinematics data, are averaged over 19 cycles from the final portion of the knee simulator wear testing to obtain a single representative gait cycle.

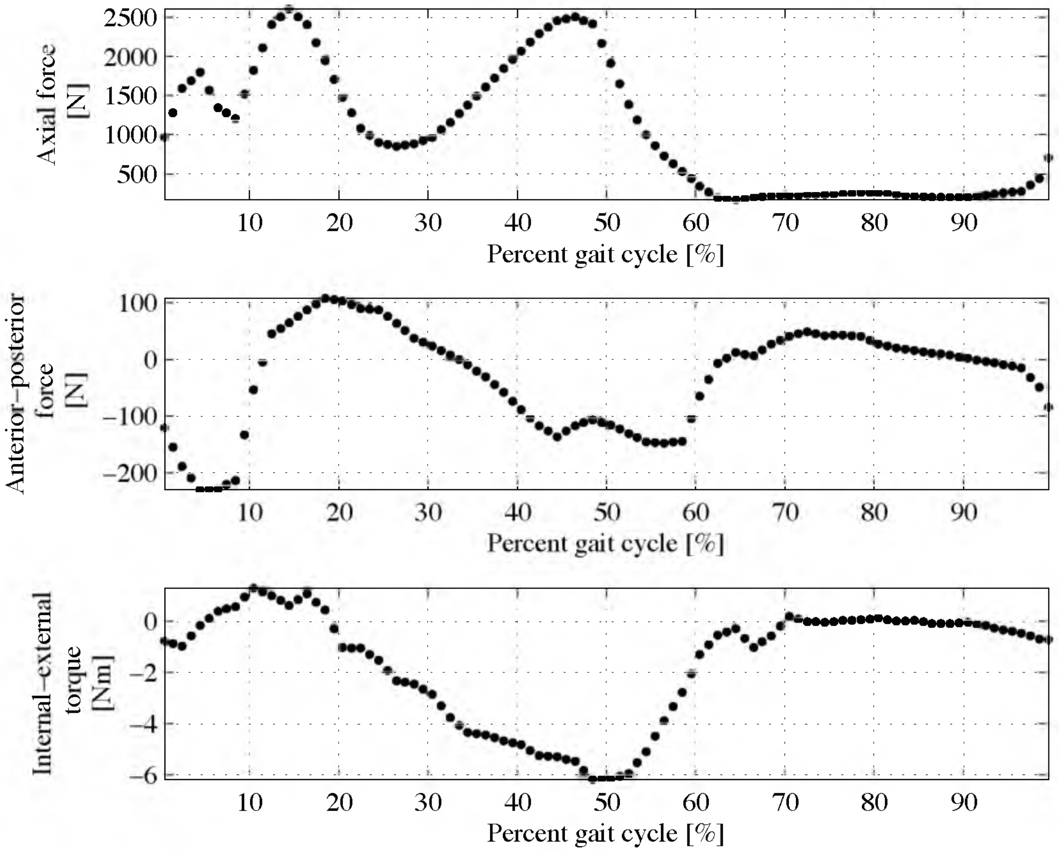

Figure 2.11: Pneumatically applied forces and torques for the knee simulator testing described in this work.

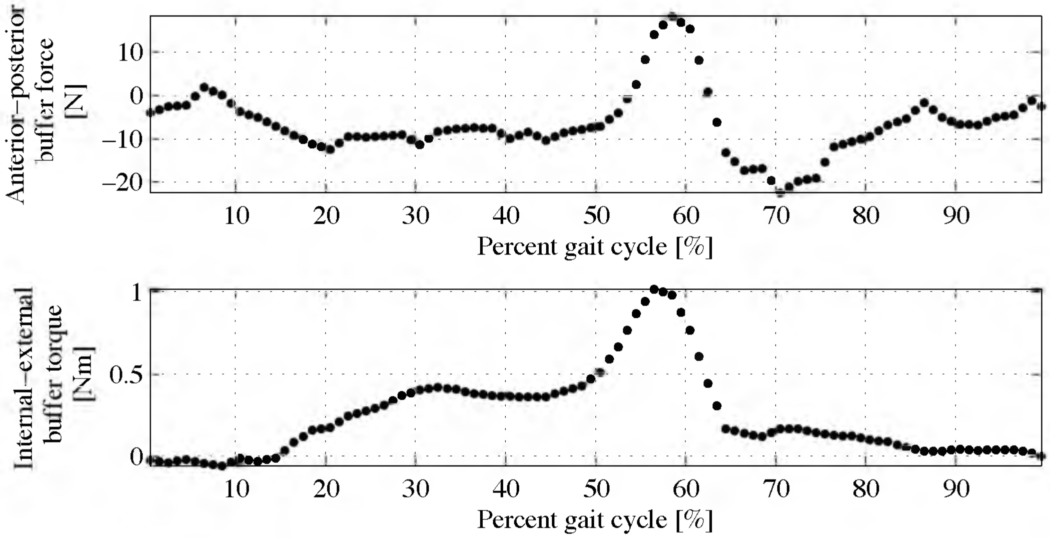

Figure 2.12: Spring buffer force and torque for the knee simulator testing described in this work.

This representative gait cycle is then used as the basis for applied loading and kinematics in the FEM model described in Section 3.2.3. The numerical values of the pneumatically applied flexion angle and knee simulator loading described in this section are given in Appendix A. The numerical values of the buffer forces in the internal-external and anterior-posterior directions are given in Appendix B. Knee simulator testing was aborted prior to the standard test duration of 5 million cycles due to tibial insert fatigue crack damage.

2.2.3 Subsurface Fatigue Crack Damage Detection and Measurement

Two fatigue crack damage evaluation and measurement specimens are used: (1) the wear tested tibial insert (tibial insert 1) described above, and (2) a retrieval tibial insert recovered surgically after in vivo use by a patient (tibial insert 2). Figure 2.13 shows tibial insert 2, the left-knee retrieval insert, with visible subsurface fatigue crack damage.

Tibial insert 2 is cruciate retaining (no large tab), size 4, and 14 mm thick. It has been manufactured and gamma irradiation sterilized following the same procedure used for tibial insert 1. A slice has been removed for oxidation analysis. After knee simulator testing of tibial insert 1

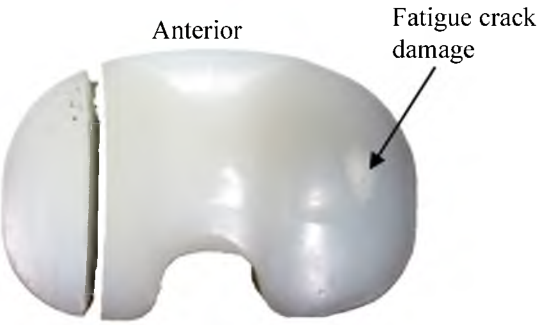

Figure 2.13: Top view of tibial insert 2 exhibiting visible subsurface fatigue crack damage.

and retrieval of tibial insert 2 the tibial inserts are prepared for fatigue crack damage evaluation and measurement. The inserts are cleaned with a soft cloth to remove any surface debris and are stored at -18° C to retard further oxidation. The fatigue crack damage area is quantified by measuring the regions of decreased light transmission, which are associated with fatigue crack damage to the UHMWPE, in photographic images of the transilluminated specimen. Figure 2.14 shows light transmission through transilluminated fatigue crack damaged (Figure 2.14 A) and pristine (Figure 2.14 B) left knee tibial inserts. The fatigue crack damage appears as a darkened crescent on the medial condyle of the fatigue crack damaged tibial insert.

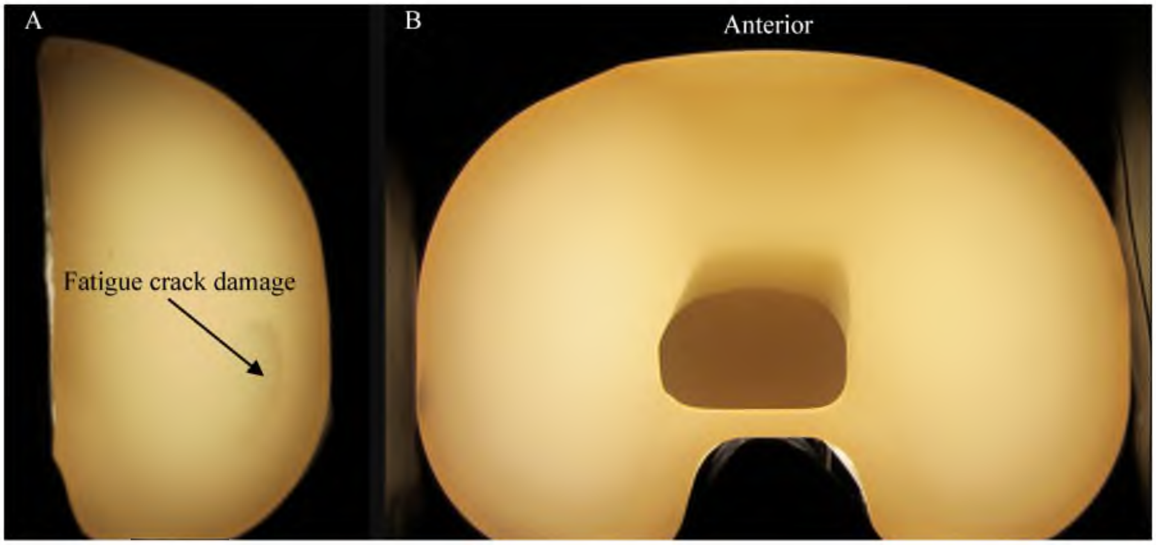

Figure 2.14: Light transmission through transilluminated left knee tibial inserts (A) with fatigue crack damage and (B) without fatigue crack damage.

Figure 2.15 shows a schematic of the physical set-up for image capture and a schematic of the Matlab image processing steps for our novel subsurface fatigue crack damage measurement technique. Figure 2.15 A illustrates the image capture set-up. The tibial insert is backlit using a uniform light source created by a fiber optic illuminator (Fiber-Lite, Bausch & Lomb, USA) and diffusing screen (0.007 mm matte two-sided film, Inventables, USA). The tibial insert is secured in a vise and is surrounded with opaque plastic sheeting to prevent light from passing around the

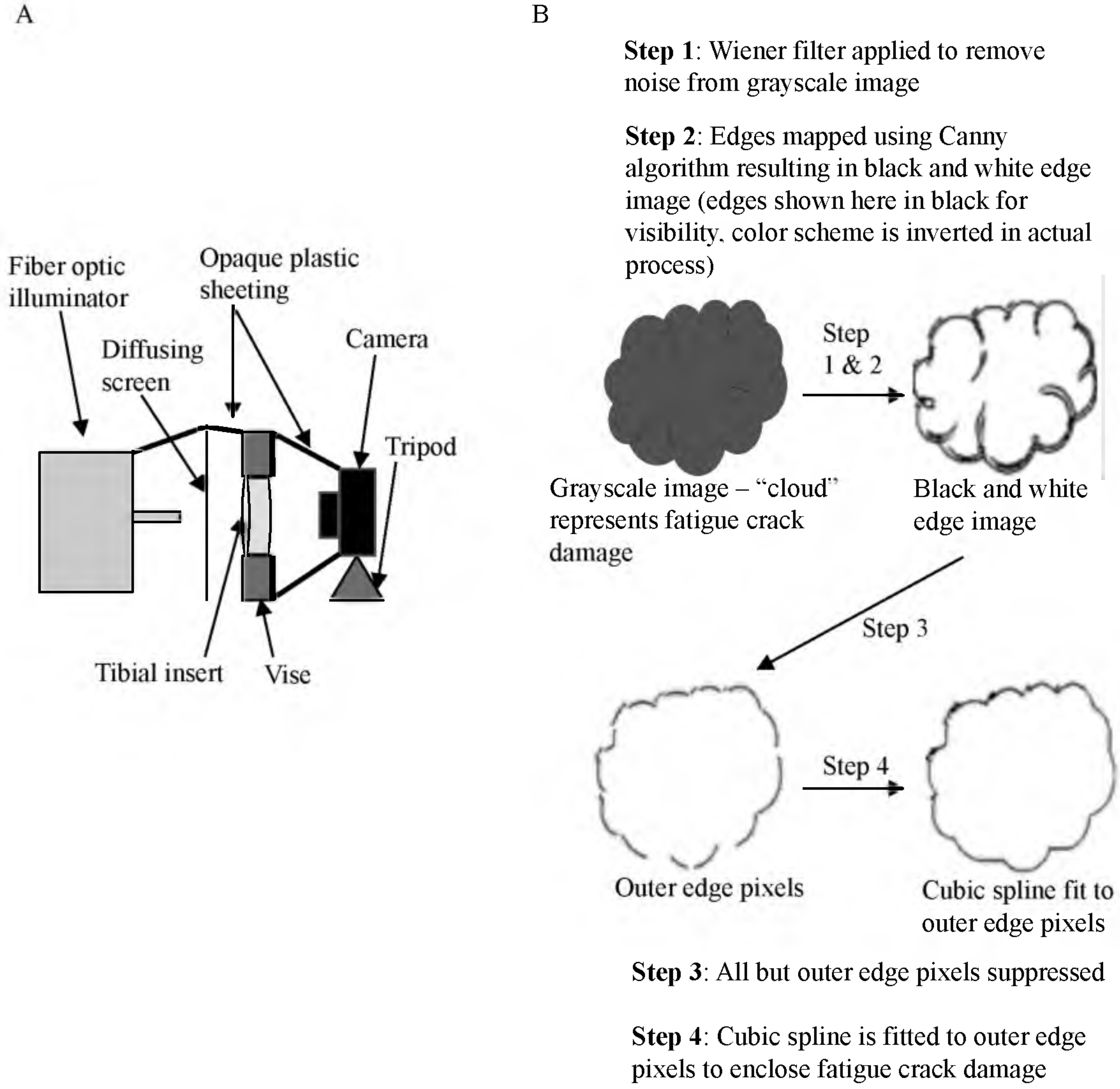

Step 1: Wiener filter applied to remove noise from grayscale image

Step 2: Edges mapped using Canny algorithm resulting in black and white edge image (edges shown here in black for visibility, color scheme is inverted in actual process)

Step 3: All but outer edge pixels suppressed

Step 4: Cubic spline is fitted to outer edge pixels to enclose fatigue crack damage

Figure 2.15: Image capture set-up and processing procedure. (A) Physical set-up for image capture and (B) schematic of the image processing in Matlab for fatigue crack damage area measurement.

sides of the tibial insert. Sheeting is also used to block ambient light from the entire setup between the fiber optic illuminator and the digital camera (Powershot ELPH 300 HS, Canon, USA). A scale bar with printed lines at 1 mm intervals is attached to the tibial insert flush with the photographed surface. In order to prevent dimensional distortion created by an oblique viewing angle the images are captured with the camera lens centered on and parallel to the backside surface of the tibial insert. The distance between the camera lens and tibial insert is adjusted to ensure that the fatigue crack damage is in focus.

Figure 2.15 B depicts the image-processing algorithm. The general processing steps are: 1) remove noise from the image, 2) map the edges, including the edges created by fatigue crack damage, and distinguish between fatigue crack damage edges and edges caused by noise, 3) remove the inner edge pixels, leaving the fatigue crack damage region defined by the outermost fatigue crack damage edge pixels, and 4) fit a cubic spline to the remaining pixels to measure the fatigue crack damage region.

Figure 2.16 shows a step-by-step overview of the algorithm applied to a captured image. Transilluminated images are imported into Matlab, converted to grayscale, and filtered using the built-in Wiener filter (Figure 2.16 A). Next, edge detection is performed using the built-in Canny edge function, resulting in a black and white image of edge and non-edge pixels (Figure 2.16 B). The edge pixels are sorted into edge pixels caused by fatigue crack damage and nondamage edge pixels caused by image noise. The nondamage edge pixels are removed, leaving only the fatigue crack damage edge pixels (Figure 2.16 C). The inner edge pixels are then removed, leaving only the outermost edge pixels (Figure 2.16 D), which correspond to the outer edge of the fatigue crack damage. Figure 2.16 E shows the outer edge pixels superimposed on the original fatigue crack damage image for comparison. The outermost fatigue crack damage edge pixels are used as interpolation points for a piecewise cubic spline. Figure 2.16 F shows the cubic spline fit to the outer fatigue crack damage edge pixels. Once the cubic spline is created the area within the cubic spline, which approximates the area of the fatigue crack damage, can be calculated. Figure 2.16 G

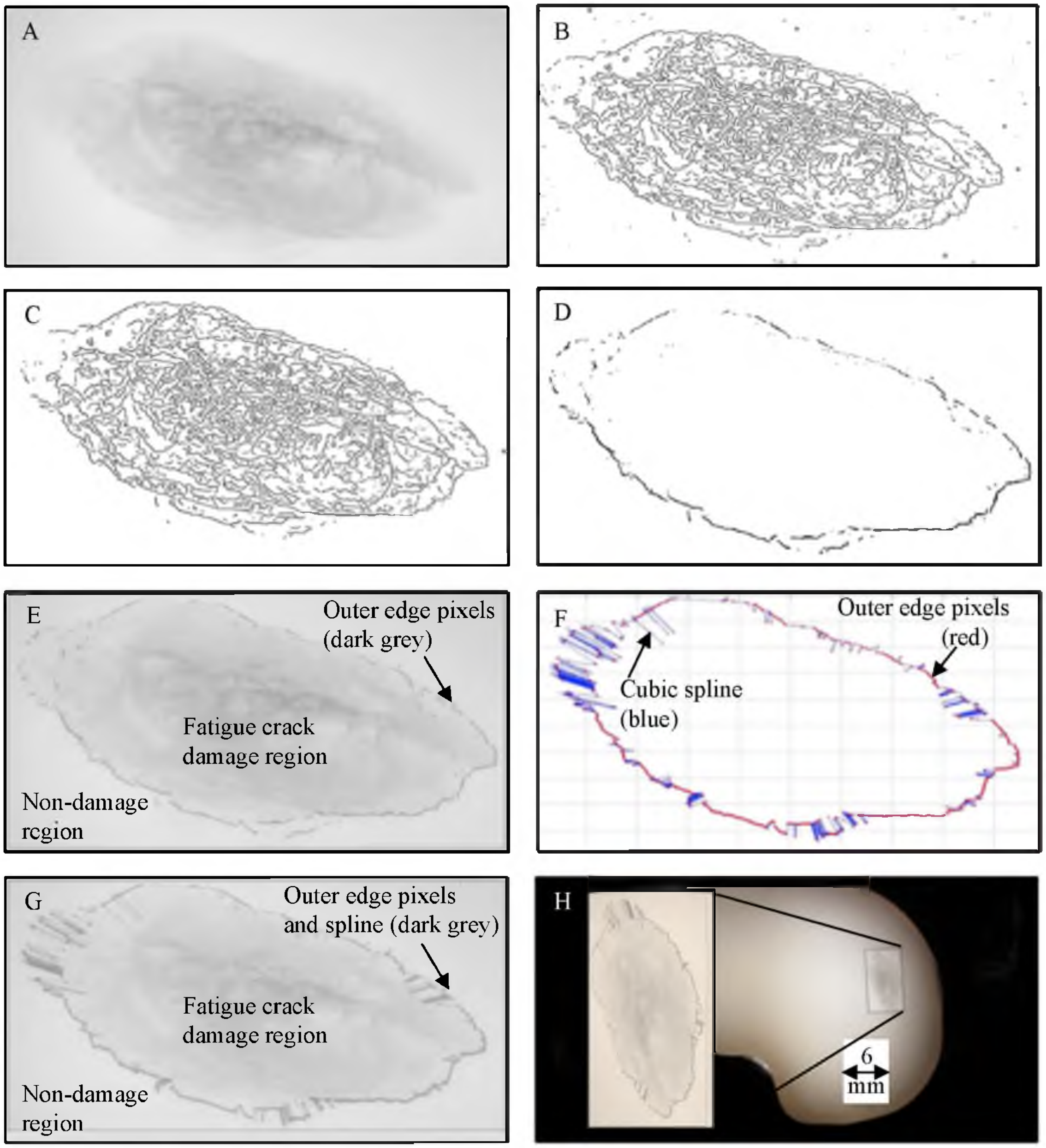

Figure 2.16: Image processing and fatigue crack damage area measurement process. (A) The original image is converted to grayscale and filtered with a Wiener filter. (B) A Canny edge finding algorithm is used to find edges within the image. (C) The edge pixels identified by the Canny algorithm are sorted into true fatigue crack damage edges and nondamage edges. Nondamage edges are eliminated. (D) All but the outermost edge pixels are removed. (E) The outer edge image superimposed on the original fatigue crack damage image for comparison. (F) A cubic spline is fit to the outer fatigue crack damage pixels. (G) The cubic spline superimposed on the fatigue crack damage image. (H) View of the entire tibial insert with cubic spline superimposed, to scale and with the fatigue crack damage magnified (inset).

shows the cubic spline superimposed on the original fatigue crack damage image. Figure 2.16 H shows the same cubic spline superimposed on an image of the entire tibial insert medial condyle to show the relative size and position of the cubic spline relative to the tibial insert condyle. A magnified inset shows a detailed view of the fatigue crack damage and superimposed cubic spline.

The Wiener filter is applied to remove high frequency noise, which degrades the effectiveness of the edge detection algorithm, from the original captured images. Figure 2.16 A shows the grayscale image after the Wiener filter is applied. The Wiener filter is used because it is an adaptive low-pass filter designed to reduce high-frequency noise in grayscale images while retaining the quality of edges within the image [35]. Low-pass filters have the potential for reducing the quality of edges within the image due to the fact that an image edge represents a high-frequency change in the pixel value between adjacent pixels [36]. By adjusting the frequency threshold based on the frequency of pixel value variation in the local neighborhood of each pixel the Wiener filter algorithm adjusts the filter threshold and thus the amount of smoothing applied in the corresponding region [37]. By applying less smoothing in regions with high pixel value variance, such as the fatigue crack damage and outer edge regions of the tibial insert, and more smoothing in regions of low pixel value variance, such as the pristine portion of the tibial insert, the edges within the image are preserved and well-defined [37].

The Canny edge finding algorithm detects edges in the filtered grayscale images in two steps. First, pixels that represent local maxima are found [38–40] and pixels not at local maxima are suppressed (set to a value of zero) [38,40]. Second, the algorithm examines the unsuppressed pixels and compares the local gradient at each remaining pixel to a set of two gradient thresholds [39,40]. If pixel gradients do not reach or exceed the low threshold they are suppressed, while pixels with gradients that exceed the high threshold are identified as edges. Pixels with gradients between the two thresholds are suppressed unless they are adjacent to pixels with thresholds that exceed the high threshold [39,40]. The Canny algorithm edge detection function returns the pixel matrix in which edge pixels are white (value of 1) and non-edge pixels are black (value of 0) [38]. The Canny edge detection method is selected here because of its robustness, which makes it commonly used in image processing edge detection applications [39–41].

The low and high Canny algorithm threshold for each tibial insert fatigue crack damage image is selected by the user for high sensitivity to edges in the fatigue crack damage region. Under-detection of edges is undesirable due to the potential for under-estimating the fatigue crack damage area. Over-detection of edges, in which noise is incorrectly classified as edges, is corrected through the edge pixel sorting process described in the following section. The selected low and high thresholds for the fatigue crack damage image for tibial insert 1 are 0.0225 and 0.2500, respectively, while the low and high thresholds for the fatigue crack damage image for tibial insert 2 are 0.0300 and 0.0740, respectively. Figure 2.16 B shows the edge pixels detected by the Canny function in the tibial insert fatigue crack damage image.

The edge pixels identified by the Canny algorithm are sorted into true fatigue crack damage edges and nondamage edges. A nondamage edge delineates an image region that is free of fatigue crack damage but is corrupted by noise and light saturation. Nondamage edges falsely appear to indicate fatigue crack damage. To decide whether a particular edge pixel is the result of fatigue crack damage or a nondamage edge pixel resulting from image noise the neighborhood of pixels surrounding the pixel in question is characterized by means of the edge pixel density. The edge pixel density is defined as the number of edge pixels (white pixels as output by the Canny function) divided by the total number of pixels (black and white pixels) within a neighborhood surrounding the pixel that is being characterized.

The fatigue crack damage regions of the tibial insert image have a higher mean edge pixel density than nondamage regions of the image. This difference in edge pixel density in the damaged and undamaged regions is used to categorize each edge pixel as fatigue crack damage or nondamage. Two sorting parameters must be determined: 1) the optimal neighborhood size for capturing the edge pixel density surrounding the pixel of interest and 2) the edge pixel density threshold that separates fatigue crack damage edge pixels from nondamage edge pixels.

The optimal neighborhood size is determined as follows. First, an identical selection rectangle is used to manually select a fatigue crack damage and nondamage selection. The fatigue crack damage selection is chosen from the region that exhibits visible fatigue crack damage, while the nondamage selection is chosen from the visually intact region. Figure 2.17 shows a typical example of the rectangular selection that is manually selected within the fatigue crack damage (Figure 2.17 A) and nondamage region (Figure 2.17 B). Second, the neighborhood size

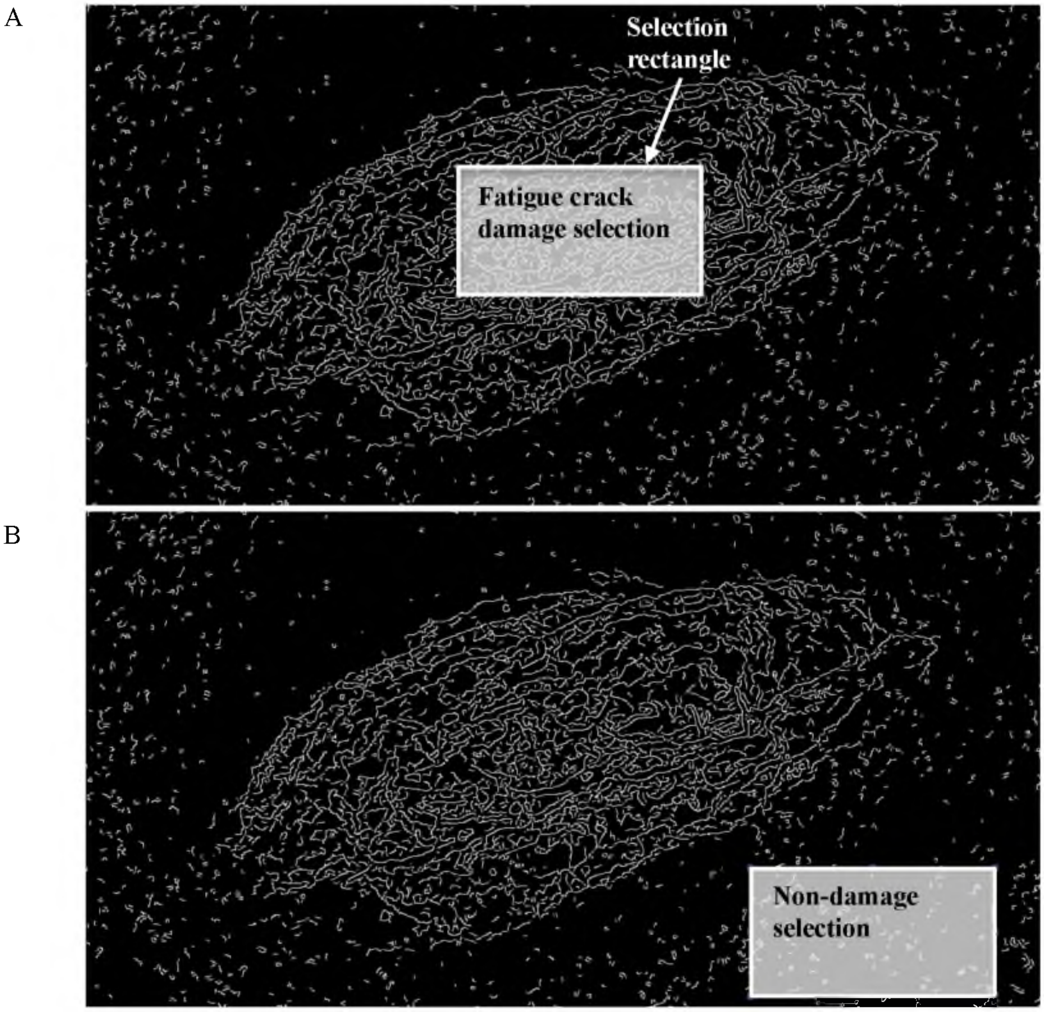

Figure 2.17: Fatigue crack damage and nondamage selections in Matlab. (A) Selection within the fatigue crack damage region and (B) nondamage region using an identical selection rectangle.

that provides the best representation of the fatigue crack damage versus nondamage edge pixel density for the fatigue crack damage and nondamage selections is determined. To determine the neighborhood size that results in the most accurate sorting of fatigue crack damage versus nondamage edge pixels a series of neighborhood sizes are tested on the fatigue crack damage and nondamage selections. Neighborhood sizes (in pixels) range from 25 pixels (5 by 5 pixels) up to a quarter of the width in pixels of the rectangular selection (a quarter of the rectangle width by a quarter of the rectangle width). This maximum neighborhood size will vary depending on the size of the specific fatigue crack damage image and the size of the rectangular fatigue crack damage cluster selection in pixels. The intracluster correlation coefficient is used to determine which neighborhood size provides the best differentiation between fatigue crack damage and nondamage edge pixels.

The intracluster correlation coefficient quantifies the ability to distinguish between fatigue crack damage edge pixels and nondamage edge pixels. A cluster is defined as a set of data that come from a single group with a defining characteristic. In this case the data are the edge pixel densities from each neighborhood and the two clusters correspond to the two rectangular selections (Figure 2.17). The defining characteristic separating the two clusters is whether the rectangular selection is chosen from the fatigue crack damage or nondamage image regions.

The intracluster correlation coefficient $0 \leq \rho \leq 1$ is defined as

$$\rho = \frac{\left(S_b^2\right)}{S_b^2 + S_w^2} \tag{2.1}$$

where S_w^2 is the within-cluster edge pixel density variance and S_b^2 is the between-cluster edge pixel variance, referring to the terminology used by Killip et al. [42]. Within-cluster edge pixel variance S_w^2 is the variance in neighborhood edge pixel densities occurring within a single cluster,

$$S_w^2 = \frac{\sum_{i=1}^{n}\left(x(i) - \overline{x}\right)^2}{n-1} \tag{2.2}$$

Within-cluster variance S_w^2 is calculated for both the fatigue crack damage and nondamage clusters for each neighborhood size. n is the total number of neighborhood samples within the cluster, $x(i)$ represents the average edge pixel density for each neighborhood sample, and $\bar{x}$ represents the overall average edge pixel density for the cluster.

The between-cluster variance S_b^2 is the variance between the clusters being compared, which in this case are the manually selected nondamage and fatigue crack damage rectangles. The between-cluster variance is calculated as

$$S_b^2 = \frac{n_D\left(x_D - \bar{x}\right)^2 + n_{ND}\left(x_{ND} - \bar{x}\right)^2}{\left(n_D + n_{ND}\right) - 1} \tag{2.3}$$

S_b^2 is calculated for each neighborhood size, where n_{ND} and n_D represent the number of neighborhoods in the nondamage and fatigue crack damage selections, $\bar{x}$ represents the overall average edge pixel density of the image from which the cluster selections are chosen, and x_{ND} and x_D are the average edge pixel densities of the nondamage and fatigue crack damage clusters.

The intracluster correlation coefficient represents the similarity between edge pixel densities of neighborhood samples within a cluster [42], with a value of 1.0 indicating identical edge pixel densities for all neighborhood samples from a single cluster. In this work the fatigue crack damage intracluster correlation coefficient is selected as the parameter for determining the optimal neighborhood size. This fatigue crack damage intracluster correlation coefficient was selected instead of the nondamage intracluster correlation coefficient because the values of the fatigue crack damage intracluster correlation coefficient were consistently lower (further from 1.0) than those of the nondamage intracluster correlation coefficient, making it the stricter criterion.

An intracluster coefficient value approaching 1.0 indicates that the between-cluster variance is much larger than the within-cluster variance. Physically, this means that the variance between the edge pixel densities of the neighborhoods from the two clusters, fatigue crack damage and nondamage, is greater than the variance of the edge pixel densities between all the neighborhoods within the fatigue crack damage cluster. The within-cluster variance provides information about the similarity in edge pixel density within the cluster of interest (fatigue crack damage), while the between-cluster variance provides information specifically about how distinguishable the fatigue crack damage and nondamage clusters are from each other based on edge pixel density.

The between-cluster variance, within-cluster variance, and intracluster coefficient change depending on the neighborhood size used to calculate the edge pixel density around each pixel. Table 2.2 lists the between-cluster variance, within cluster variance, and intracluster coefficient of the twelve neighborhood sizes tested for the fatigue crack damage and nondamage selections. Table 2.2 illustrates that the between-cluster variance increases with increasing neighborhood size, reaching its maximum value of $2.231 \cdot 10^{-3}$ at the second largest neighborhood size, 105 by 105 pixels. In contrast, the within-cluster variance decreases with increasing neighborhood size, reaching a minimum value of $8.376 \cdot 10^{-4}$ at the same second largest neighborhood size. The combination of an increasing between-cluster variance and decreasing within-cluster variance results in an increase in intracluster correlation coefficient with increasing neighborhood size, with a maximum value of 0.727 at the second highest tested neighborhood size. Note that the variance here is dimensionless, since it is expressed as edge pixels over total pixels.

The optimal neighborhood size is selected based on the size at which the highest fatigue crack damage cluster intracluster correlation coefficient is first achieved. Figure 2.18 shows a plot of the intracluster correlation coefficient of the fatigue crack damage and nondamage clusters versus the tested neighborhood sizes. The plot demonstrates the effect of a too small neighborhood size. The smallest neighborhood size, 5 by 5 pixels, is associated with a very small fatigue crack damage cluster intracluster correlation coefficient of less than 0.2. Fatigue crack damage cluster intracluster correlation coefficient values in excess of 0.7 are only reached at the

Table 2.2: Between-cluster variance S_b^2, within-cluster variance S_w^2, and intracluster correlation coefficient ρ of each tested neighborhood size.

Neighborhood size in one dimension [Pixels]	S_b^2	S_w^2	ρ
5	$2.107 \cdot 10^{-3}$	$1.176 \cdot 10^{-2}$	0.152
15	$2.109 \cdot 10^{-3}$	$3.062 \cdot 10^{-3}$	0.408
25	$2.113 \cdot 10^{-3}$	$2.167 \cdot 10^{-3}$	0.494
35	$2.119 \cdot 10^{-3}$	$1.749 \cdot 10^{-3}$	0.548
45	$2.126 \cdot 10^{-3}$	$1.583 \cdot 10^{-3}$	0.573
55	$2.143 \cdot 10^{-3}$	$1.180 \cdot 10^{-3}$	0.645
65	$2.150 \cdot 10^{-3}$	$1.118 \cdot 10^{-3}$	0.658
75	$2.161 \cdot 10^{-3}$	$1.016 \cdot 10^{-3}$	0.680
85	$2.185 \cdot 10^{-3}$	$9.898 \cdot 10^{-4}$	0.688
95	$2.198 \cdot 10^{-3}$	$8.340 \cdot 10^{-4}$	0.725
105	$2.231 \cdot 10^{-3}$	$8.376 \cdot 10^{-4}$	0.727
115	$2.231 \cdot 10^{-3}$	$8.376 \cdot 10^{-4}$	0.727

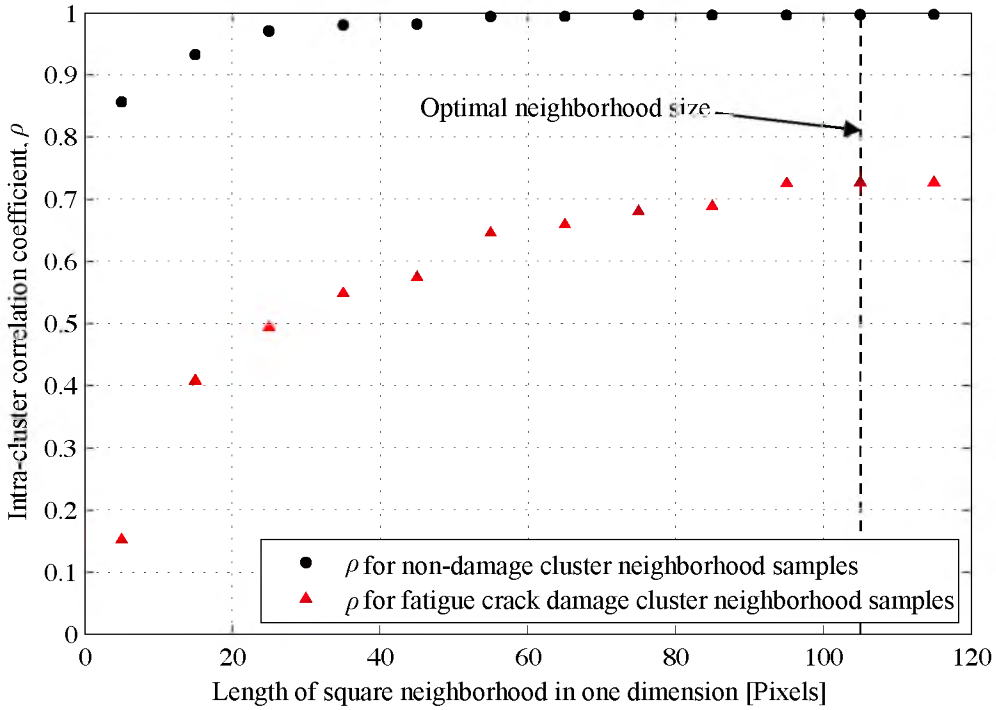

Figure 2.18: Intracluster correlation coefficient ρ of fatigue crack damage and nondamage clusters for the range of tested neighborhood sizes.

three largest tested neighborhood sizes. The optimal neighborhood size, where the fatigue crack damage cluster intracluster correlation coefficient first reaches its maximum value of 0.727 and then plateaus, is 105 by 105 pixels for the tested fatigue crack damage image. Figure 2.19 shows the edge pixel density range for the fatigue crack damage and nondamage clusters versus the tested neighborhood sizes.

The circular and triangular markers indicate the mean edge pixel densities of the fatigue crack damage and nondamage clusters, respectively. The error bars indicate the spread of the edge pixel densities. For the smallest neighborhood size, the edge pixel densities calculated for the fatigue crack damage and nondamage clusters overlap significantly, displaying low between-cluster variance, and vary widely for each cluster, showing high within-cluster variance. In combination, this results in a low intracluster correlation coefficient (0.152) and limited ability to distinguish between the two clusters at the 5 by 5 pixel neighborhood size. In contrast, the

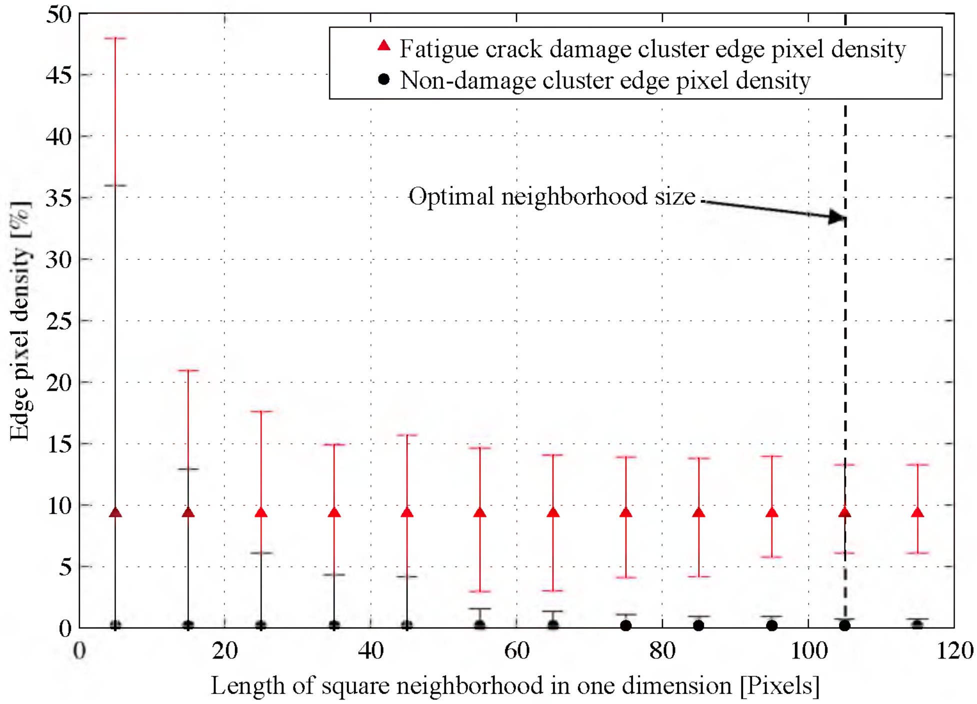

Figure 2.19: Mean edge pixel density of fatigue crack damage and nondamage clusters for each tested neighborhood sample size. The circular and triangular markers indicate the mean edge pixel densities of the fatigue crack damage and nondamage clusters, respectively. The error bars indicate the spread of the edge pixel density.

optimal neighborhood size, 105 by 105 pixels, corresponds to no overlap between the density ranges, indicating increased between-cluster variance, and a small density range for each cluster, indicating increased within-cluster variance and a high intracluster correlation coefficient (0.727). Once the optimal neighborhood size is determined, the edge pixels in the tibial insert image can be sorted into fatigue crack damage and nondamage based on each edge pixel's neighborhood edge pixel density. The tibial insert image, which has been processed into a matrix of edge and non-edge pixels by the Canny edge detection function, is searched for edge pixels in each row and column. When an edge pixel is found, the edge pixel density is calculated for the pixels that make up the neighborhood surrounding the edge pixel. Edge pixels for which the surrounding density of edge pixels falls below the edge pixel density threshold, i.e., the maximum edge pixel density in the manually selected nondamage sample region, are labeled as nondamage edge pixels and eliminated. The result of this elimination is observable as a difference in image noise between Figure 2.16 B and Figure 2.16 C.

All but the outermost fatigue crack damage pixels are eliminated. This is accomplished by searching the edge pixel image from top to bottom along the columns and recording the first edge pixel encountered in each column, then repeating the process in the opposite direction, searching bottom to top along the columns to find the top and bottom edges of the fatigue crack damage region. The same process is repeated left to right and right to left along the rows of the image to find the left and right edges of the fatigue crack damage. The outer edge pixel indices are recorded. The edge pixels at these indices are preserved and all other edge pixels are removed. Figure 2.16 D illustrates the outline of edge pixels detected and mapped to a new image through this process.

The piecewise cubic spline is then fit to the outer edge pixels. The rectangular coordinate indices of the outer edge pixels are converted to polar coordinates and sorted by angle. The centroid of the outer edge pixels is used as the origin. Once sorted, the outer edge pixels act as interpolation coordinates for a piecewise cubic spline that circumscribes the outside of the fatigue crack damage. Figure 2.16 F shows the cubic spline that is fit to these outline pixels. The area within this cubic spline is calculated to represent the area of the fatigue crack damage region. The fatigue crack damage area in pixels is then converted to mm^2 based on a scale image. The fatigue crack damage in each tibial insert is measured in the transverse plane of the tibial insert, parallel to the tibial insert's flat base.

2.3 Results

2.3.1 Knee Simulator Fatigue Testing

The fatigue crack damage developed during wear testing is located in the subsurface region of tibial insert 1. The occurrence of fatigue crack damage suggests that, during knee simulator testing, the tibial insert specimen is subject to loading resulting in local stress exceeding the yield stress of the UHMWPE. The gravimetric wear results are rendered void due to the early termination of the wear test and are not reported here.

2.3.2 Fatigue Crack Damage Detection and Measurement

2.3.2.1 Results For Tibial Insert 1

Figure 2.20 shows the piecewise cubic spline that interpolates through the outer edge pixels of the fatigue crack damage area on tibial insert 1. The total measured fatigue crack damage area is 22 mm^2. The orientation of x- and y-axes of the plotted cubic spline correspond to the anterior-posterior and medial-lateral axes of the tibial insert. Figure 2.21 shows the cubic spline superimposed on the fatigue crack damage area detected on tibial insert 1. An enclosing rectangle in Figure 2.21 A for position and size reference relative to tibial insert 1 highlights the fatigue crack damage. The cubic spline and the visible fatigue crack damage are magnified in Figure 2.21 B for qualitative comparison. Figure 2.21 C shows that the cubic spline fits closely with the visible edge on the left edge of the fatigue crack damage. On the right side, where no distinct edge exists, the edge of the fatigue crack damage region is approximate by a straight section of cubic spline connecting the two points at the far ends of the visible edge line. Jagged cubic spline regions exist, as indicated in Figure 2.21 C, where image noise remains after the image filtering described in Section 2.2.2 and the fatigue crack damage detection algorithm fails to differentiate this noise from fatigue crack damage edge pixels. This effect is most prominent in regions where the visible edge of the fatigue crack damage appears faint or discontinuous and the Canny edge detection function is less effective. Incomplete fatigue cracks with sections of intact material may contribute to faint and discontinuous fatigue crack damage edges.

2.3.2.2 Results For Tibial Insert 2

Figure 2.22 shows the cubic spline that interpolates through the outer edge pixels of the fatigue crack damage area detected on tibial insert 2. The effect of a small amount of image noise

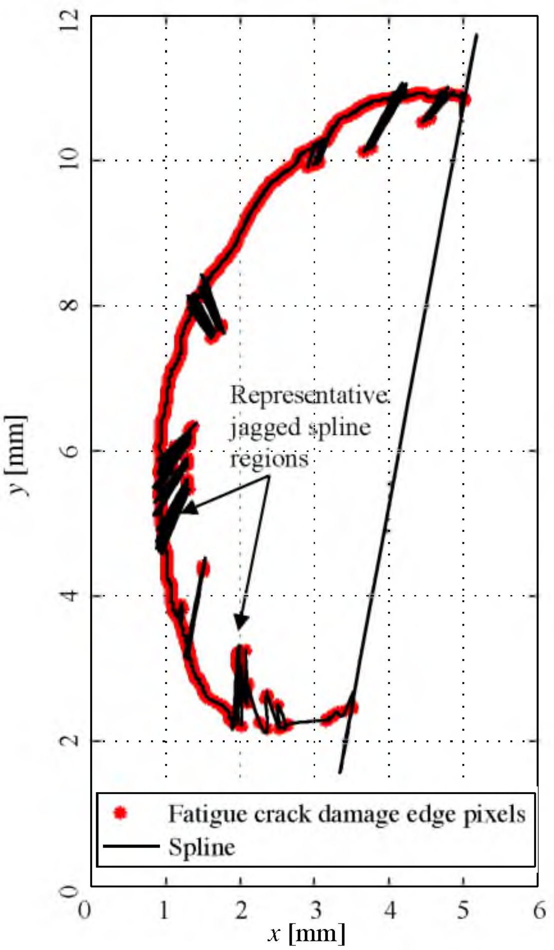

Figure 2.20: The cubic spline fitted to outer fatigue crack damage edge pixels on tibial insert 1.

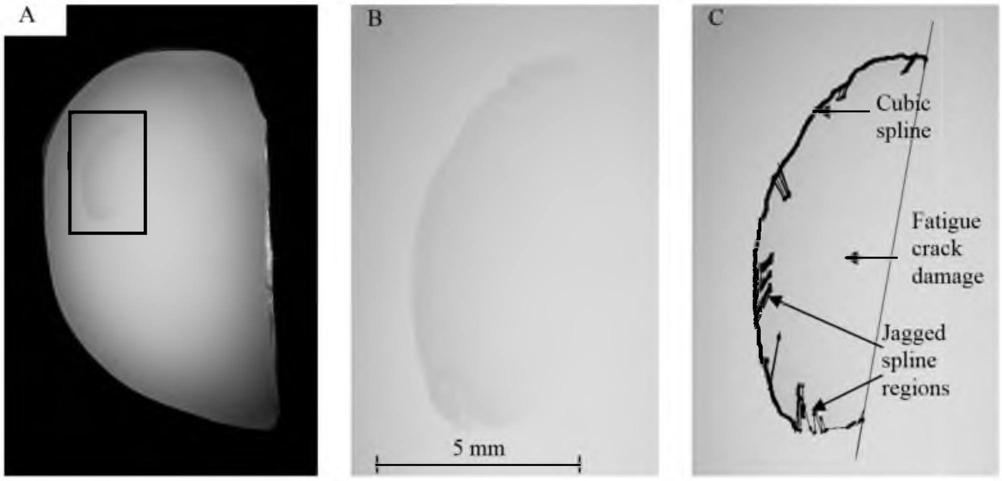

Figure 2.21: The cubic spline superimposed on the fatigue crack damage image for tibial insert 1. (A) The fatigue crack damage area (enclosed in black rectangle) relative to tibial insert 1. (B) Magnified view of fatigue crack damage region. (C) The cubic spline superimposed on the fatigue crack damage image.

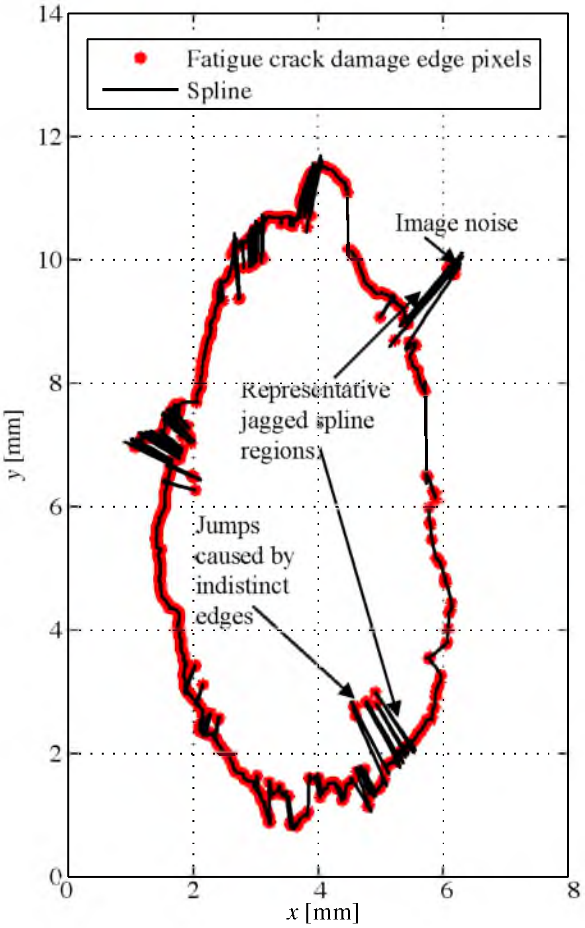

Figure 2.22: The cubic spline fit to the outer edge pixels of the fatigue crack damage on tibial insert 2.

being categorized as fatigue crack damage can be observed as jagged spline regions. Representative occurrences are marked in the plot. The total measured fatigue crack damage area in this plane is 38 mm^2.

Figure 2.23 shows the cubic spline superimposed on the fatigue crack damage area detected on tibial insert 2. The fatigue crack damage is highlighted by an enclosing rectangle in Figure 2.23 A for position and size reference relative to tibial insert 2. The cubic spline and the visible fatigue crack damage are magnified in Figure 2.23 B for qualitative comparison. Figure 2.23 C shows that the cubic spline fits closely with the visible edge of the fatigue crack damage. As observed for tibial insert 1, the cubic spline for tibial insert 2 also contains jagged regions, as indicated in Figure 2.23 C, where image noise is incorrectly classified as part of the fatigue crack damage region.

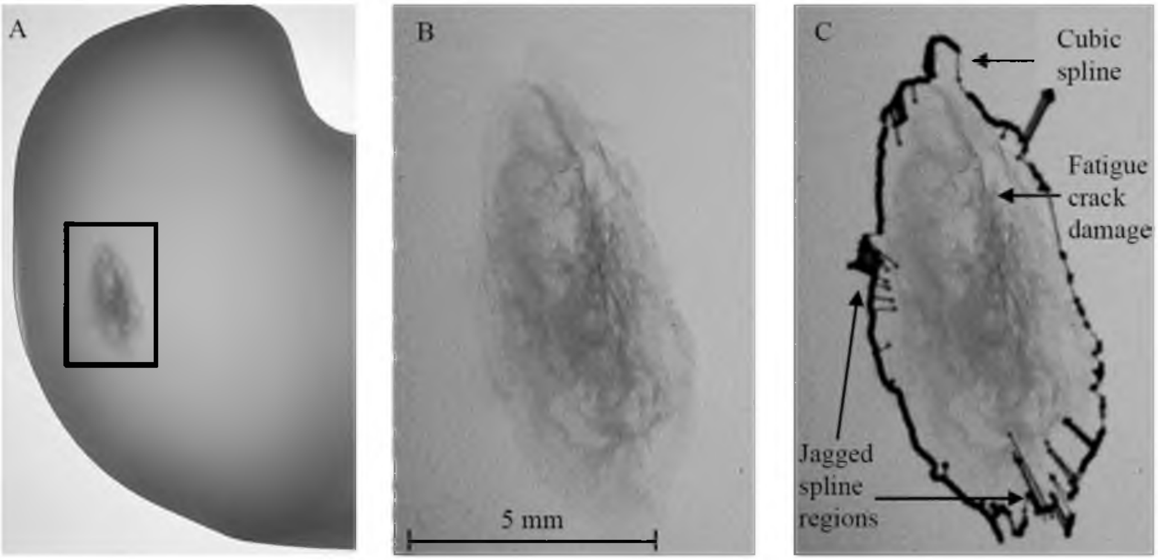

Figure 2.23: Cubic spline superimposed on the fatigue crack damage image for tibial insert 2. (A) The fatigue crack damage area (enclosed in black rectangle) relative to the tibial insert. (B) A magnified view of the fatigue crack damage region. (C) The cubic spline superimposed on the fatigue crack damage image.

2.4 Discussion

This new method to quantify fatigue crack damage overcomes the reliance on subjective identification of fatigue crack damage edges [13,18] and manual tracing techniques [13]. In addition, the fatigue crack area is measured, which has not been done for existing techniques such as SAT [21] and transillumination for qualitative evaluation [12]. The measured fatigue crack damage area represents a quantitative result for comparing fatigue crack damage severity between tibial insert specimens. The measurement resolution is dependent on the fatigue crack damage image scale. The fatigue crack damage images for tibial insert 1 and tibial insert 2 have length scale factors of 29 pixels per mm and 28 pixels per mm, respectively. An area difference of 841 pixels for the first fatigue crack damage image and 784 pixels for the second fatigue crack damage image yield changes in area of 1 mm^2, or 4.5% and 2.6% of the respective fatigue crack damage areas. The measurement accuracy when using this technique is dependent on three primary factors. First, if the fatigue crack damage plane is not parallel to the viewing plane during fatigue crack damage image capture, the resulting area projection will underestimate the actual fatigue crack damage area. The orientation of the fatigue crack damage plane relative to the viewing plane in the two tibial inserts that we tested is unknown and warrants further investigation.

Second, the fatigue crack damage area measurement is dependent on accurate detection of the outermost edges of the fatigue crack damage. As demonstrated by the two tibial inserts examined in this work, distinct edges do not necessarily enclose the entire fatigue crack damage area. Figure 2.20 A and B show the first insert, which exhibits a crescent-shaped fatigue crack damage region with an indistinct edge on the concave side of the crescent. The second tibial insert exhibits greater edge continuity, but still exhibits regions where the outer edge is not detected. This effect is visible in Figure 2.22 where the spline forms a jagged edge. This lack of a distinct enclosing edge presents potential for measurement inaccuracies. Noise within the image, which has the potential to be incorrectly categorized as damage, can also contribute to inaccuracies in the fatigue crack damage area from its actual area.

This effect is observable as sections of jagged cubic spline in Figure 2.20 and Figure 2.22 where the spline jumps between the true fatigue crack damage edge pixels and misidentified nondamage edge pixels (identified as noise in Figure 2.22). This problem is reduced, but not completely eliminated, by the use of the Wiener filter during image processing. In the two specimens tested here, the area added or removed by the jagged spline regions due to noise represented only a small portion of the total enclosed area. The jagged spline regions are caused by edge pixels that fall inside or outside of the curve of the fatigue crack damage edge. To evaluate the effect of removing the jagged regions, the contributing edge pixels are identified, based on the associated sharp changes in direction of the piecewise cubic spline segments, and removed. When these pixels are removed, the area within the resulting piecewise cubic spline increases by 0.01 mm^2 for tibial insert 1 and by 0.14 mm^2 for tibial insert 2. This represents a 0.05% and 0.41% change in fatigue crack damage area for tibial insert 1 and tibial insert 2, respectively.

The transillumination technique has not been validated for various fatigue crack damage depths and sizes. The concern regarding the effect of depth on the visibility of fatigue crack damage is partially addressed by the tendency of fatigue crack damage to occur between 1 and 2 mm subsurface, rather than deep within the tibial insert [26,43]. However, further validation with a variety of fatigue crack damage depths is desirable for confirming the robustness of the transillumination based method. Lastly, this method relies on the assumption that increased tibial insert opacity represents fatigue crack damage. However, deformation of the material may result in increases in UHMWPE opacity prior to the formation of macroscopic fatigue cracks.

In spite of these limitations the transillumination and fatigue crack damage edge measurement technique developed here represents a simple and economical method for quantifying fatigue crack damage area and location within tibial insert specimens with greater precision and accuracy than existing subsurface fatigue crack damage measurement methods.

2.5 References

[1] Blunn, G. W., Walker, P. S., Joshi, A., and Hardinge, K., 1991, “The dominance of cyclic sliding in producing wear in total knee replacements,” Clin. Orthop., (274), pp. 253–260.

[2] Blunn, G. W., Joshi, A., Minns, R. J., Lidgren, L., Lilley, P., Ryd, L., Engelbrecht, E., and Walker, P. S., 1997, “Wear in retrieved condylar knee arthroplasties: A comparison of wear in different designs of 280 retrieved condylar knee prostheses,” J. Arthroplasty, **12**(3), pp. 281–290.

[3] Simis, K. S., Bistolfi, A., Bellare, A., and Pruitt, L. A., 2006, “The combined effects of crosslinking and high crystallinity on the microstructural and mechanical properties of ultra high molecular weight polyethylene,” Biomaterials, **27**, pp. 1688–1694.

[4] Medel, F., and Furmanski, J., 2009, “Fatigue and fracture of UHMWPE,” UHMWPE Biomaterials Handbook: Ultra High Molecular Weight Polyethylene in Total Joint Replacement and Medical Devices, Kurtz, S. M., ed., Elsevier Academic Press, New York, NY, pp. 451–472.

[5] Kurtz, S. M., ed., 2009, UHMWPE Biomaterial Handbook: Ultra High Molecular Weight Polyethylene in Total Joint Replacement and Medical Devices, Elsevier Academic Press, New York, NY.

[6] Villarraga, M. L., Kurtz, S. M., Herr, M. P., and Edidin, A. A., 2003, “Multiaxial fatigue behavior of conventional and highly crosslinked UHMWPE during cyclic small punch testing,” J. Biomed. Mater. Res. A, **66A**(2), pp. 298–309.

[7] Haider, H., 2009, “Tribological assessment of UHMWPE in the knee,” UHMWPE Biomaterials Handbook, Academic Press, Inc., New York, NY, pp. 381–408.

[8] Oral, E., Malhi, A. S., and Muratoglu, O. K., 2006, “Mechanisms of decrease in fatigue crack propagation resistance in irradiated and melted UHMWPE,” Biomaterials, **27**, pp. 917–925.

[9] Shibata, N., and Tomita, N., 2005, “The anti-oxidative properties of α-tocopherol in γ-irradiated UHMWPE with respect to fatigue and oxidation resistance,” Biomaterials, **26**(29), pp. 5755–5762.

[10] ISO/IEC, 2009, "Implants for surgery - Wear of total knee-joint prostheses - Part 1: Loading and displacement parameters for wear-testing machines with load control and corresponding environmental conditions for test," ISO 14243-1.

[11] Hamill, J., and Knutzen, K. M., 2009, Biomechanical Basis of Human Movement, Lippincott Williams & Wilkins, Philadelphia, PA.

[12] Muratoglu, O. K., Bragdon, C. R., Jasty, M., O’Connor, D. O., Von Knoch, R. S., and Harris, W. H., 2004, “Knee-simulator testing of conventional and cross-linked polyethylene tibial inserts,” J. Arthroplasty, **19**(7), pp. 887–897.

[13] Harman, M. K., Banks, S. A., and Hodge, W. A., 2001, “Polyethylene damage and knee kinematics after total knee arthroplasty,” Clin. Orthop., **392**, pp. 383–393.

[14] Williams, J. L., Knox, D. A., Teeter, M. G., and Holdsworth, D. W., 2010, "Evidence that in vivo wear damage alters kinematics and contact stresses in a total knee replacement," J. Long. Term Eff. Med. Implants, **20**(1), pp. 43–48.

[15] D'Lima, D. D., Steklov, N., Fregly, B. J., Banks, S. A., and Colwell Jr., C. W., 2008, "In vivo contact stresses during activities of daily living after knee arthroplasty," J. Orthop. Res., **26**, pp. 1549–1555.

[16] Fang, H. W., Hsu, S. M., and Sengers, J. V., 2003, Ultra-high Molecular Weight Polyethylene Wear Particles Effects on Bioactivity, National Institute of Standards and Technology, Washington, D.C.

[17] Brach del Prever, E. M., Bistolfi, A., Bracco, P., and Costa, L., 2009, "UHMWPE for arthroplasty: past or future?" J Orthopaed Traumatol, **10**, pp. 1–8.

[18] Furmanski, J., Kraay, M. J., and Rimnac, C. M., 2011, "Crack initiation in retrieved cross-linked highy cross-linked ultra-high-molecular-weight polyethylene acetabular liners: An investigation of 9 cases," J. Arthroplasty, **26**(5), pp. 796–801.

[19] Cornwall, B. G., Bryant, T. J., Hansson, C. M., Rdan, J., Kennedy, L. A., and Cookey, T. D. V., 1995, "A quantitative technique for reporting surface degradation of UHMWPE components of retrieved total knee replacements," J. Appl. Biomater., **6**, pp. 9–18.

[20] Kurtz, S. M., Peloza, J., and Siskey, R., 2005, "Analysis of a retrieved polyethylene total disc replacement component," Spine J., **5**, pp. 344–350.

[21] Todo, S., Tomita. N., Kitakura, T., and Yamano, Y., 1999, "Effect of sliding locus on subsurface crack formation in ultra-high-molecular-weight polyethylene knee component," Biomed. Mater. Eng., **9**, pp. 13–20.

[22] Teeter, M. G., Yuan, X., Naudie, D. D. R., and Holdsworth, D. W., 2010, "Technique to quantify subsurface cracks in retrieved polyethylene componenets using micro-CT," J. Long. Term Eff. Med. Implants, **20**(1), pp. 27–34.

[23] Furmanski, J., and Rimnac, C. M., 2011, "Crack propagation resistance is similar under static and cyclic loading in crosslinked UHMWPE: A pilot study," Clin. Orthop., **469**(8), pp. 2302–2307.

[24] Loadman, M. J., 1998, Analysis of rubber and rubber-like polymers, Kluwer Academic Publishers, United Kingdom.

[25] Petzow, G., ed., 1999, Metallographic Etching: Techniques for Metallography, Cermaography, Plastography, ASM International, United States of America.

[26] Bell, C., Walker, P. S., Abeysundera, M. R., Simmons, J. M. H., King, P. M., and Blunn, G. W., 1996, "Effect of oxidation on the delamination of ultrahigh-molecular-weight polyetheylene tibial components," J. Arthroplasty, **13**(3), pp. 280–290.

[27] Semitracks, "Acoustic Microscopy," Semit. Semicond. Microelectron. Microsyst. Nanotechnol. Train. [Online]. Available: http://www.semitracks.com/index.php/reference-

material/failure-and-yield-analysis/package-analysis/acoustic-microscopy. [Accessed: 11-Jun-2014].

[28] HDI Solutions, Inc., "Basic principle of a scanning acoustic tomograph." [Online]. Available: http://www.hdi-solutions.com/products/Brochures/SATBasics.pdf. [Acessed: 25-June-2014].

[29] Rasesh, K., 2010, "New developments in x-ray micro-computed tomography technology and its applications to study bone micro-architecture," J. Acoust. Soc. Am., **127**, p. 2006.

[30] Harman, M. K., Markovich, G. D., Banks, S. A., and Hodge, W. A., 1998, "Wear patterns on tibial plateaus from varus and valgus osteoarthritic knees," Clin. Orthop., **352**, pp. 149–158.

[31] Nunez, L., 2013, "Post-Market Surveillance of Total Knee Replacement Combining Clinical Outcomes and Quantitative Image Processing Techniques," M.S. thesis, Bioengineering, Clemson University.

[32] Rawlinson, J. J., Furman, B. D., Li, S., Wright, T. M., and Bartel, D. L., 2006, "Retrieval, experimental, and computational assessment of the performance of total knee replacements," J. Orthop. Res., pp. 1384–1394.

[33] ASTM International, 2008, "Standard practice for accelerated aging of ultra-high molecular weight polyethylene after gamma irradiation in air," ASTM F2003-02.

[34] DesJardins, J. D., Walker, P. S., Haider, H., and Perry, J., 2000, "The use of a force-controlled dynamic knee simulator to quantify the mechanical performance of total knee replacement designs during functional activity," J. Biomech., **33**, pp. 1231–1242.

[35] MathWorks, 2014, "weiner2," MathWorks Doc. Cent. [Online]. Available: http://www.mathworks.com/help/images/ref/wiener2.html. [Accessed: 24-Jul-2014].

[36] Krajsek, K., and Mester, R., 2006, "The Edge Preserving Wiener Filter for Scalar and Tensor Valued Images," Pattern Recognition, K. Franke, K.-R. Müller, B. Nickolay, and R. Schäfer, eds., Springer Berlin Heidelberg, Berlin, Heidelberg, pp. 91–100.

[37] MathWorks, 2014, "Remove noise from images," MathWorks Doc. Cent. [Online]. Available: http://www.mathworks.com/help/images/remove-noise-from-images.html. [Accessed: 24-Jul-2014].

[38] MathWorks, 2014, "edge," MathWorks Doc. Cent. [Online]. Available: http://www.mathworks.com/help/images/ref/edge.html. [Accessed: 24-Jul-2014].

[39] Canny, J., 1986, "A computational approach to edge detection," IEEE Trans. Pattern Anal. Mach. Intell., **PAMI-8**(6), pp. 679–698.

[40] Green, W. E., 2002, "Canny edge detection tutorial," Drexel Univ. Auton. Syst. Lab [Online]. Available: http://dasl.mem.drexel.edu/alumni/bGreen/www.pages.drexel.edu/_weg22/can_tut.html. [Accessed: 24-Jul-2014].

[41] Wyman, C., 2008, "Canny edge detection," Top. Graph. Adv. OpenGL Render. [Online].

Available: http://homepage.cs.uiowa.edu/~cwyman/classes/spring0822C251/homework/canny.pdf. [Accessed: 24-Jul-2014].

[42] Killip, S., Mahfoud, Z., and Pearce, K., 2004, "What is an intracluster correlation coefficient? Crucial concepts for primary care researchers," Ann. Fam. Med., **2**(3), pp. 204–208.

[43] Bartel, D. L., Bicknell, V. L., and Wright, T. M., 1986, "The effect of conformity, thickness, and material on stresses in ultra-high molecular weight components for a total joint replacement," J. Bone Joint Surg. Am., **68**, pp. 1041–1051.

CHAPTER 3

FINITE ELEMENT SIMULATION

3.1 Background

The location of fatigue crack damage observed in the tibial insert is related to the magnitude and location of the external loading and the corresponding internal stress. The stress in the tibial insert results from contact between the condyles of the tibial insert and those of the femoral component. Because local stress within the tibial insert is difficult to measure experimentally, computer simulation methods are frequently used to calculate the local stress inside the tibial insert under specific loading scenarios [1–19]. Common simulation techniques include rigid body modeling of the prosthetic knee joint components for predicting the kinematics of the prosthetic knee joint [11,13,15], elastic foundation modeling for predicting both kinematics and contact pressure [13,17,18], and finite element modeling for predicting kinematics, contact pressure, and local stress and strain inside the material [3,4,6–9,11–14,16]. For the purpose of this work, which focuses on predicting UHMWPE tibial insert stress associated with subsurface fatigue cracking, a finite element simulation is used.

3.1.1 Finite Element Mesh and Element Selection

The finite element method is a numerical technique for finding approximate solutions to boundary value problem differential equations. The technique is suitable for a geometrically complex solution domain because the domain is broken into multiple discrete elements and connecting nodes. The unknown solution to the differential equation is calculated exactly at the nodes, and interpolated through each element according to a prescribed shape function. We are interested in finding the unknown stress and strain inside the tibial insert for a specific external loading [20]. The shape function associated with each element determines how the nodal solution is interpolated inside that element, and limits the polynomial order of the solution that the element can accurately model. For instance, a single element with a linear shape function can only exactly model a linear solution. However, multiple linear elements in series can approximate a higher order solution [20]. In finite element analysis one must use either elements with a shape function of sufficiently high polynomial order or use a sufficient number of lower-order elements to achieve a satisfactory approximation of the exact solution. The discrete set of elements that compose the solution domain are commonly referred to as the model "mesh" [20].

The complex geometry and contact conditions experienced in a prosthetic knee joint simulation require use of elements with high order shape functions, and/or a refined mesh in regions of the solution domain where steep local stress and strain gradients occur. The specific number of elements is unique to the scenario being modeled and, thus, varies throughout the prosthetic knee joint simulations in the literature [4–7,10–16]. In most cases, eight or ten-node tetrahedral elements with a sufficiently high-order shape function are selected to achieve a converged solution for the quantity of interest [6,7,10,11,13–16]. Tetrahedral elements are a good choice because they can approximate the complex geometry of the curved condyles of the tibial insert.

3.1.2 Commonly Modeled Scenarios and Corresponding Boundary Conditions

One significant challenge in calculating the local stress and strain in the tibial insert through finite element analysis is selecting accurate boundary conditions to effectively capture the complex loading and displacement conditions that occur in vivo. Variations in the knee joint forces induced by muscular action, ligament and joint capsule tension, and transmitted ground reaction forces [21], in addition to variations of the location where those forces act [22], the surgical positioning of the implant components [5], and variations in the quality of the UHMWPE used in the tibial insert [22] all contribute to discrepancies between the calculated strain and stress and the actual in vivo performance of a selected tibial insert geometry [1].

Previous research documented in the literature has focused on modeling two primary load and displacement scenarios. The first scenario is the simulation of actual displacement and loading experienced by the knee joint in vivo. This approach requires the measurement or indirect calculation of the loading and displacement of the prosthetic knee joint articulating surfaces. For example, D'Lima et al. [2] used an instrumented tibial insert to measure the contact pressure on the surface of the tibial insert and calculated the net compressive load on the tibial insert. In their technique the corresponding knee joint kinematics (displacements and rotations) are obtained via fluoroscopic imaging, a common technique in which x-rays are used to film a dynamic event [2,6,14]. The subject-specific prosthetic knee joint loads and kinematics are then used in the finite element model. While this potentially allows for an accurate comparison between simulated deformation and wear and experimentally determined deformation and wear in a retrieved tibial insert, the method suffers from weaknesses in the fluoroscopic measurement of the knee joint kinematics, including difficulty in accurately evaluating out-of-plane displacement and rotation of the prosthetic knee joint components [2]. The second commonly simulated scenario is a prosthetic knee joint loaded in a knee simulator [23]. This approach has been used in several studies because displacements and forces used in knee simulators are more easily and accurately measured than those occurring in vivo [7,11,13,16]. In addition, the simulation results can be validated with experiments. Halloran et al. [13] performed a rigid-body simulation using gait cycle data from the ISO 14243-1 standard for prosthetic knee joint wear testing in a knee simulator [23] to calculate prosthetic knee joint kinematics, contact area between the articulating surfaces, and contact pressure, and compared these to experimental measurement of the same parameters. Their results demonstrated that a finite element model using force-control inputs according to ISO 14243-1

[23] accurately predicts the experimentally measured results [13]. A similar study performed by Knight et al. [11] confirmed that both force-control inputs and displacement-control inputs can be used as finite element boundary conditions to accurately simulate the kinematics and loading of a knee simulator wear test. Although using knee simulator data limits the possible simulation scenarios to a standardized gait cycle, and potentially neglects discrepancies between standardized and in vivo loading, it presents the most direct comparison between experiments and simulation models. This allows for comparison between different prosthetic knee joint designs under the same precisely controlled experimental and simulated loading conditions without the additional complication of patient-specific kinetics and kinematics. In this thesis, the simulated loading of the prosthetic knee joint is based on recorded force and displacement data from the knee simulator testing discussed in Chapter 2.

3.1.3 UHMWPE Material Model

Another major consideration in finite element modeling of tibial insert strain and stress during a simulated loading scenario is selecting a material model that accurately represents the constitutive behavior of the UHMWPE and cobalt-chromium components of the prosthetic knee joint. Several different UHMWPE material models have been employed in the literature. These range from a simple linear elastic model [17,18] to more complex models such as the hybrid model [1,19] and the holistic strain hardening wear model [3].

3.1.3.1 Conventional Material Models

The simplest model treats UHMWPE as a linear elastic material. For that case, Hooke's law holds true and plastic deformation is not taken into account [24], i.e.,

$$\sigma = E\varepsilon \tag{3.1}$$

Fregly et al. applied a linear elastic material model to two simulations: 1) simulation of a prosthetic knee joint under walking gait conditions based on fluoroscopic kinematics [18] and 2) simulation of a prosthetic knee joint under quasistatic displacement and loading conditions based on a prosthetic knee joint mechanical test apparatus [17]. In both cases the simulated stress in the tibial insert is compared to surface damage observed in a retrieved tibial insert of the same geometry. In both simulations, they used rigid body dynamics with deformable body contact to predict the contact pressure between the articulating surfaces of the contacting bodies [17]. These simulations documented a closer agreement between predicted and experimentally measured contact pressure when a linear, as opposed to a nonlinear, elastic material model is used to model the prosthetic knee joint under quasistatic loading. In a second study [18], they demonstrated that the nonlinear elastic material model produces a more uniform contact pressure across a larger area than that produced by the linear elastic model and, thus, is likely to predict a larger adhesive-abrasive wear and creep damage area. However, the use of a nonlinear elastic material model would not cause significant changes in the location and depth of the predicted adhesive-abrasive wear and creep damage, compared to results obtained with the linear elastic material model.

Halloran et al. [13] also simulated contact between the femoral component and tibial insert during walking gait. Their justification for using a linear elastic model was based on the well-documented values in the literature for the elastic modulus and Poisson coefficient of UHMWPE, which are the only two parameters needed in a linear elastic model. The results of the simulations by Fregly et al. [17,18] and Halloran et al. [13] indicated that a linear elastic material model may be sufficient for accurately predicting strain and stress within the tibial insert for conditions in which the magnitude of the local strain remains within the elastic limit and strain rates are low, such that strain rate effects can be neglected. An additional comparison between experimental stress-strain data and linear elastic model simulation results performed by Kurtz [1] showed that the linear elastic model becomes less accurate when examining time-dependent responses, large deformation failure, or cyclic loading behavior. Figure 3.1 shows a plot of a typical tensile stress-strain curve for UHMWPE superimposed with a plot of the response predicted by a linear elastic model with an elastic modulus matching that of the UHMWPE linear

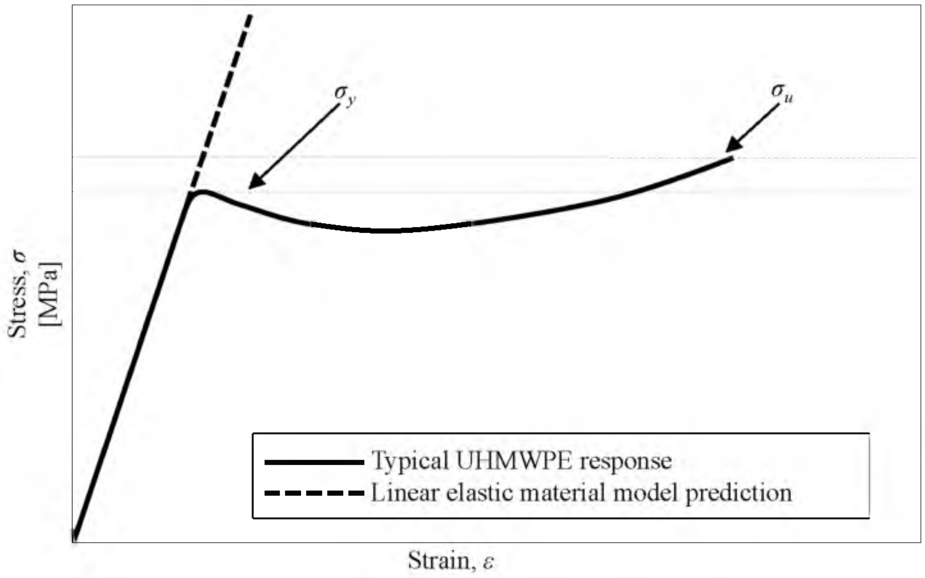

Figure 3.1: Typical stress-strain curve for UHMWPE and predicted stress-strain curve for a linear elastic model with an elastic modulus matching that of UHMWPE in the linear stress-strain region. Adapted from [1].

stress-strain region. This plot demonstrates the inaccuracy of the linear elastic UHMWPE material model prediction at stress beyond the elastic limit, from the UHMWPE yield stress σ_y until the ultimate tensile stress σ_u.

Another commonly used material model for UHMWPE is the isotropic plasticity model. The term isotropic indicates that the material properties are the same in all orientations [24]. Plasticity indicates that the reversible linear loading and unloading behavior represented by Hooke`s law for linear elastic materials no longer holds true and is replaced by a stress-strain relationship that accounts for the development of irreversible strain in the material when a stress threshold (the yield stress) is exceeded [25]. Under biomechanically realistic loading conditions the high contact stress induced by the nonconformity between the femoral and tibial contact surfaces of the prosthetic knee can exceed the threshold at which plastic deformation begins, making models which account for plastic deformation necessary for accurately predicting the behavior of the UHMWPE [1].

The simplest isotropic plasticity model is the perfectly plastic model. This model predicts increasing plastic deformation due to incremental strain under constant stress once the yield stress of the UHMWPE is exceeded. The behavior prior to the yield stress is predicted by an elastic material model, such as the previously described linear elastic material model. Figure 3.2 shows a plot of a typical UHMWPE stress-strain curve and of a stress-strain curve predicted by a linear elastic perfectly plastic material model. Strain hardening and rate dependency are not considered. The difference in stress-strain behavior between the linear elastic perfectly plastic material model and the actual UHMWPE behavior becomes more critical at large strains where strain hardening occurs due to straightening and alignment of the polymer chains [1]. This model over-predicts residual plastic deformation after unloading. This over-prediction is caused by the use of linear unloading, which overestimates permanent plastic deformation relative to that predicted by the actual nonlinear unloading behavior of the UHMWPE.

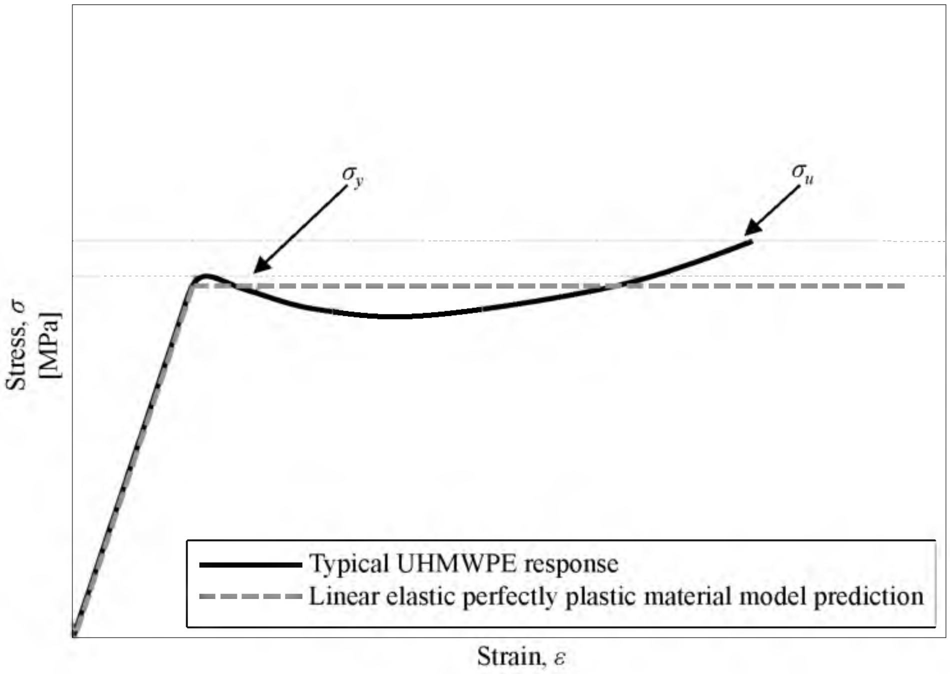

Figure 3.2: Typical stress-strain curve for UHMWPE and predicted stress-strain curve for a linear elastic perfectly plastic model.

Figure 3.3 shows a plot of typical UHMWPE nonlinear loading and unloading behavior and the linear unloading behavior predicted by the perfectly plastic model in terms of true stress and true strain. The difference in shape between the two unloading curves is shown, with the resulting difference in permanent plastic true strain indicated.

A more complex isotropic plasticity model is the J_2-plasticity model, which uses the von Mises yield criterion and assumes rate-independent isotropic hardening. Hardening is the change in the yield stress depending on the material`s loading history. The J_2-plasticity model considers uniaxial tension data and models the material response through a piecewise linear approximation [1]. Figure 3.4 shows a plot of a typical UHMWPE stress-strain curve and of a stress-strain curve predicted by a J_2-plasticity model.

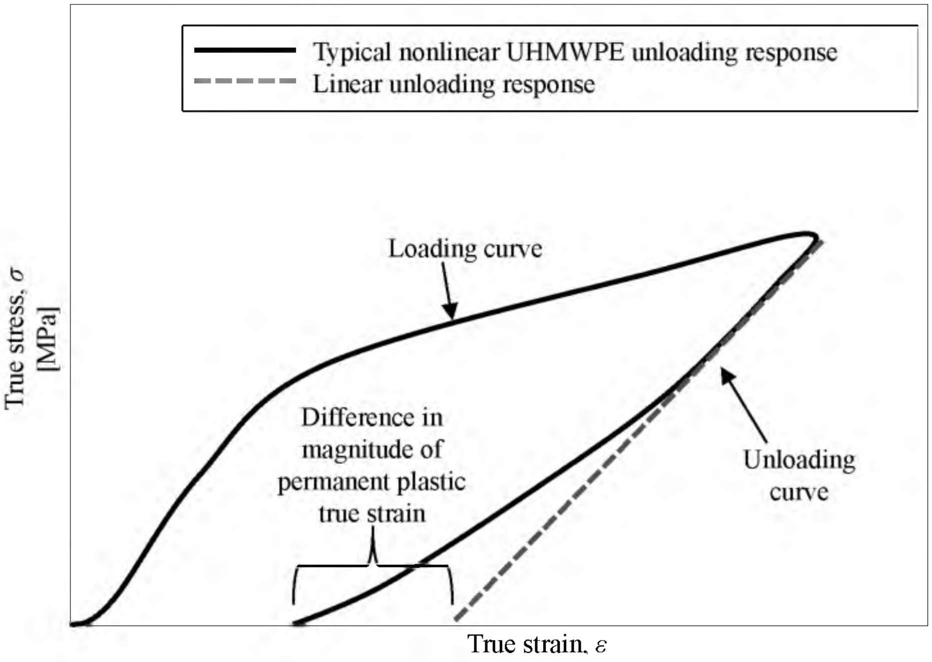

Figure 3.3: Difference in permanent plastic true strain predicted by typical UHMWPE nonlinear unloading behavior and modeled linear unloading behavior. Adapted from [26].

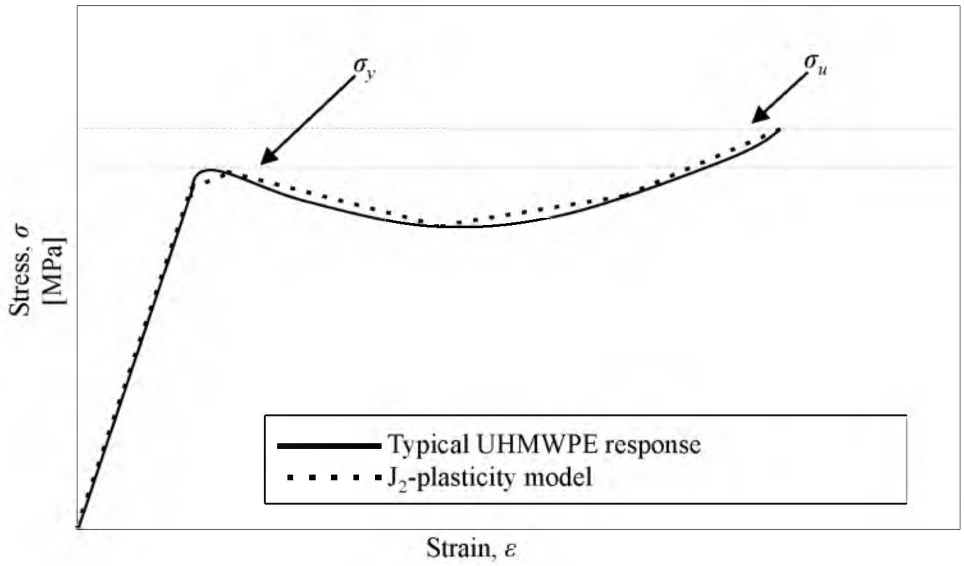

Figure 3.4: Typical stress-strain curve for UHMWPE and predicted stress-strain curve for a piecewise linear J_2-plasticity model. Adapted from [1].

This model can accurately predict strain results for UHMWPE at strains below the large-deformation-to-failure region, but performs poorly when used to predict cyclic strain results due to its prediction of purely linear unloading behavior [19], similar to the previously described perfectly plastic material model. In the case of the J_2-plasticity model, a linear unloading curve can result in over-prediction of permanent plastic deformation by over 200% [26]. In addition, the isotropy assumed in this model may not be accurate for UHMWPE under some loading scenarios due to polymer chain alignment, crystallographic slip, and changes in lamellar orientation [1]. In spite of these limitations the J_2-pasticity model has been used extensively in prosthetic joint simulations [6,7,16,27].

Godest et al. [16] used a J_2-plasticity model to predict prosthetic knee joint kinematics and contact stress under knee simulator loading. They acknowledged that the use of the J_2-plasticity model in their simulation represented a simplification of the true material behavior of UHMWPE, but justified it as a realistic approximation of the material behavior for situations with negligible loading rate effects. The J_2-plasticity model has also been used in combination with

Archard's wear law [28]. In finite element simulations Archard's law is used to calculate wear at the model nodes based on an experimentally measured wear constant, the sliding distance between the contacting element nodes, and the nodal contact pressure. The nodal wear can then be used to calculate the total wear volume via integration over the contact area [7].

A third UHMWPE material model is the linear viscoelastic model [1,29]. Linear viscoelasticity expands upon the linear elastic model by adding time-dependent viscous behavior. Under cyclic loading the addition of viscous behavior will result in a phase lag between the applied stress and the resulting strain. The relationship between the stress and strain can be represented by the material's dynamic modulus G, which is a function of the storage G' and loss G'' moduli [30].

$$G = G' + iG'' \tag{3.2}$$

where $i = (-1)^{0.5}$. The storage and loss moduli are then related to the phase lag δ as

$$G' = \frac{\sigma}{\varepsilon}\cos\delta \tag{3.3}$$

and

$$G'' = \frac{\sigma}{\varepsilon}\sin\delta \tag{3.4}$$

where σ and ε are the nominal stress and strain, respectively.

The viscoelastic material model accounts for three types of mechanical behavior that are neglected in a linear elastic model. These are 1) stress-strain curve hysteresis, 2) stress relaxation, and 3) creep. Hysteresis can be observed in the loading and unloading portions of the stress-strain curve for the viscoelastic material. The shape of the stress-strain curve is different for the loading and unloading portions due to the stress-strain phase lag, forming a loop-shape rather than a single stress-strain curve where the loading and unloading portion collapse on each other [31]. Stress relaxation occurs when a constant strain is applied to a material and the stress in the material gradually decreases [30]. Creep is similar, but involves gradually increasing strain at a constant applied stress [30]. The significance of including the viscoelastic properties of stress-strain curve hysteresis, stress relaxation, and creep in the UHMWPE material model depends upon the loading conditions being modeled.

Rullkoetter et al. [29] used a viscoelastic model in their simulation of a prosthetic knee joint under loading. They studied progressive and steady state loading and examined the effects of time-dependent material behavior on the maximum surface normal contact stress and subsurface Tresca stress during sustained loading. The Tresca plasticity model predicts yielding when the maximum shear stress reaches a magnitude of half the yield stress or half the difference between the maximum and minimum principal stress [32]. They observed that stress relaxation reached a magnitude of approximately 25% for both surface and subsurface stress and that contact area increased by nearly 30% during the two-minute simulation, with creep displacement of approximately 50% of the initial displacement after two minutes. After unloading, the material returned to its unloaded displacement profile [29]. These findings indicate that creep and relaxation become more significant with longer periods of load application. During testing in a knee simulator the loading cycle occurs at a frequency of 1 Hz [23], similar to walking gait, which means sustained loading such as that modeled by Rullkoetter et al. is unlikely during gait and both creep and relaxation effects will be less severe than what was reported in this study.

Quinci et al. [33] further examined the use of a linear viscoelastic model with an emphasis on in vivo operating conditions. Sustained compression loading and recovery testing was performed for a set of prosthetic knee joints. During this testing the contact area, deformation of the contact surface, and pressure were measured. Finite element simulations of the same loading and recovery conditions were performed using three UHMWPE material models: linear elastic, elastic-plastic, and linear viscoelastic. Upon comparison of the experimental and finite element analysis results Quinci et al. found that creep deformation had a significant effect on experimental and simulated contact pressures [33]. In addition, the linear viscoelastic model resulted in greater deformation under sustained compressive loading, which is in closer agreement to the experimental observations than when using an elastic-plastic material model. This effect was due to viscoelastic creep during the 20,000-second sustained loading trial. At high compressive loads the plastic response became more significant, and the viscoelastic model was unable to fully capture the material response [33]. Permanent plastic deformation and creep deformation were observed at each of the tested loading configurations, indicating that plastic and viscoelastic material responses are important under sustained loading at physiologically realistic load magnitudes.

These results from the literature suggest that the consideration of viscoelastic behavior may be important for accurate prediction of contact stress under in vivo and knee simulator loading conditions. A linear viscoelastic model can accurately model the behavior of UHMWPE, although the model's accuracy deteriorates when strain exceeds the yield strain and at high strain rates [1]. The linear viscoelastic material model predicts the material behavior more accurately than an elastic-plastic model under sustained application of relatively low compressive loads that do not substantially exceed the yield stress, although the UHMWPE stress due to high compressive loads may be most accurately modeled if plastic behavior is included [1,34].

3.1.3.2 Advanced Material Models

Other models address the limitations of the linear elastic, isotropic plastic, and linear viscoelastic material models by incorporating large strain, time dependent behaviors and anisotropy. The current state-of-the-art advanced UHMWPE material model is the hybrid model [1,19,35,36]. This model was developed to predict local stress and strain in tibial inserts undergoing cyclic loading. It incorporates rate effects, anisotropy under large deformation, and viscoplastic behavior by considering how the response of UHMWPE at the molecular level influences macroscale behavior [1]. The hybrid model has been validated for extrusion molded conventional [19,35,36] and highly cross-linked [35,36] UHMWPE under multi-axial monotonic and cyclic load conditions and provides much more accurate predictions than the J_2-plasticity model and several simpler constitutive models [19]. This model represents the ideal model for extremely accurate prediction of UHMWPE stress-strain behavior. However, it requires thirteen material parameters to achieve this high level of accuracy and is computationally complex.

Recently, several additional complex models that incorporate adhesive-abrasive wear behavior along with history-dependent anisotropy, creep, and strain hardening properties of UHMWPE have been developed [3,11,34,37-42]. Knight et al. [11] tested a finite element simulation adaptive remeshing model based on Archard's wear law for predicting UHMWPE tibial insert wear. Finite element simulations of force controlled and displacement controlled knee simulator wear testing using this material wear model produced adhesive-abrasive wear results similar to those produced through experimental knee simulator wear testing. However, concerns exist regarding the use of Archard's wear law, as this wear model was developed for metallic materials and may not always accurately represent the behavior of polymeric materials such as UHMWPE [40]. More recently, a wear model that includes strain hardening and creep was developed [3]. The wear coefficient for strain hardened and not strain hardened surfaces and surfaces influenced by creep were tuned to experimental wear data, and similar wear volumes were observed in the simulation and experimental results below 3.5 million cycles. Most recent models have used similar methods with the additions of more specific cross-shear parameters [37,38], further emphasis on the viscoelastic creep response as an important factor in adhesive-abrasive wear [33], consideration of sliding kinematics in wear [39], and contact-pressure independent wear factors [40].

Development in the area of fatigue crack wear simulation has been less advanced than that of adhesive-abrasive wear simulation, in spite of the association between fatigue crack wear and extensive femoral and tibial osteolysis [22]. However, there are several fatigue crack simulation studies that have examined the relationship between predicted stress and experimental fatigue crack results. One way in which the stress and fatigue crack relationship has been examined is by simulating an idealized sliding contact scenario and comparing the results to experimental results for a sliding indenter test [41]. In this case a flat UHMWPE plate contacted by a sliding cobalt alloy indenter was considered, where the UHMWPE plate was modeled with a quadrilinear isotropic strain hardening material model similar to the J_2-plasticity model. The indenter was modeled as a rigid body. The loading and sliding cycle was repeated five times until a steady state for stress and deformation was reached. The simulation stress results were compared to stereo-micrographs of fatigue crack damage induced by experimental testing using the same sliding indenter scenario over 952,000 cycles. It was observed that fatigue crack damage in the experimentally tested UHMWPE plates corresponded to the locations of maximum principal stress seen in the simulation, which occurred on the medial and lateral edges of the indenter path. Additionally, once steady state was achieved, residual surface stress contributed significantly to the total stress observed during the loading and sliding cycle [41].

In another study by Sathasivam et al. [42] a similar simulation was performed with a prosthetic knee joint in place of a sliding indenter. Two prosthetic knee joint geometries were modeled using quasistatic analyses at discrete points for every 2% increment of the gait cycle. The tibial insert was modeled with a linear-elastic material model. Predictive damage scores were calculated based on the cumulative shear stress results, based on previous work by Bartel et al. [43]. Fatigue crack initiation and small crack propagation was associated with cyclic shear stress. The damage function for each element was defined as

$$\sum_{i=1}^{i=T-1} \left|S_{i+1} - S_i\right| \times 0.5\left(\left|S_{i+1}\right| + \left|S_i\right|\right) \tag{3.5}$$

where S_1 and S_T are the first and last points of the element's stress history [42]. For both simulated prosthetic knee joint geometries the maximum damage scores were located on the medial condyle of the tibial insert. The magnitude of the maximum damage score varied based on the degree of congruency between the tibial insert and femoral component, with high congruency being associated with a lower damage score. Validation was not performed, due to the difficulty of matching the loading and kinematic conditions of retrieved tibial inserts to those used in the simulation.

Both a material model's ability to accurately represent a material's behavior and the material model's computational cost must be considered when selecting the best material model for a given simulation. Although the hybrid model has been shown to most accurately replicate UHMWPE behavior, simpler models may provide sufficient information with lower computational impact as long as the limitations of these models are considered.

For this work two material models are selected. A linear elastic model is selected as the initial material model based on relatively low computational cost. This model is most accurate in the linear region of the UHMWPE stress-strain curve, where the yield stress is not exceeded, and becomes less accurate above this region, where permanent plastic strain becomes significant. In order to capture the time-dependent response of UHMWPE during gait simulator conditions, a second simulation is performed using a linear viscoelastic material model. This model includes effects of creep on the change in contact area between the femoral component and tibial insert during sustained loading. The results of the two simulations are compared to determine the effect of viscoelastic behavior on the predicted stress locations and magnitudes. It is expected that the linear elastic material model will over-predict material stiffness and under-predict deformation in the contact region for prolonged stress (viscoelastic creep) and at stress above the yield stress (plastic deformation).

3.2 Methods

The two simulations performed in this work model a single gait cycle of the knee simulator testing performed on the first tibial insert. To minimize computational cost, this simulation is limited to the stance phase, i.e., the 60-65% of the gait cycle during which the foot is in contact with the ground, as opposed to the swing phase, when the foot is not in contact with the ground. The knee experiences significantly greater tibial loading during the stance phase than during the swing phase [44]. We perform a dynamic simulation of the stance phase, as opposed to a quasistatic simulation. The key difference is that the dynamic simulation allows modeling the entire motion of the prosthetic knee joint during the stance phase, whereas a quasistatic simulation requires that the prosthetic knee joint be constrained to a certain position and loaded until static equilibrium is achieved, essentially simulating a single snapshot of the stance phase. Precise timing of when the maximum stress occurs during the gait cycle is impractical to measure in vivo, and has not yet been reported [44,45]. In addition, tibio-femoral contact stress varies based on the geometry of the tibial insert and femoral component and the specific loading, such as knee simulator versus subject-specific in vivo kinetics and kinematics.

3.2.1 Geometry

The geometry specific to the prosthetic knee joint evaluated in the knee simulator experiment is imported into Abaqus, a commercial finite element analysis software package used in this work, as a computer-aided design (CAD) file. The geometry is simplified by eliminating features that are not relevant to the contact and strain/stress analysis. The simplification reduces the computational cost of the simulation, without altering the contact geometry between both components. Figure 3.5 illustrates the original (Figure 3.5 A) and simplified (Figure 3.5 B) tibial insert and femoral component geometry.

3.2.2 Mesh and Material Parameters

Table 3.1 lists the materials and corresponding properties used in the simulations. The initial simulation uses a linear elastic material model for the UHMWPE tibial insert, which is fully defined by the yield stress, Poisson’s ratio, and elastic modulus listed in Table 3.1. These material parameters are based on tensile test data. The stress-strain response of UHWMPE is identical for tension and compression up to 12% strain [1]. The second simulation employs a linear viscoelastic material model, which uses both the UHMWPE elastic parameters listed in Table 3.1 and additional viscous behavior parameters, provided in Table 3.2.

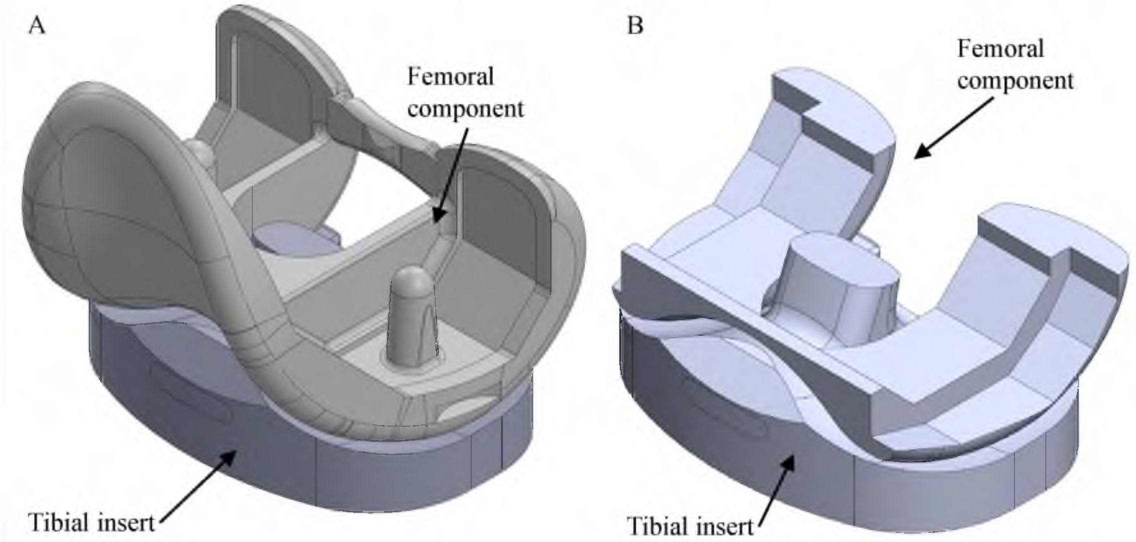

Figure 3.5: CAD model of the tibial insert and femoral component. (A) Original geometry and (B) simplified implant geometry.

Table 3.1: Material properties for the materials used in the finite element model.

Material	Elastic modulus [MPa]	Poisson's ratio	Density [kg/m^3]
Cobalt-chromium	210,000 *	0.300 **	8,300 **
UHMWPE	819 ***	0.473 ***	945 ***

* Value obtained from [46]

** Value obtained from [47]

*** Value obtained from manufacturer

Table 3.2: Time domain frequency parameters defining the linear viscoelastic material model via a two-term Prony series in Abaqus. These inputs are calculated from elastic storage and loss modulus data from [49].

$g^*_{\Re}(f)$	$g^*_{\Im}(f)$	$k^*_{\Re}(f)$	$k^*_{\Im}(f)$	f [Hz]
0.13927	0.30362	0.13927	0.30362	0.1
0.11838	0.23398	0.11838	0.23398	0.3
0.10097	0.16435	0.10097	0.16435	1.0
0.06964	0.02507	0.06964	0.02507	10.0

3.2.2.1 Calculation of Parameters for Linear Viscoelastic UHMWPE Material Model

The parameters listed in Table 3.2 allow Abaqus to create a two-term Prony series approximation (further discussed in Section 3.2.2.2), which describes the viscoelastic material behavior [48]. The input parameters consist of the frequency domain shear and bulk moduli broken down into their real and imaginary components, indicated with subscripts $\Re$ and $\Im$, respectively, i.e., $g^*_{\Re}(f)$, $g^*_{\Im}(f)$, $k^*_{\Re}(f)$, and $k^*_{\Im}(f)$, with f the frequency at which each set of frequency domain shear and bulk modulus data are obtained. The input parameters are calculated from the frequency-dependent elastic storage $E'(f)$ and loss $E''(f)$ moduli reported for GUR 1020 at 37° C for different loading frequencies $0.1 \leq f \leq 100$ Hz [49]. These data are selected for use in the material model based on the similarity between the material properties of GUR 1020 and GUR 1050 and the identical temperature at which the knee simulator testing described in this work is performed. We selected elastic modulus data obtained at four frequencies, 0.1, 0.3, 1.0 and 10.0 Hz, for calculating the Abaqus input parameters $g^*_{\Re}(f)$, $g^*_{\Im}(f)$, $k^*_{\Re}(f)$, and $k^*_{\Im}(f)$.

Although the simulated gait cycle is limited to a frequency of 1 Hz, the individual elements may undergo loading at higher frequencies due to the rapid movement of the contact area between the femoral component condyles and tibial insert condyles and rapid load application occurring during portions of the gait cycle. In addition, data from a minimum of four frequencies are required to calculate a Prony series with a sufficient number of terms. Kurtz et al. [1] documented that a two-term series is sufficient for approximating the viscoelastic behavior of UHMWPE. The Prony series approximation is discussed further in Section 3.2.2.2.

The steps used in this work for calculation of the Abaqus input parameters are:

- **Step 1**: Calculate the frequency domain shear storage modulus $G'(f)$ and loss modulus $G''(f)$ and frequency domain bulk storage modulus $K'(f)$ and loss modulus $K''(f)$ using Equations (3.6), (3.7), (3.8), and (3.9).
- **Step 2**: Calculate the monotonic shear modulus G_∞ and bulk modulus K_∞ from the elastic modulus E and Poisson's ratio ν using Equation (3.10) and (3.11).
- **Step 3**: Apply the values calculated in Steps 1 and 2 to Equations (3.12), (3.13), (3.14) and (3.15) to obtain the Abaqus input parameters.

Step 1 uses $E'(f)$ and $E''(f)$ to calculate the frequency domain shear storage modulus $G'(f)$ and loss modulus $G''(f)$, i.e.,

$$G'(f) = \frac{E'(f)}{2(1+\nu)} \tag{3.6}$$

$$G''(f) = \frac{E''(f)}{2(1+\nu)} \tag{3.7}$$

where ν is the Poisson's ratio, E' is the measured frequency-dependent elastic storage modulus, and E'' is the measured frequency-dependent elastic loss modulus. The frequency domain bulk storage modulus $K'(f)$ and loss modulus $K''(f)$ are calculated as

$$K'(f) = \frac{E'(f)}{3(1-2\nu)} \tag{3.8}$$

$$K''(f) = \frac{E''(f)}{3(1-2\nu)} \tag{3.9}$$

In Step 2, the monotonic shear modulus G_∞ and bulk modulus K_∞, defined as the moduli for time approaching infinity and a frequency approaching zero Hertz, are calculated as

$$G_\infty = \frac{E}{2(1+\nu)} \tag{3.10}$$

$$K_\infty = \frac{E}{3(1-2\nu)} \tag{3.11}$$

In Step 3, the monotonic shear and bulk moduli and frequency-dependent shear and bulk storage and loss moduli are used to calculate the real and imaginary components of the frequency-dependent shear and bulk moduli as

$$g^*_{\Im}(f) = 1 - \left(\frac{G'(f)}{G_\infty}\right) \tag{3.12}$$

$$g^*_{\Re}(f) = \frac{G''(f)}{G_\infty} \tag{3.13}$$

$$k^*_{\Im}(f) = 1 - \left(\frac{K'(f)}{K_\infty}\right) \tag{3.14}$$

$$k^*_{\Re}(f) = \frac{K''(f)}{K_\infty} \tag{3.15}$$

Abaqus then fits the input data to a Prony series with N number of terms, where N is equal to half the number of frequencies f for which data are input. For example, here we use data from four frequencies to get a two-term Prony series.

3.2.2.2 Background on Prony Series Calculation in Abaqus

The Prony series method fits a power series of exponential relaxation functions to the provided frequency-dependent parameters from Step 3 [1]. The Prony series representation of the stress relaxation shear modulus is

$$G(f) = G_\infty + \sum_{i=1}^{N} G_i \left[\frac{1}{i\tau_i f + 1}\right] \tag{3.16}$$

in the frequency domain [49]. G_i and τ_i are the Prony series material parameters, and f is the frequency. The storage modulus $G'(f)$ and loss modulus $G''(f)$, are related to the Prony series parameters by

$$G'(f) = G_0\left[1 - \sum_{i=1}^{N} G_i\right] + G_0\sum_{i=1}^{N}\frac{G_i\tau_i^2 f^2}{1+\tau_i^2 f^2} \tag{3.17}$$

and

$$G''(f) = G_0\sum_{i=1}^{N}\frac{G_i\tau_i^2 f^2}{1+\tau_i^2 f^2} \tag{3.18}$$

respectively, where G_0 is the instantaneous shear modulus and N is the number of terms in the Prony series [48]. This process is performed by the Abaqus software for the user-provided data calculated in Section 3.2.2.1, the desired number of Prony terms N, and the acceptable root mean square (RMS) error between the data and the Prony series curve. Initial Prony series parameters are applied in Abaqus to obtain initial storage and loss modulus values, and are then iteratively adjusted until an acceptable error between the calculated and measured values is achieved. Analogous procedures are used to obtain the corresponding bulk moduli $K'(f)$ and $K''(f)$ [47]. We have specified the allowable RMS error for the Prony curve data fit as 0.175 MPa in this work.

In our simulations the femoral component is defined as a rigid body by converting the modeled geometry to a rigid body shell to reduce the computational cost while maintaining sufficient accuracy, because the elastic modulus of the cobalt-chromium is several orders of magnitude larger than that of the UHMWPE [15].

3.2.2.3 Meshing the Tibial Insert and Femoral Component

Figure 3.6 shows the mesh of the femoral component and tibial insert used in the finite element model. Figure 3.6 A shows the finite element mesh of the rigid body femoral component, which uses a free mesh with a mixture of zero-thickness linear triangular and quadrilateral shell elements to conform to the complex geometry of the femoral component. The free mesh algorithm allows Abaqus to determine the best mesh organization over the modeled component within the element type and size parameters provided by the user.

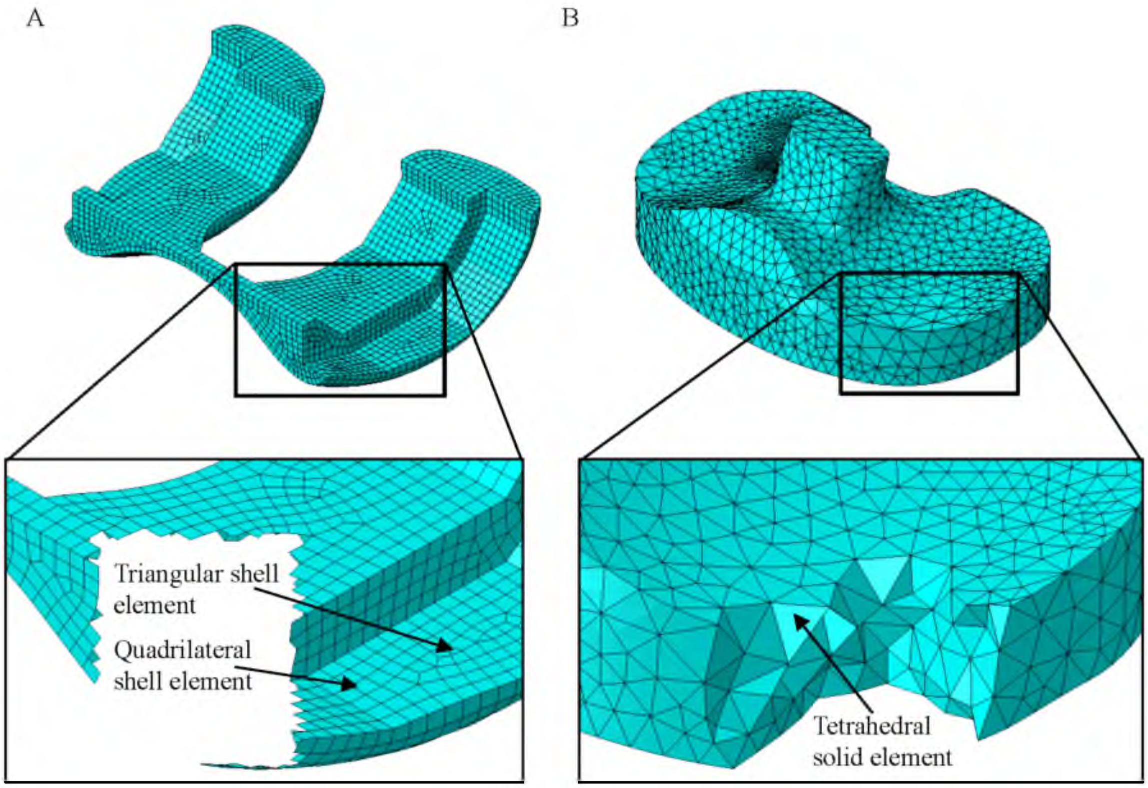

Figure 3.6: Element types for the prosthetic knee joint components. (A) Triangular and quadrilateral zero-thickness rigid shell elements for the femoral component. The magnified view shows the anterior-lateral part of the femoral component. (B) Ten-node quadratic tetrahedral element tibial insert mesh.

The magnified view inset of Figure 3.6 A, shows both triangular and quadrilateral elements on the curved surface of the femoral component, and highlights the necessity of using two different element shapes. Some elements are removed in the magnified view to display the zero-thickness element shape. Since nodal stress results are not calculated for elements that compose rigid bodies, zero-thickness linear shell elements are sufficient [15]. The tibial insert is modeled with modified quadratic tetrahedral elements, which are specified as element type C3D10M in Abaqus [51]. Figure 3.6 B shows the tetrahedral shape of these elements, which allows the mesh to conform to the complex geometry of the tibial insert. Additionally, the modified formulation ensures that, under uniform contact pressure, the resulting forces at each of the element`s nodes are also uniform, modeling realistic contact behavior [51]. The magnified view in Figure 3.6 B shows the anterior-lateral part of the tibial insert with some elements removed to display element shape.

3.2.3 Loading and Displacement Boundary Conditions

The boundary conditions are based on the displacement and loading described in the ISO 14243-1 standard for wear-testing of prosthetic knee joints [23] and experimental test data from the knee simulator testing of the tibial insert (see Appendix C). Displacement boundary conditions are used in the finite element simulation for all but the axial degree of freedom to ensure a precise match between the condylar contact location in the knee simulator testing and in the finite element simulation. Sign conventions follow those given in ISO 14243-1 [23], illustrated in Figure 3.7 for the tibial insert and Figure 3.8 for the femoral component. The finite element simulation displacement and axial force data are based on a 19-cycle average taken near the 75,177-cycle endpoint of the knee simulator testing. The precise displacement and rotations in the flexion-extension, anterior-posterior, and internal-external degrees of freedom are measured for each 0.01 second time step of the 19-cycle average during knee simulator testing, allowing displacement and rotation boundary conditions to be applied for the prosthetic knee joint simulation throughout the entire simulated gait cycle. Because displacement of the tibial insert in

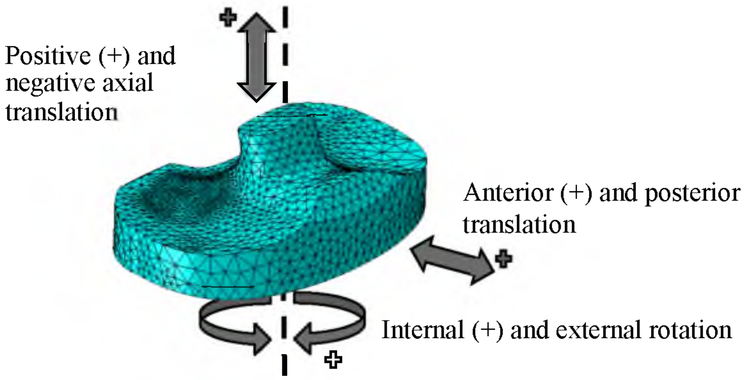

Figure 3.7: Tibial insert (left knee, anterior-medial view) sign conventions for tibial insert motion in the superior-inferior, anterior-posterior, and internal-external directions.

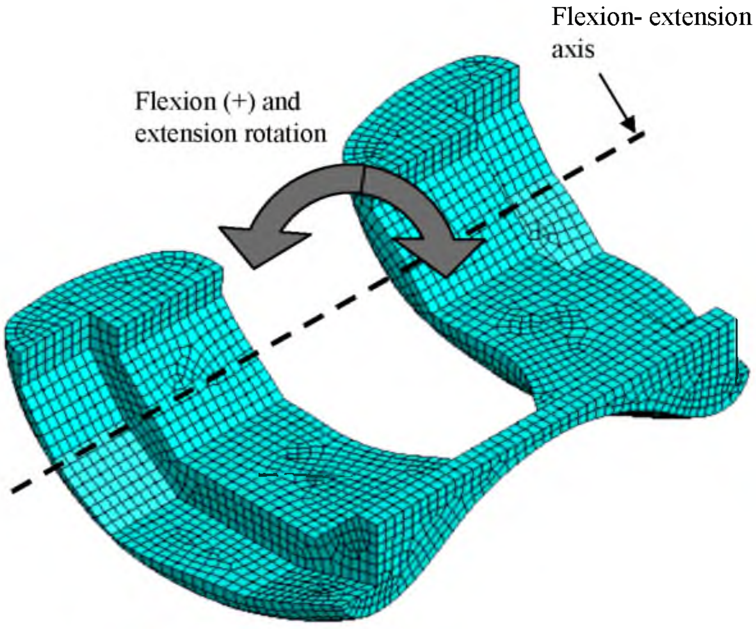

Figure 3.8: Femoral component (left knee, anterior-medial view) sign convention for flexion (+) and extension. An approximation of the flexion-extension axis is indicated by the dashed line.

the axial direction is not measured during knee simulator testing an axial load is applied as the axial degree of freedom boundary condition.

The femoral component is constrained to have zero displacement and rotation in all directions other than flexion-extension rotation, while the tibial insert is constrained to have zero displacement in the medial-lateral direction and zero rotation in the flexion-extension direction. The positive-negative axial displacement of the tibial insert relative to the femoral component and the varus-valgus angle of the tibial insert relative to the femoral component are not specified, allowing the tibial insert to make realistic contact with the femoral component. Figure 3.9 illustrates the applied loading, applied translations and rotations, and unconstrained translation and rotation, for each degree of freedom in the simulated prosthetic knee.

Figure 3.10 shows the applied pressure and displacement versus time during the 0.60-second stance phase of a 1 Hz gait cycle. Figure 3.11 illustrates that for the flexion-extension

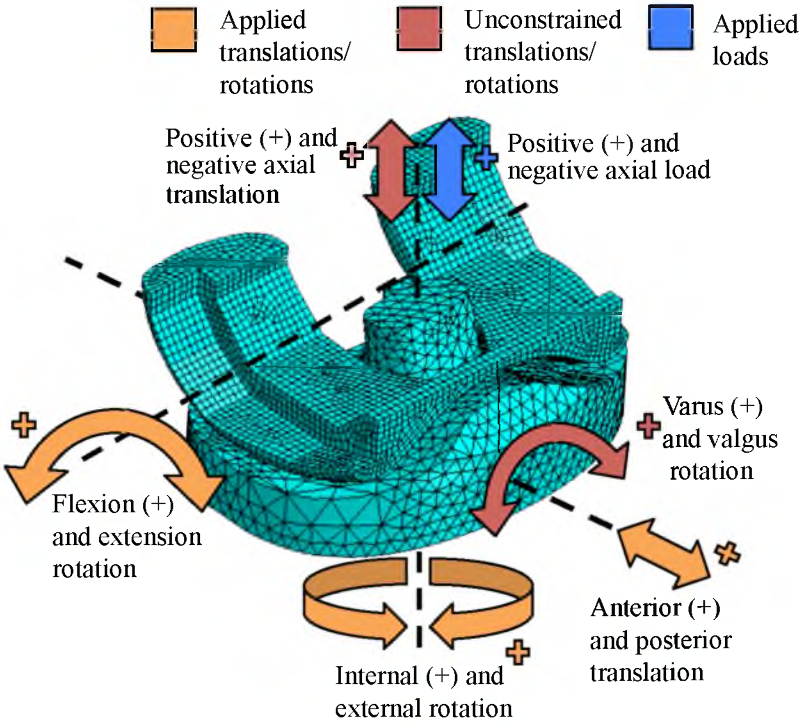

Figure 3.9: Applied loading, applied displacements, and unconstrained displacements for each degree of freedom of the knee simulator. Plus signs indicate the positive direction.

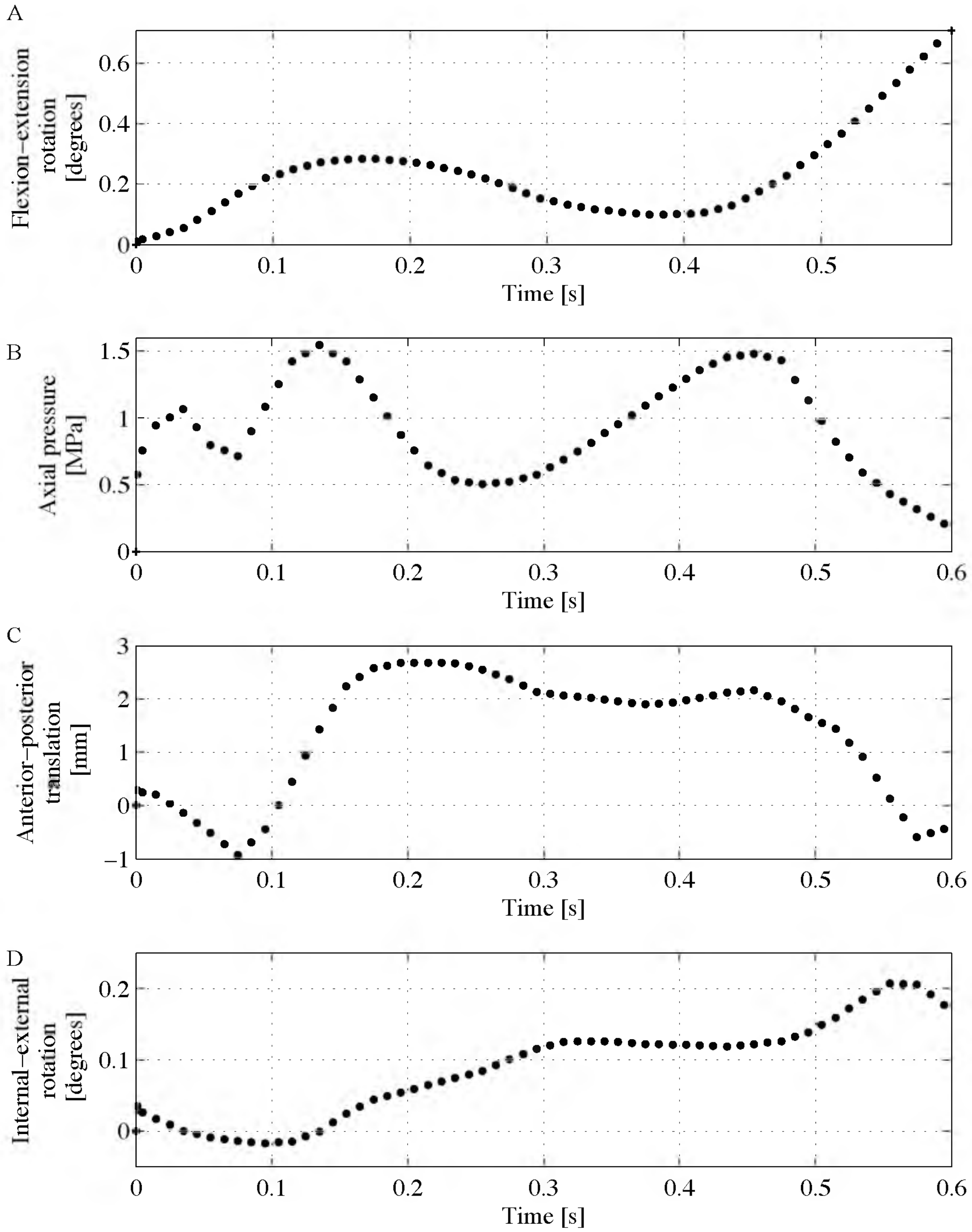

Figure 3.10: Displacements and loading applied to the (left knee) femoral component and tibial insert of the finite element model as a function of simulation time during the 0.60-second stance phase of a 1 Hz gait cycle. (A) Flexion/extension angle applied to femoral component, (B) axial pressure applied to the tibial insert, (C) anterior/posterior translation applied to the tibial insert, and (D) internal/external rotation angle applied to the tibial insert.

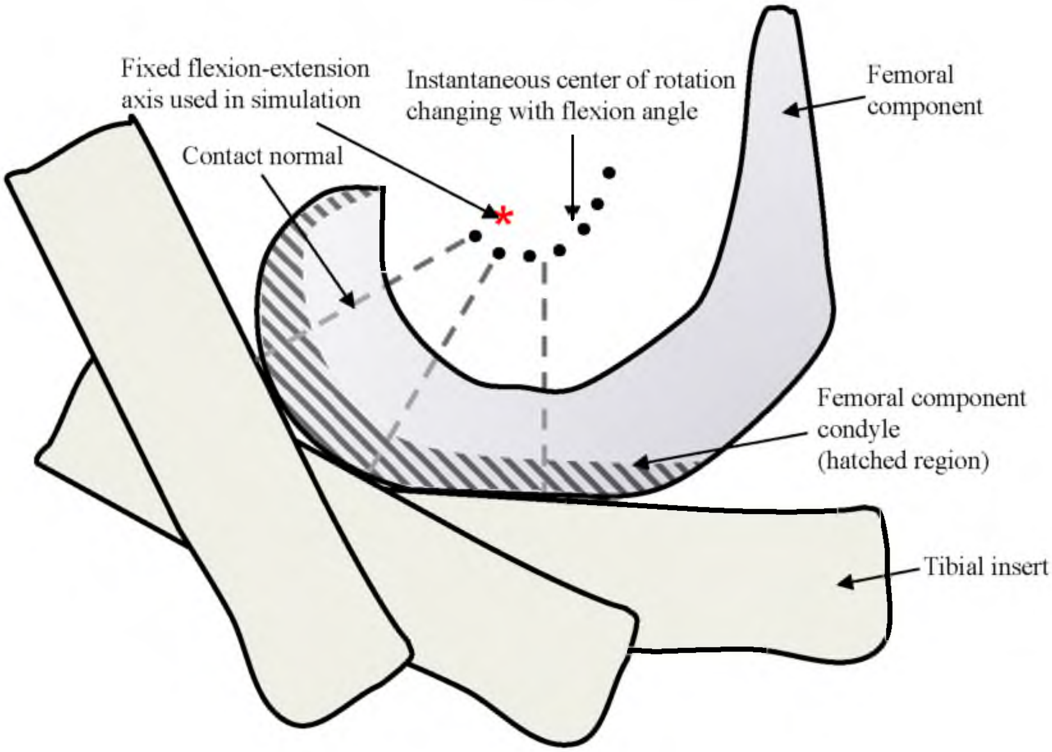

Figure 3.11: Sagittal (side) view of the tibial insert and femoral component during flexion/extension, showing that the instantaneous center of rotation continuously changes as a result of the varying radius of curvature of the condyle of the femoral component. Adapted from [1]. The fixed flexion-extension axis used in the knee simulator testing and in the simulation is also shown.

rotation a continuously moving instantaneous center of rotation exists, because the radius of curvature of the femoral condyles varies along the length of the condyles. The flexion-extension rotation axis used in the knee simulator and in the finite element model is based on a fixed axis approximation of the instantaneous axis of rotation for 30 to 60 degrees of flexion, also shown in Figure 3.11.

The fixed flexion-extension rotation axis of the femoral component is determined in SolidWorks following the guidelines listed in the ISO standard 14243-1, section 3.6 [23]. A CAD model of the femoral component is placed into contact with a horizontal plane. Figure 3.12 illustrates how the longitudinal axis of the femoral component is then angled to 30 degrees (Figure 3.12 A) and 60 degrees (Figure 3.12 B) relative to the normal of the horizontal plane.

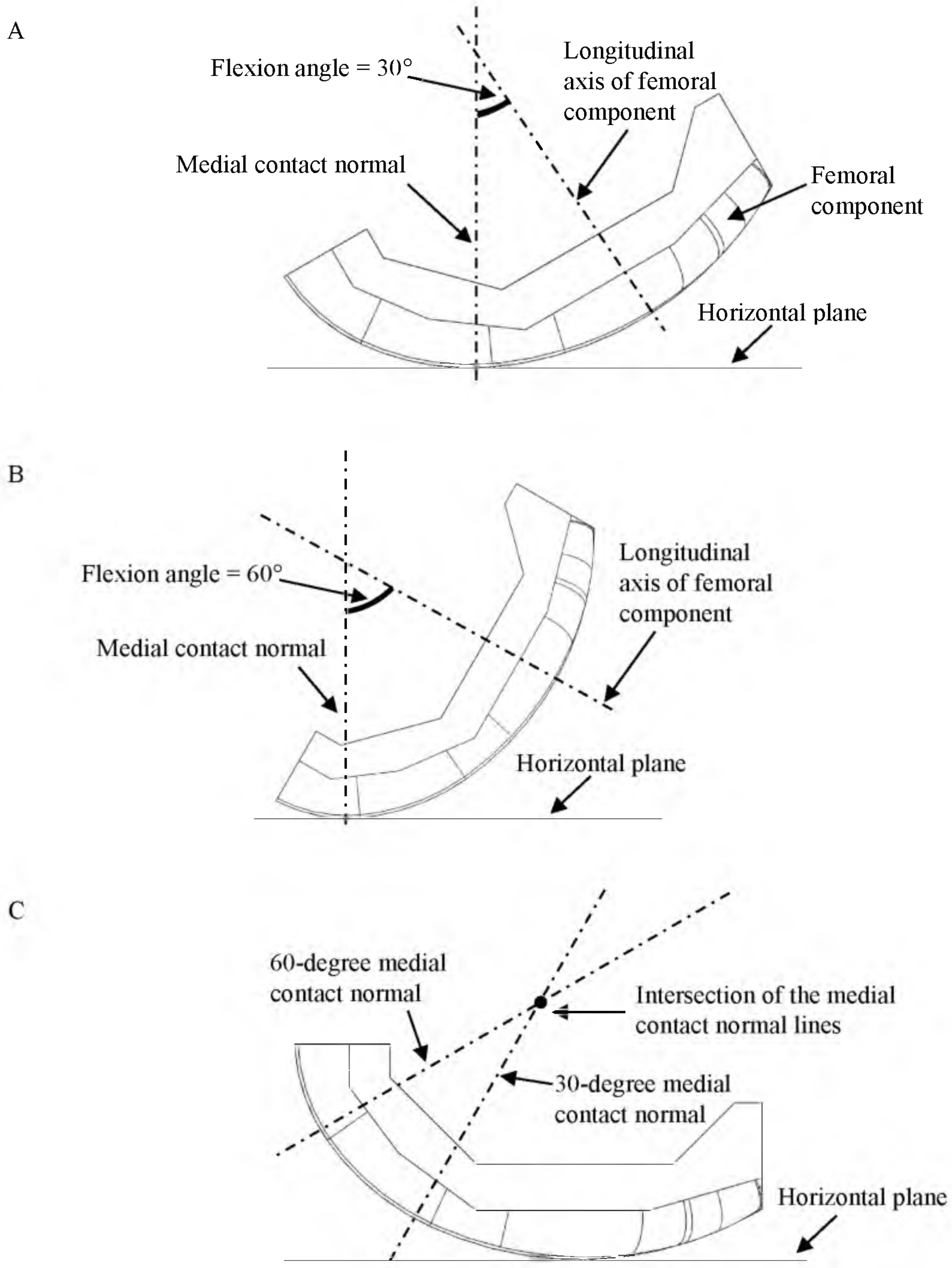

Figure 3.12: Medial view of left knee femoral component and contacting plane for creation of femoral flexion axis based on contact normals at 30 and 60 degrees of femoral flexion. (A) Normal lines are found at 30 degrees and (B) 60 degrees of flexion between longitudinal axis of femoral component and the normal to the horizontal plane. (C) The point of intersection of the 30 degree and 60 degree contact normal lines (marked by black dot) defines the fixed femoral flexion-extension rotation axis.

This mimics femoral flexion to 30 and 60 degrees. For both flexion angles a contact normal, i.e., a line orthogonal to the contact plane and originating in the contact point, is drawn for both the medial and lateral femoral condyle. Figure 3.12 C shows that the two medial contact normal lines intersect. The flexion-extension axis is then determined by connecting the intersection of the medial and lateral contact normals.

Figure 3.13 shows the reference point *RP1*, which is used to create flexion and extension of the femoral component, placed on the fixed femoral component flexion-extension axis. *RP1* is rigidly attached via a kinematic constraint to a second reference point, *RP2*, located on the femoral component. When a flexion-extension angle is specified, *RP1* rotates on its *x*-axis, which is collinear with the femoral component flexion-extension axis, to the specified angle. A kinematic constraint specifying the magnitude and direction of displacement of *RP1* is used to constrain the femoral component to rotate about the flexion-extension axis. Figure 3.14 shows the kinematic constraint applied to the tibial insert reference point. Reference point *RP1*, located on the tibial insert loading axis at the tibial insert's *y*-direction center of rotation, is rigidly attached

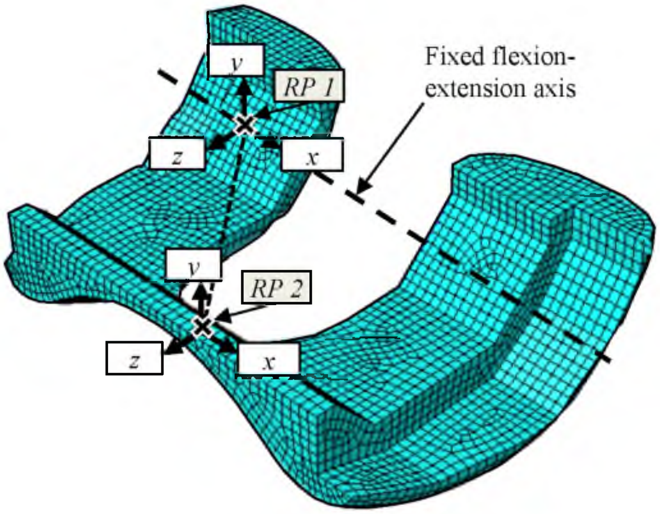

Figure 3.13: Femoral flexion constraint (left knee, anterior-lateral view). Reference point *RP2*, indicated by a black "X," is rigidly attached to the femoral component. *RP2* is also rigidly attached via a kinematic constraint (dashed line) to *RP1*, indicated by a second black "X," which is located at the femoral component fixed flexion-extension axis.

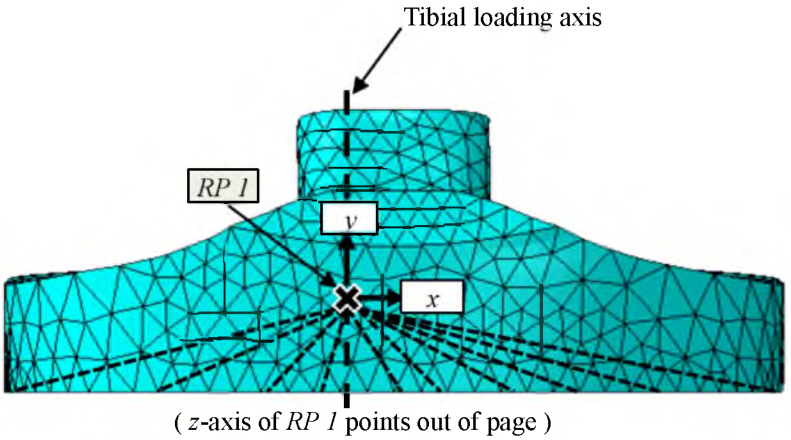

Figure 3.14: Tibial insert displacement and rotation constraint (left knee, anterior view). Reference point *RP 1*, indicated by a black "X," is rigidly attached via a kinematic constraint (set of dashed lines) to the base of the tibial insert.

via a kinematic constraint to the base of the tibial insert. This kinematic constraint controls the internal-external and varus-valgus rotation and anterior-posterior and positive-negative axial translation.

The internal-external rotation axis of the tibial insert corresponds to the axis along which the axial load acts on the tibial insert. Figure 3.15 shows the tibial insert loading axis, which is defined in ISO standard 14243-1 [23] as being parallel to the center axis of the tibial insert and offset medially from the center axis by $0.07w \pm 0.01w$, where w is the width of the tibial insert (Figure 3.15 A). The tibial loading axis is also used to define the anterior-posterior translation of the tibial insert relative to the flexion-extension axis of the femoral component. Figure 3.15 B shows the anterior-posterior position of the axis relative to the tibial insert. The anterior-posterior displacement is measured as the perpendicular distance between the tibial insert loading axis and the femoral component flexion-extension axis, with the anterior and posterior directions being in

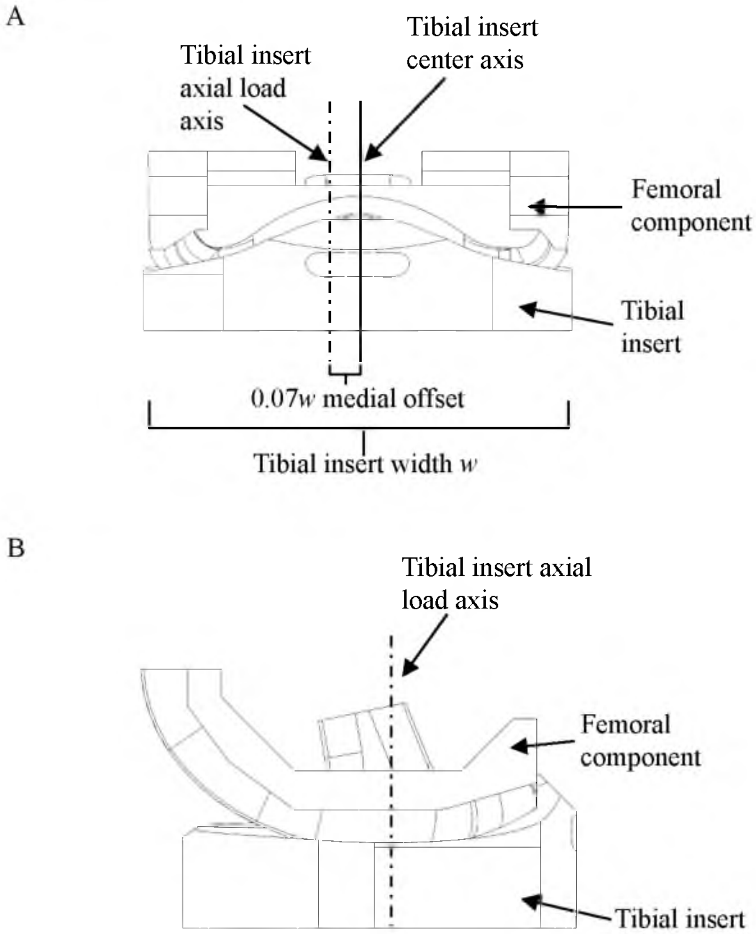

Figure 3.15: Tibial insert loading axis position relative to the tibial insert in a left prosthetic knee joint. (A) Anterior view of the tibial insert loading axis relative to the center axis. (B) Medial view of the femoral component-tibial insert assembly with the tibial insert loading axis visible as dashed line.

reference to the tibial insert's coordinate system and, thus, the direction changes with the rotation of the tibial insert about the tibial force axis. Figure 3.16 shows the neutral reference position for the anterior-posterior translation axes. The femoral component flexion-extension and tibial insert loading axis allow the position of the two components relative to each other at each point in the gait cycle to be fully defined. In all cases the translations and rotations are described relative to the neutral position, described in ISO 14243-1 as the position where the femoral component is fully seated in the tibial insert and both components are in static equilibrium under axial loading [23].

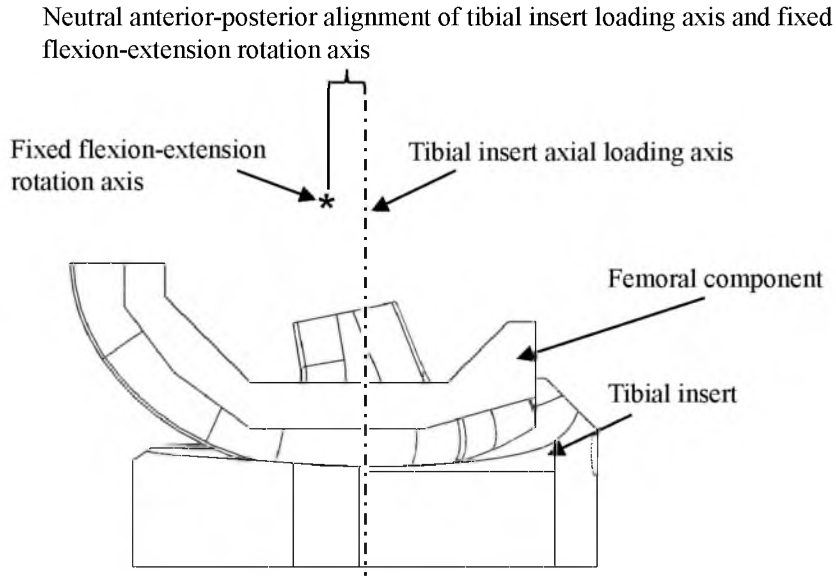

Figure 3.16: Medial view of the reference axes for anterior-posterior translation of the (left) tibial insert in neutral position. The asterisk represents the fixed flexion-extension axis, which is oriented normal to the page. The dashed black line represents the tibial force axis.

This position is achieved within SolidWorks by seating the femoral component with a fixed tibial insert while using simulated contact to prevent component overlap. Contact is specified as "general contact." For the "general contact" type, specific contact surfaces are not specified in Abaqus. Rather, all surfaces on both components are examined for contact at each iteration of the analysis. The tangential behavior is modeled as frictionless contact. This approach has been commonly used in research documented in the literature [17,41,42,52,53], as the coefficient of friction of UHMWPE on Cobalt-chromium is small, with measured values on the order of 0.04 and ranging between 0.01 and 0.07 [3,13,16,34]. Since displacement is controlled by the boundary conditions for anterior-posterior and medial-lateral translation, the influence of friction can be neglected with regard to its effect on tibial insert and femoral component motion under the applied loading. The effect of friction on contact pressure is assumed to be negligible, as the coefficient of friction in prosthetic knee joint contact simulations has been found to have a minimal impact on total contact pressure [16]. "Hard contact" pressure-overclosure enforcement, in which penetration of the contacting parts is minimized and no tension is transferred across the contact interface, is used to control the contact between the tibial insert and femoral component in the normal contact direction.

3.2.4 Convergence

An explicit solver is selected to economically solve the dynamic finite element model. To evaluate model convergence, the initial mesh is selectively refined throughout the contact region between the tibial insert and femoral component, until the maximum von Mises stress does not change by more than 3% between subsequent mesh refinements. Figure 3.17 shows the initial mesh, which uses an average element length of 5.0 mm for the tibial insert and 1.0 mm for the femoral component. The tibial insert mesh is locally refined for each convergence analysis, while the rigid-body femoral component mesh is preserved at the same refinement. The tibial insert mesh refinement uses both surface and cell mesh partitioning to preserve good mesh quality based on element aspect ratios and face angles. The number of poorly-shaped elements in the region of interest is minimized for each refinement. Figure 3.18 shows the final mesh that delivered converged stress results. Each refined mesh is applied to an abridged convergence study simulation to reduce computational time. This abridged simulation solves a section of the gait cycle during which maximum stress is expected based on an initial full-length stance phase trial with the course mesh. The convergence study uses the linear elastic UHMWPE material model.

We obtain a converged solution for a refined mesh with element lengths of 0.625 mm in the region of interest (highest strain and stress) and 2 mm globally throughout the tibial insert. The maximum von Mises contact stress observed at this mesh refinement is 79.61 MPa and changes by only 2.9%, to a maximum contact stress value of 77.34 MPa, for a doubled mesh density in the region of interest. The converged solution for the abbreviated refinement simulation is validated via comparison to the maximum contact stress magnitude as calculated using a Hertzian contact model.

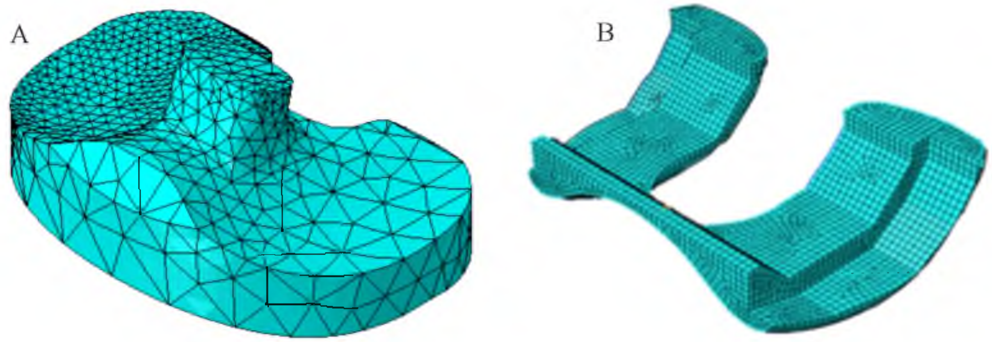

Figure 3.17: Initial model mesh for (left knee) tibial insert and femoral component. (A) The mesh of the tibial insert, which is refined in subsequent analysis. (B) The mesh of the femoral component mesh, which is maintained constant throughout the study.

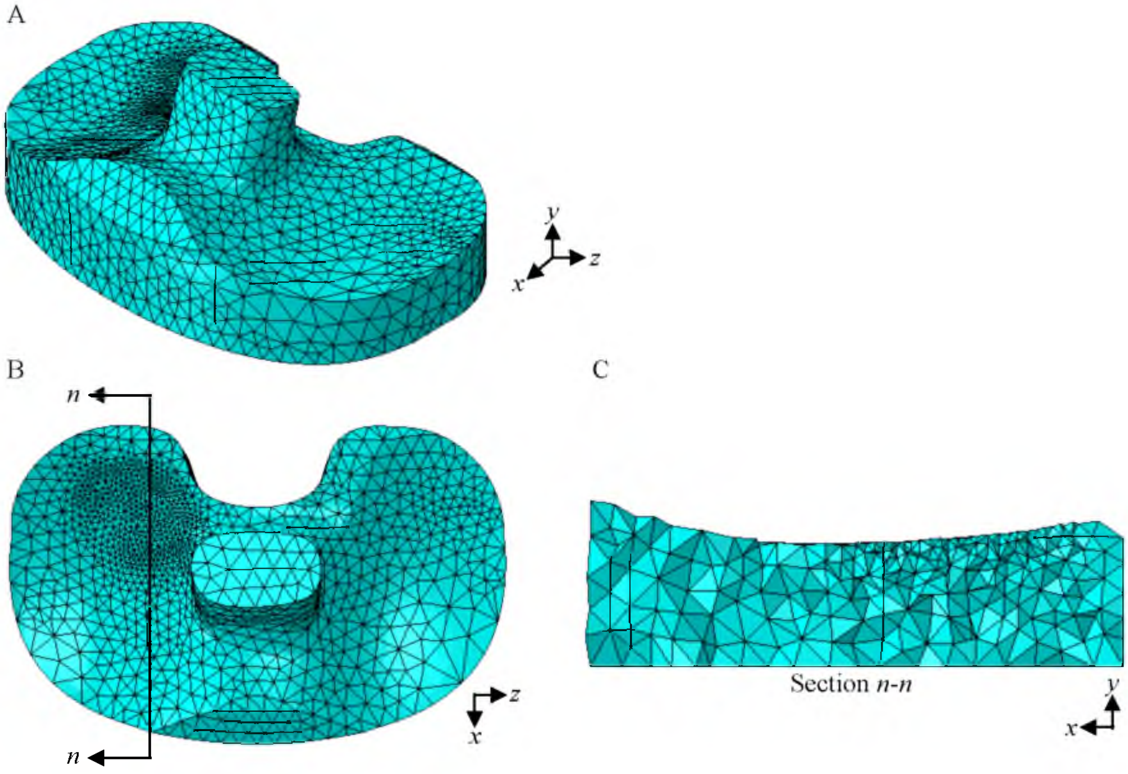

Figure 3.18: Final refined mesh for the tibial insert. (A) Anterior view and (B) top view showing location of refinement. (C) Cut-away view of refinement through depth along the line marked in (B), lateral view of cut.

3.2.4.1 Hertz Contact Verification

The Hertz contact theory is applicable to elastic contact of two curved surfaces loaded against each other along their contact normal. The following conditions must hold true: 1) The surfaces in contact are continuous and nonconforming, i.e., the bodies contact only at a single point or line prior to deformation and, once loaded, the radius of the contact area remains much smaller than the dimensions of the contacting bodies, 2) the strains are small and remain within the linear deformation threshold of the contacting materials, 3) each contacting body can be considered an elastic half-space loaded over a small elliptical contact area, and 4) the surfaces of the contacting bodies are frictionless, thus transmitting only a normal component of contact pressure [54]. Although the contact between the femoral component condyles and tibial insert condyles cannot be classified as a true Hertz contact, this model provides a reasonable approximation of the contact situation occurring within the prosthetic knee joint.

The parameters used in the Hertzian contact model approximate those of the prosthetic knee joint when maximum stress occurs. The contact between the tibial insert and femoral component is approximated as 1) a single condyle-condyle contact with the entire load through the prosthetic knee joint applied to the single condylar contact, and 2) a symmetric double condyle-condyle contact with half the total load applied to the single condyle-condyle contact.

The first and second principal radii of curvature for the femoral ellipsoid are based on the sagittal and frontal radii of curvature of the femoral component. Two possible radii exist in the sagittal plane. The large radius associated with the anterior portion of the femoral component is selected because this section of the femoral component is in contact at the 16 degrees of flexion when maximum stress occurs in the gait cycle simulation. Thus, the radius of curvature of the first principal axis is 27.6 mm while that of the second principal axis is 21.0 mm. The corresponding tibial insert condyle is approximated as an ellipsoid with radii along the first and second principal axes of negative 71.9 mm and 32.5 mm, respectively. The material properties used for the femoral and tibial ellipsoids are given in Table 3.1.

Equation (3.19) is used to calculate the maximum pressure p_0 between the femoral ellipsoid and tibial ellipsoid under normal load F.

$$p_0 = \frac{3F}{2ab\pi} \tag{3.19}$$

where a and b are calculated as

$$a = f \cdot \left(\frac{3F}{gX} \cdot (\theta_1 + \theta_2) \right)^{1/3} \tag{3.20}$$

$$b = g \cdot \left(\frac{3F}{gX} \cdot (\theta_1 + \theta_2) \right)^{1/3} \tag{3.21}$$

The values for θ_1 and θ_2 are calculated as

$$\theta_1 = 4 \cdot \left(\frac{1 - \nu_1^2}{E_1} \right) \tag{3.22}$$

$$\theta_2 = 4 \cdot \left(\frac{1 - \nu_2^2}{E_2} \right) \tag{3.23}$$

where E_1, ν_1 and E_2, ν_2 are the material properties of the femoral component and tibial insert, respectively. Coefficients f and g are selected from a table of coefficients based on the value of Ω [55].

$$\Omega = \cos^{-1} \left(\frac{\sqrt{X_1^2 + X_2^2 + 2X_1X_2 \cos\left(2\alpha \frac{\pi}{180}\right)}}{X} \right) \tag{3.24}$$

where α is the angle, in degrees, between the major radii of the two ellipsoids. X, X_1, and X_2 used in Equation (3.20), (3.21), and (3.24) are calculated as

$$X = \frac{1}{r_{11}} + \frac{1}{r_{12}} + \frac{1}{r_{21}} + \frac{1}{r_{22}} \tag{3.25}$$

$$X_1 = \frac{1}{r_{11}} - \frac{1}{r_{12}} \tag{3.26}$$

$$X_2 = \frac{1}{r_{21}} - \frac{1}{r_{22}} \tag{3.27}$$

where r_{11}, r_{12}, r_{21}, and r_{22} are the major and minor radii for the femoral and tibial ellipsoids.

A force of 1911.91 N, equal to the applied axial load on the tibial insert when the maximum tibial insert subsurface stress of 79.61 MPa occurs during the convergence simulation, is used as the normal force on the tibial ellipsoid. For the single condyle-condyle approximation the entire load is applied, while half of the load is applied for the double condyle-condyle contact approximation. The Hertz contact stress is compared to the maximum stress during each mesh refinement of the convergence study. Figure 3.19 shows the converged solution of local von Mises stress magnitude within the medial condyle of the tibial insert at the point in the abbreviated simulation when the maximum von Mises stress of 79.61 MPa is reached.

Table 3.3 lists the results for both contact scenarios and for two finite element simulations. Finite element simulation 1 is the abbreviated refinement simulation. Finite element simulation 2 is identical to the first except for a modification to the boundary conditions

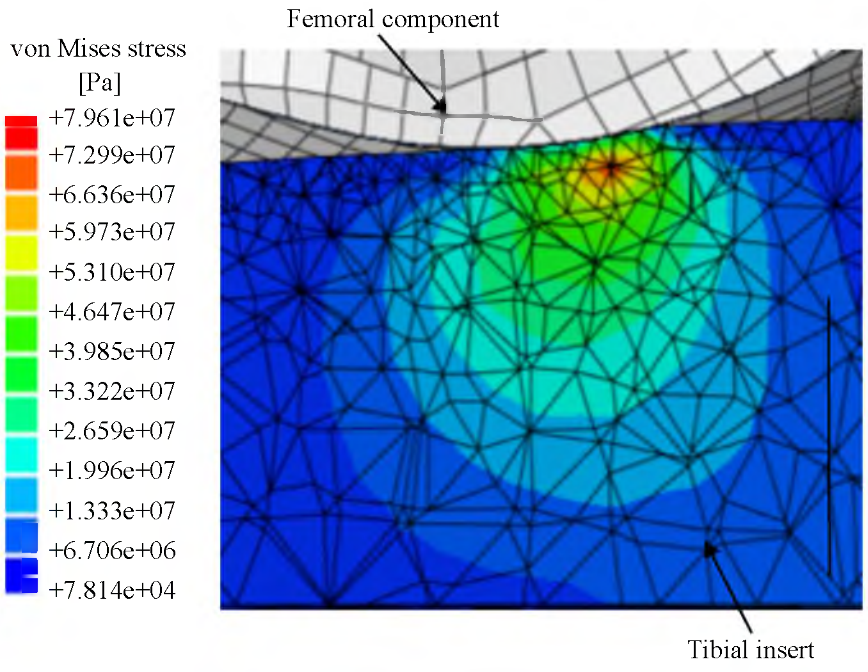

Figure 3.19: Local von Mises stress when maximum stress occurs during the abbreviated convergence trial, finite element simulation 1. View shows lateral view of anterior-posterior cross-section of medial condyle of tibial insert.

Table 3.3: Hertz stress results for the two extremes of possible loading conditions in comparison to maximum von Mises stress during finite element simulation.

Contact condition	Hertz contact stress [MPa]	Maximum von Mises stress from finite element simulation 1 [MPa]	Maximum von Mises stress from finite element simulation 1 [MPa]
Single condyle-condyle contact	53.59	79.61	76.46
Double condyle-condyle contact	42.54		

in which the anterior-posterior and internal-external displacements are set to zero and only the axial force contributes to the contact stress. Comparison between the contact stress results from finite element simulations 1 and 2, demonstrates the contribution of the anterior-posterior and internal-external displacements to the magnitude of the contact stress.

The maximum von Mises stress is on the same order of magnitude as both Hertz predictions for maximum contact stress, with the finite element simulation result being higher by approximately 23 and 26 MPa for the single condyle-condyle contact condition and approximately 34 and 37 MPa for the double condyle-condyle contact condition, for finite element simulations 1 and 2, respectively. In the finite element simulations, the condyles are not precisely elliptical. Consequently, the femoral condyle to tibial insert condyle contact region is not perfectly approximated by an elliptical contact region. In the finite element simulations, contact between the femoral condyle and tibial condyle occurs on the more vertically sloped region at the base of the tibial insert stabilizing post and outer condyle edges rather than exclusively within the region centered on the apex of the concave condylar surface, resulting in two separate contact regions per condyle and contact radii different than those predicted by the Hertz contact model. This difference in contact geometry between the finite element simulation and the Hertz model may account for the difference in calculated maximum contact stress magnitude between the finite element simulation and Hertz solution.

The von Mises stress magnitude plot in Figure 3.19 illustrates that the location of the maximum von Mises stress exists a short distance below the surface, as predicted by the Hertz solution. The combination of mesh refinement and comparison with an analytical solution provide confidence that the numerical simulation provides a converged solution.

3.3 Simulation Results

Figure 3.20 shows a plot of the maximum von Mises stress for each output frame of the full-length stance phase linear elastic UHMWPE material model simulation as a function of time. Figure 3.21 shows a plot of the corresponding von Mises maximum stress values for the linear viscoelastic UHMWPE material model simulation. Each plot contains the maximum von Mises stress that occurs in the tibial insert, the maximum subsurface von Mises stress in the medial condyle of the tibial insert, and the maximum von Mises stress in the lateral condyle of the tibial insert, for each output frame (i.e., the twenty 0.0305-second intervals that make up the 0.61 second simulation). The precise values for the linear elastic and linear viscoelastic simulations are listed in Appendix D.

During multiple simulation output frames the maximum von Mises stress throughout the insert is a result of artificial surface stress maxima. First, the depth at which each maximum stress occurs is compared to the expected depth as predicted by the Hertz contact approximation of the condyle-condyle contact, and by other works in the literature. Similar finite element simulation studies of prosthetic knee joint contact during gait documented maximum shear and von Mises stress occurring at a 1-2 mm depth below the surface of the tibial insert [43,56]. Hertz theory supports these findings, predicting a maximum contact stress at $0.48a$, where a is the radius of the contact area of Hertzian contact.

For the femoral-tibial condyle contact approximation, $a = 4.56$ mm, corresponding to a maximum von Mises stress location depth of 2.19 mm. Hence, we categorize high stress values at

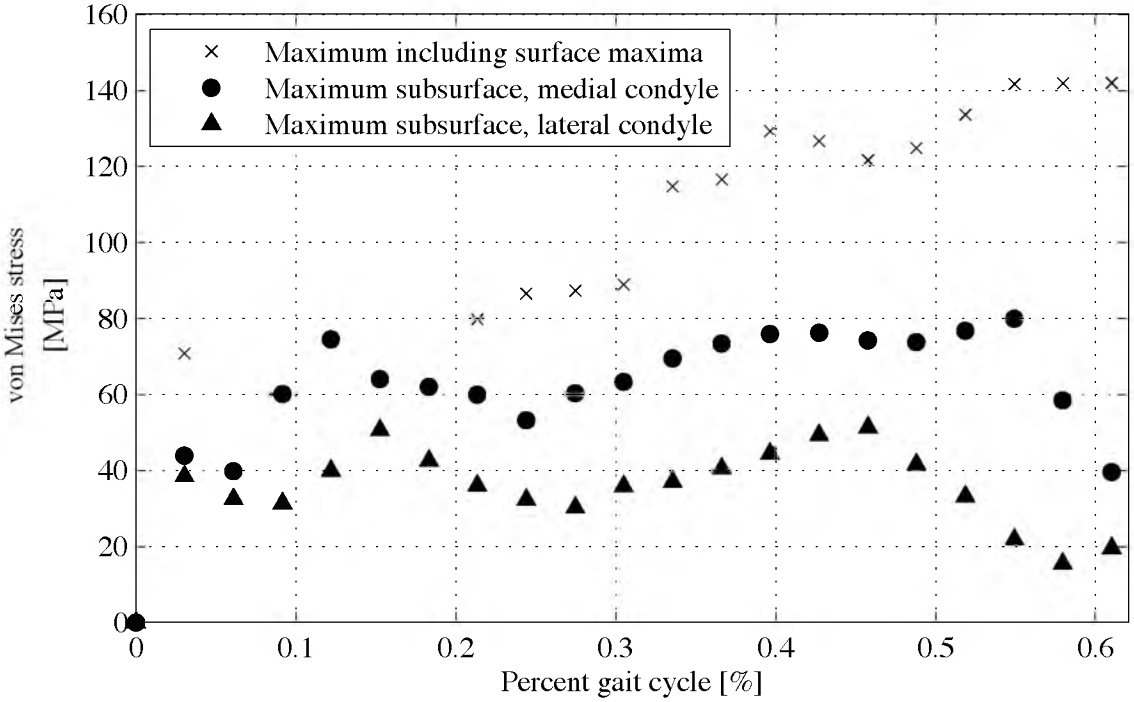

Figure 3.20: Maximum von Mises stress in the tibial insert as a function of time during the finite element stance phase simulation. UHMWPE is modeled using a linear elastic material model.

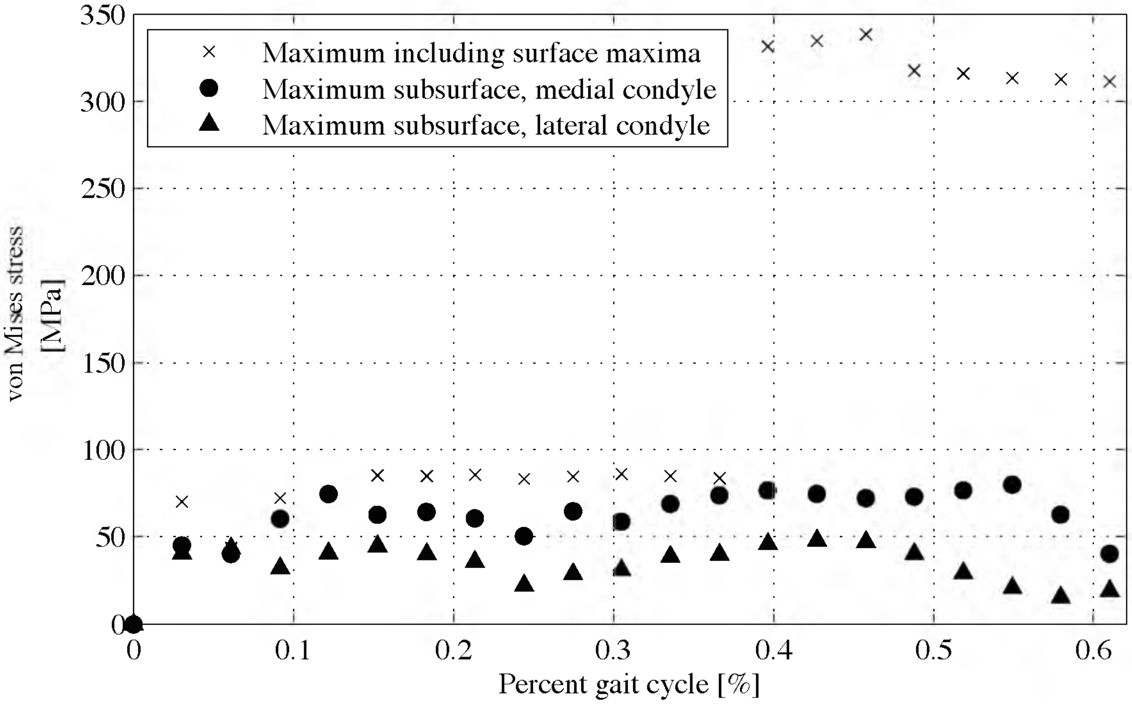

Figure 3.21: Maximum von Mises stress in the tibial insert as a function of time during the finite element stance phase simulation. UHMWPE is modeled using a linear viscoelastic material model.

and immediately below the surface (< 0.5 mm depth) as numerical artifacts. Figure 3.22 shows subsurface and surface von Mises stress magnitudes within the tibial insert to illustrate this effect. The von Mises stress maxima observed on the surface of the tibial insert, magnified in Figure 3.22 insets A and B, are extremely localized relative to the larger regions over which other stress magnitudes occur, and are highly discontinuous with surrounding stress magnitudes. The depth of the artificial maximum stress, based on the scale shown in Figure 3.22 inset B, confirms that the stress artifact is near the surface, at a depth that is unrealistic according to the Hertz contact approximation and results described in the literature.

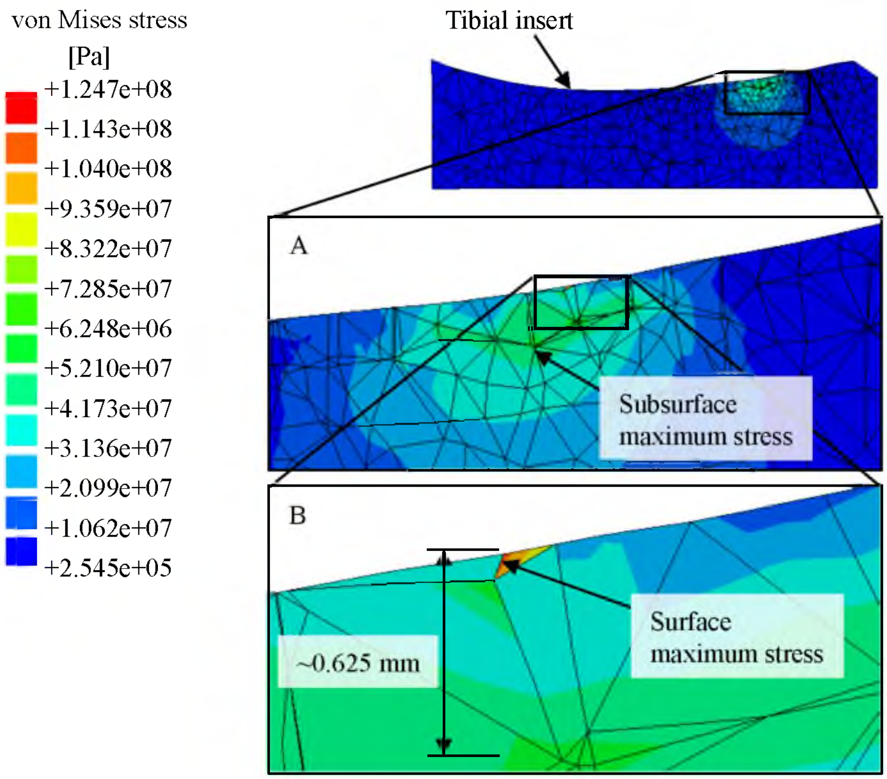

Figure 3.22: Subsurface and surface von Mises stress maxima within the tibial insert. Inset A shows a subsurface stress maximum, where the actual maximum contact stress occurs. Inset B shows an artificial stress maximum at the surface of tibial insert.

Figure 3.23 shows examples of the maximum subsurface von Mises stress from the beginning (0.1525 s), middle (0.4575 s), and end (0.6100 s) of the stance phase simulation (subfigures A, B, and C, respectively). In each case the subsurface maximum von Mises stress is located in the posterior portion of the medial tibial insert condyle. The stress contours for these subsurface localized stress magnitudes are continuous and the depth of the maximum stress is approximately constant, indicating that the condyle-condyle contact area is similar during each segment of the stance phase simulation.

The maximum subsurface von Mises stress within the tibial insert medial condyle and the maximum subsurface von Mises stress within the tibial insert lateral condyle is recorded for each output frame (0.0305 s increments) for stance-phase simulations using the linear elastic and the linear viscoelastic UHMWPE material model. Figure 3.24 plots the maximum subsurface von Mises stress magnitude at each output frame of the stance phase simulation for the medial (Figure 3.24 A) and lateral (Figure 3.24 B) tibial insert condyles. The results demonstrate that the medial condyle contact stress is consistently higher than the lateral condyle contact stress for both the linear elastic and linear viscoelastic material models. In addition, the maximum stress magnitude within each condyle consistently exceeds the yield stress of the material of 21 MPa [57], marked by the shaded region in each plot. This indicates that consideration of the plastic response of the UHMWPE is important under the knee simulator loading conditions modeled here.

3.3.1 Comparison of Linear Elastic and Linear Viscoelastic Model von Mises Stress Results

Figures 3.25 and 3.26 show the von Mises stress at 0.061 and 0.366 s from the linear elastic and linear viscoelastic simulations. These stress plots illustrate instances during the gait cycle simulation in which the maximum von Mises stress magnitude and location for the linear elastic and linear viscoelastic materials models are visibly different (Figure 3.25) and approximately equal (Figure 3.26). Figure 3.26 is representative of the majority of the simulation,

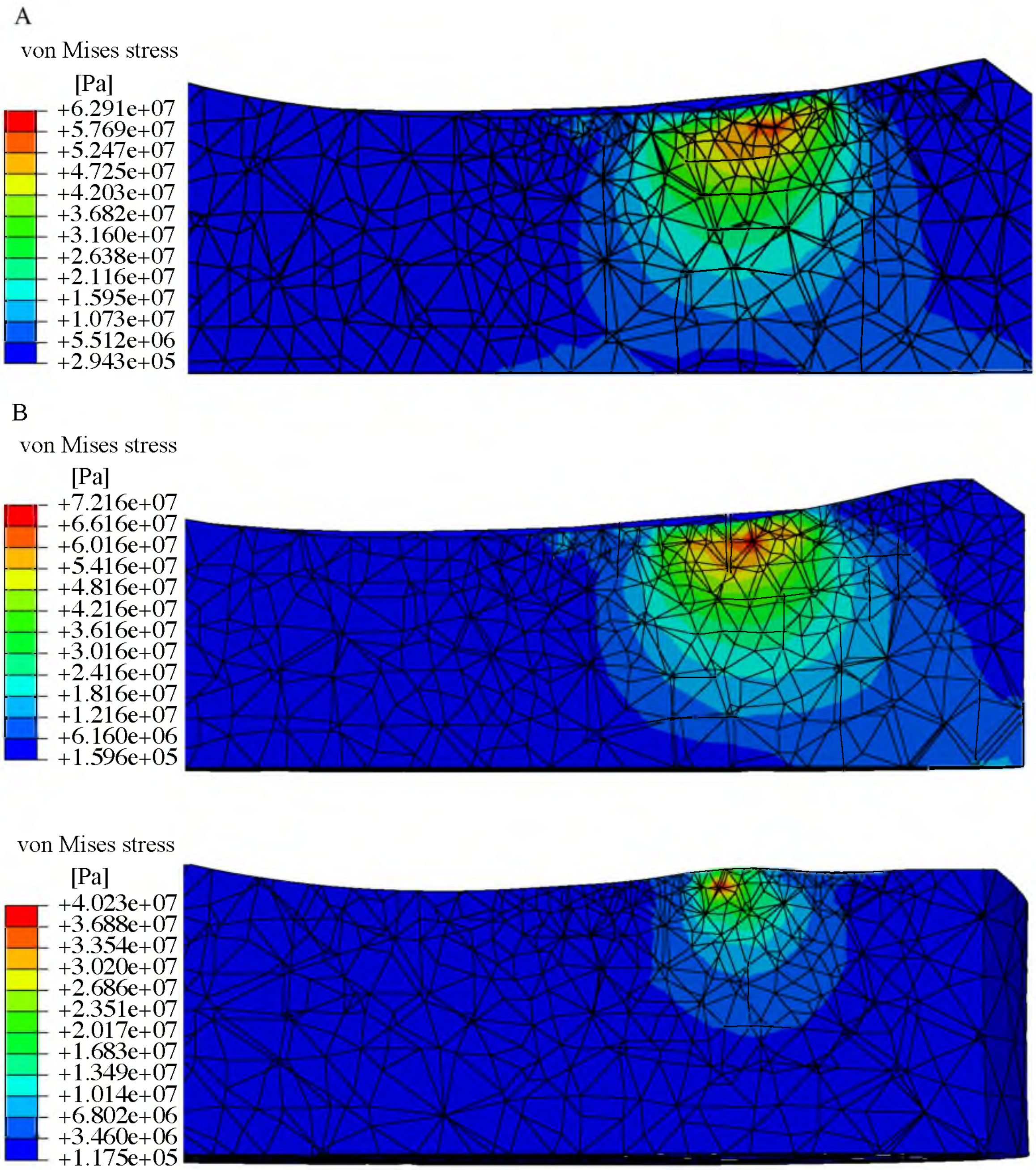

Figure 3.23: Cross-sectional view showing subsurface von Mises stress in the posterior portion of the medial condyle of the modeled tibial insert from the A) beginning (0.1525 s), B) middle (0.4575 s), and C) end (0.6100 s) of the stance phase contact simulation.

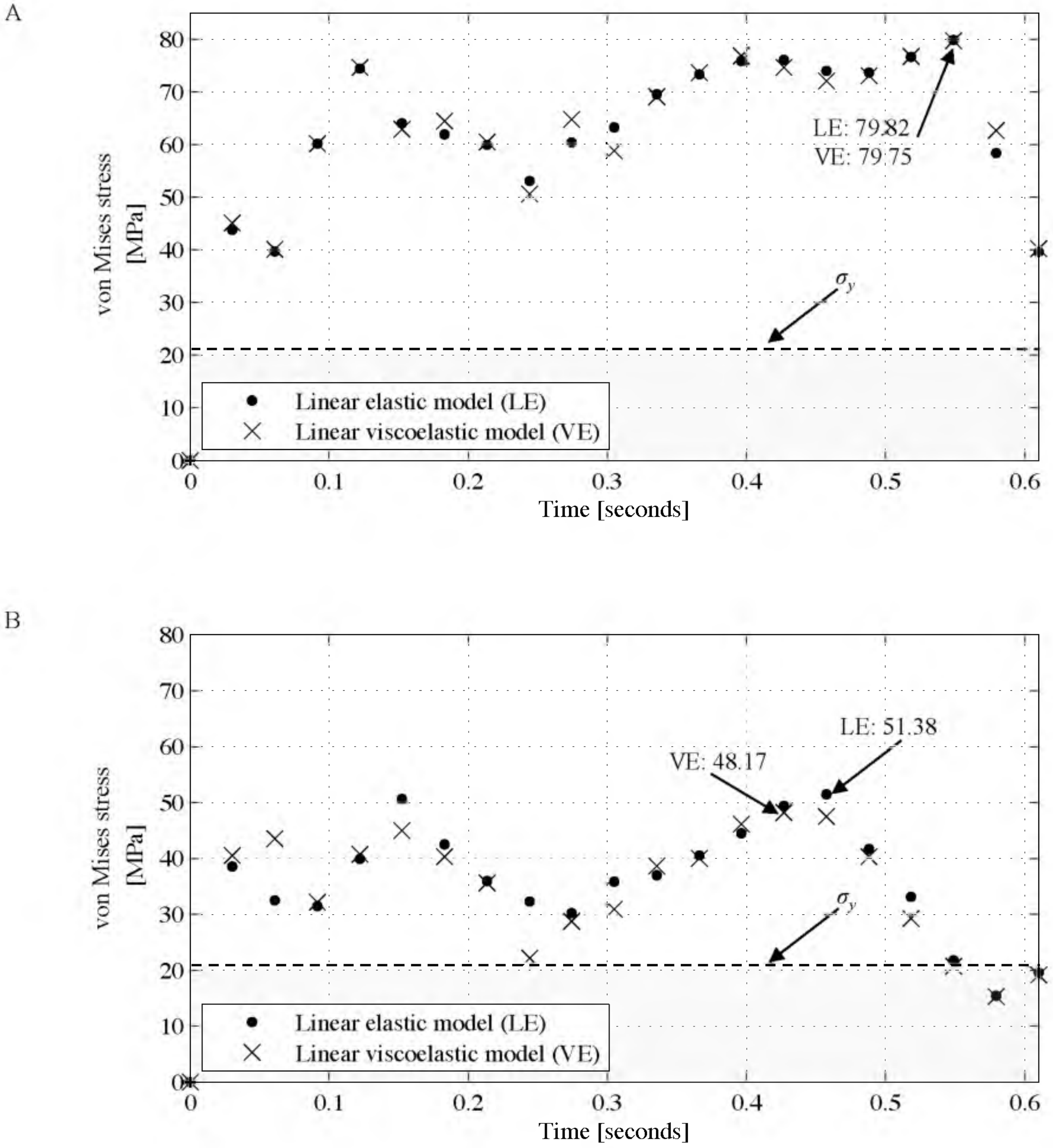

Figure 3.24: Maximum von Mises contact stress as a function of time for linear elastic and linear viscoelastic UHMWPE material models for (A) medial condyle (B) lateral condyle. Overall maximum von Mises stress magnitude for each material model is labeled. The yield stress (σ_y = 21 MPa) is indicated.

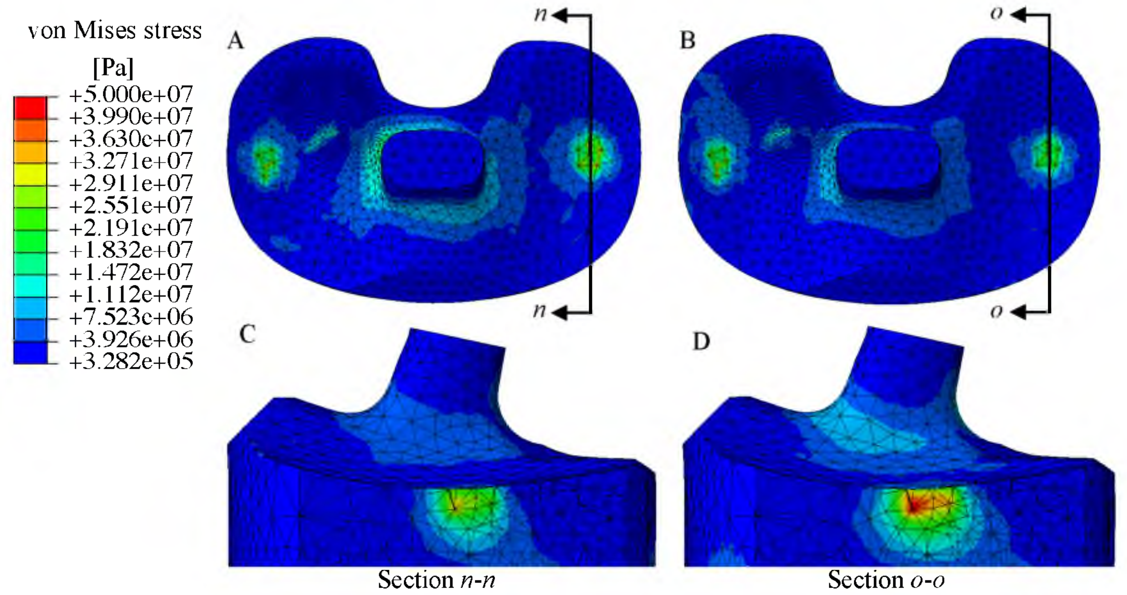

Figure 3.25: Tibial insert von Mises stress at 0.061 seconds of the stance phase simulation. (A) Top view for the linear elastic model. (B) Top view for the linear viscoelastic model. (C) Cut-away view of the subsurface von Mises stress for the linear elastic model. (D) Cut-away view for the linear viscoelastic model.

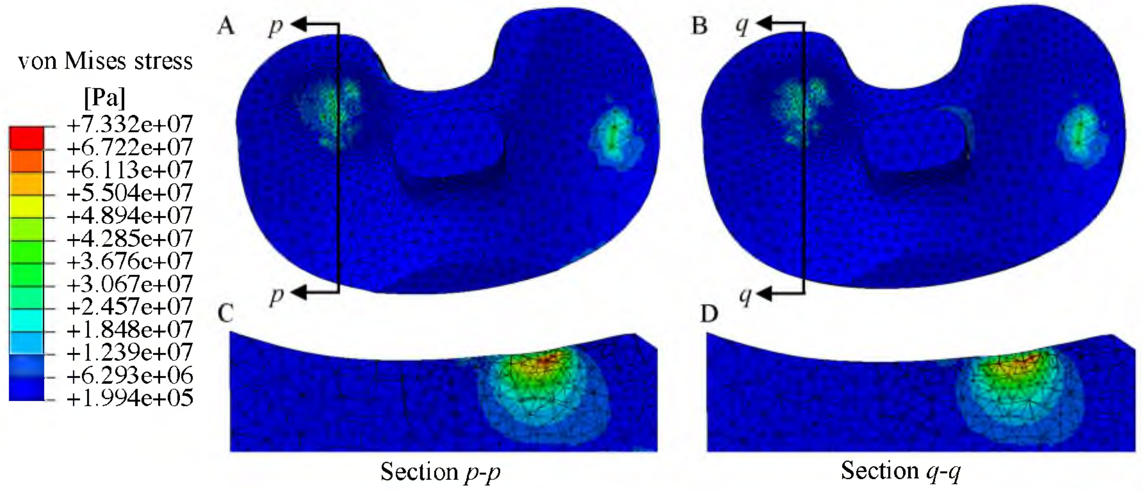

Figure 3.26: Tibial insert von Mises stress results at 0.366 seconds of the stance phase simulation, at which point maximum stress between the linear elastic and viscoelastic material models were approximately equal. (A) Top view of the linear elastic model. (B) Top view of linear viscoelastic model. (C) Cut-away view of the subsurface von Mises stress for the linear elastic model. (D) Cut-away view for the linear viscoelastic model.

as similar stress is observed for both material models throughout the gait cycle, as already shown in Figure 3.24. The difference between the maximum subsurface von Mises stress magnitude between both material models is listed in Table 3.4. The average difference in subsurface maximum von Mises stress is less than 1.00 MPa for both condyles, while the root mean square difference reaches a maximum value of 4.09 MPa, nearly 8% of the lateral condyle overall maximum von Mises stress magnitude.

Figure 3.27 shows the trajectory of the maximum von Mises stress in the medial condyle during the stance phase simulation for the linear elastic (Figure 3.27 A) and linear viscoelastic (Figure 3.27 B) UHMWPE models. The precise locations of the subsurface maximum von Mises stress are marked for each output frame, with the dashed line path connecting the maxima in order of occurrence. We observe that for both material models the maximum von Mises stress is concentrated in the posterior-medial region of the tibial insert for the majority of the simulated stance phase. Figure 3.28 illustrates the subsurface areas over which the von Mises stress exceeds

Table 3.4: Differences in maximum von Mises stress for simulations using the linear elastic and linear viscoelastic material models. * Normalized to overall (both condyles) maximum, **normalized to condyle maximum.

	Medial condyle	Lateral condyle
Maximum difference in maximum von Mises stress between linear elastic and linear viscoelastic material models [MPa]	4.38	10.12
Average difference in maximum von Mises stress over 0.61 s stance phase simulation between the two material models [MPa]	-0.17	0.96
Root mean square (RMS) difference in maximum von Mises stress over 0.61 s stance phase simulation between the two material models [MPa]	2.01	4.09
RMS difference as percentage of overall maximum subsurface von Mises stress [%]	2.52 %* 2.52 %**	5.12 %* 7.96 % **

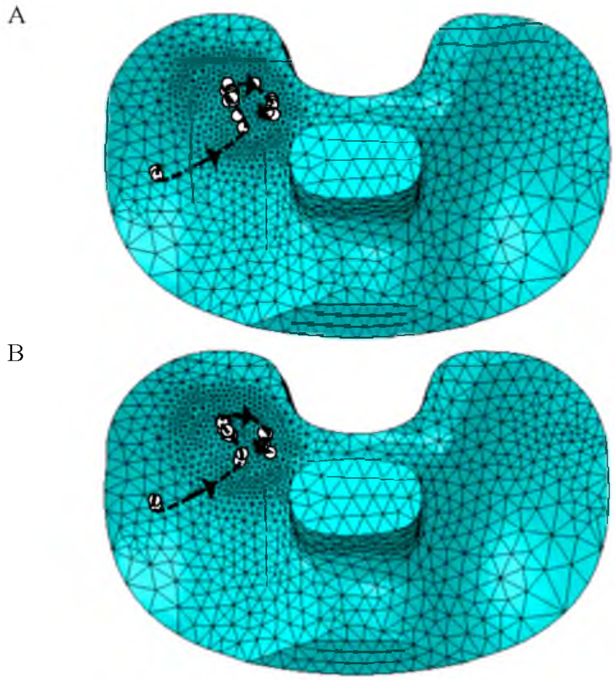

Figure 3.27: Top view of the maximum von Mises stress locations (white dots) in the medial condyle of the (left) tibial insert during the stance phase. The black dashed line indicates the sequence in which the discrete frame stress maxima occur. (A) Maximum von Mises stress locations for the linear elastic model. (B) Maximum von Mises stress locations for the linear viscoelastic model.

the yield stress of the material, which is one predictor of UHMWPE damage.

The stress used for the yield threshold is 21 MPa, based on data from nonirradiated GUR 1050 at 37°C [57]. Figure 3.28 A shows the yield stress exceeding areas for the linear elastic model, while Figure 3.28 B shows the analogous results for the linear viscoelastic model. Figure 3.28 C illustrates the similarity in the size and location of the yield stress exceeding areas between the simulations using the linear elastic and linear viscoelastic UHMWPE material models by outlining the overlapping areas where the yield stress is exceeded for both material models. The overlapping areas represent 81% of the total area over which the yield stress is exceeded for the superimposed material model plots. Regions in Figure 3.28 C where no overlap occurs demonstrate that differences exist in the location and size of the yield stress exceeding area between the linear elastic model and linear viscoelastic model simulations. This demonstrates that there is some effect on stress prediction due to the material model, as expected.

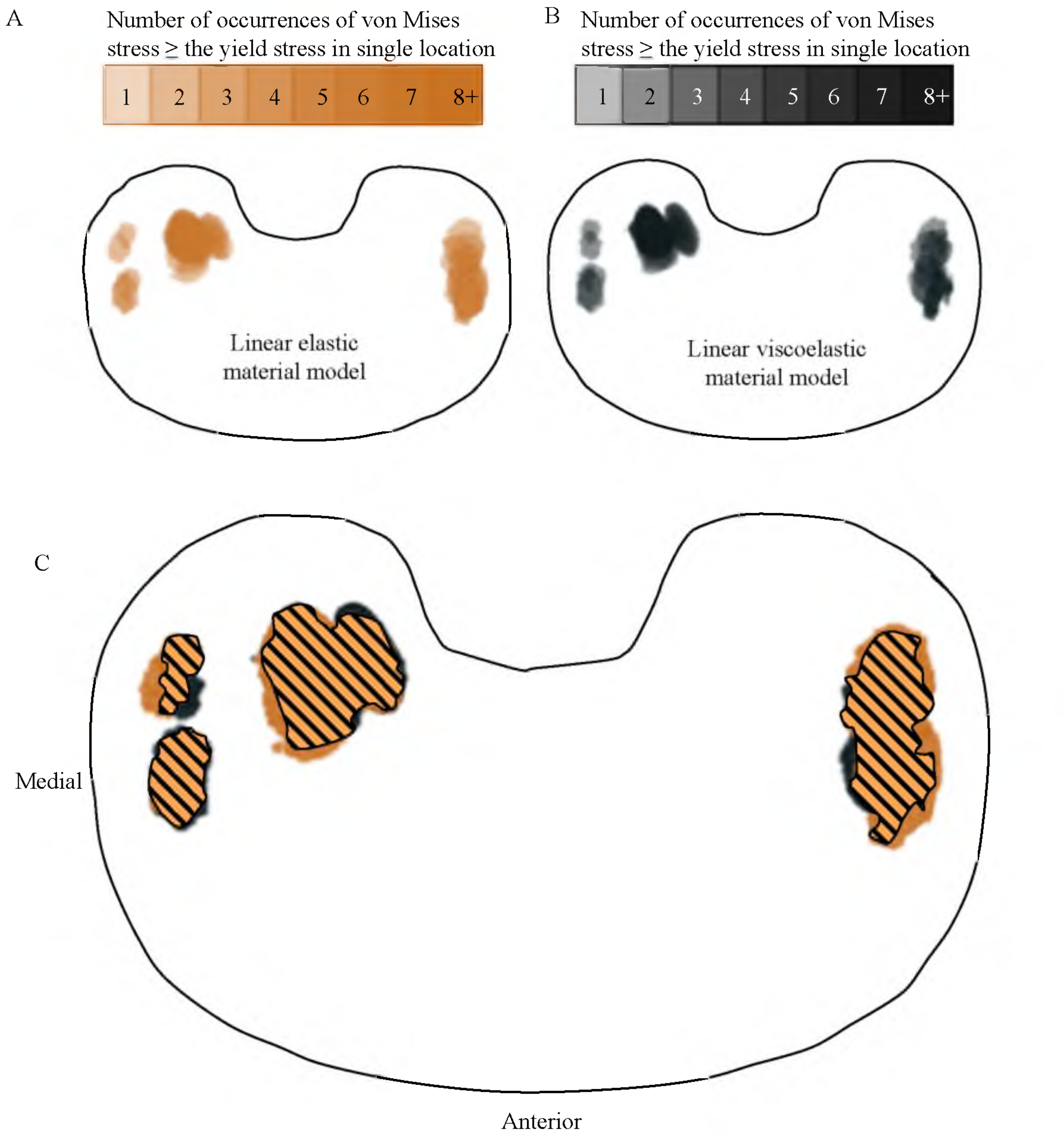

Figure 3.28: Top view of left tibial insert modeled with a linear elastic and linear viscoelastic material model with von Mises stress magnitudes in excess of the yield stress (≥ 21 MPa [57]) marked in shaded regions. (A) The von Mises stress results from the linear elastic model. (B) The von Mises stress results of the linear viscoelastic material model. Partially transparent shaded regions are created for each output frame and then superimposed such that darker areas (more opaque) indicate multiple output frames where that region is stressed in excess of the yield stress, while lighter (more transparent) regions indicate fewer frames at which that region is stressed in excess of the yield stress. (C) The areas at which the yield stress is exceeded for the linear elastic (light orange) and linear viscoelastic (black) material model simulations superimposed for comparison. The hatched regions represent regions in which the linear elastic and viscoelastic model results overlap.

3.4 References

[1] Kurtz, S. M., ed., 2009, UHMWPE Biomaterial Handbook: Ultra High Molecular Weight Polyethylene in Total Joint Replacement and Medical Devices, Elsevier Academic Press, New York, NY.

[2] D'Lima, D. D., Steklov, N., Fregly, B. J., Banks, S. A., and Colwell Jr., C. W., 2008, "In vivo contact stresses during activities of daily living after knee arthroplasty," J. Orthop. Res., **26**, pp. 1549–1555.

[3] Willing, R., and Kim, I. Y., 2009, "A holistic numerical model to predict strain hardening and damage of UHMWPE under multiple total knee replacement kinematics and experimental validation," J. Biomech., **42**, pp. 2520–2527.

[4] van den Heever, D. J., Scheffer, C., Erasmus, P., and Dillon, E., 2011, "Contact stresses in patient-specific unicompartmental knee replacement," Clin. Biomech., **26**, pp. 159–166.

[5] Taylor, M., Bryan, R., and Galloway, F., 2013, "Accounting for patient variability in finite element analysis of the intact and implanted hip and knee: A review," Int. J. Numer. Methods Biomed. Eng., **29**, pp. 273–292.

[6] Simpson, D. J., Gray, H., D'Lima, D. D., Murray, D. W., and Gill, H. S., 2008, "The effect of bearing congruency, thickness and alignment on the stresses in unicompartmental knee replacements," Clin. Biomech., **23**, pp. 1148–1157.

[7] O'Brien, S., Luo, Y., Wu, C., Petrak, M., Bohm, E., and Brandt, J-M., 2013, "Computational development of a polyethylene wear model for articular and backside surfaces in modular total knee replacements," Tribol. Int., **59**, pp. 284–291.

[8] Morra, E. A., Heim, C. S., and Greenwald, A. S., 2012, "Preclinical computational models: Predictors of tibial insert damage patterns in total knee arthroplasty," J. Bone Joint Surg. Am., **94-A**(18), p. e137: 1–5.

[9] Morra, E. A., and Greenwald, A. S., 2005, "Polymer insert stress in total knee designs during high-flexion activities: A finite element study," J. Bone Jt. Surg., **87-A**(Supplement 2), pp. 120–124.

[10] Mamat, N., Nor, M., Osman, N. A. A., and Oshkour, A., 2012, "Numerical measurement of contact pressure in the tibiofemoral joint during gait," IEEE, Penang, pp. 38–43.

[11] Knight, L. A., Pal, S., Coleman, J. C., Bronson, F., Haider, H., Levine, D. L., Taylor, M., and Rullkoetter, P. J., 2007, "Comparison of long-term numerical and experimental total knee replacement wear during simulated gait loading," J. Biomech., **40**, pp. 1550–1558.

[12] Ketata, H., Krichen, A., Kharrat, M., and Dammak, M., 2006, "Mechanical response of polyethylene tibial component using compression loading contact test: Experimental and finite element analysis," Technol. Health Care, **14**, pp. 479–487.

[13] Halloran, J. P., Petrella, A. J., and Rullkoetter, P. J., 2005, "Explicit finite element modeling of total knee replacement mechanics," J. Biomech., **38**, pp. 323–331.

[14] Catani, F., Innocenti, B., Belvedere, C., Labey, L., Ensini, A., and Leardini, A., 2010, “The Mark Coventry Award: Articular contact estimation in TKA using in vivo kinematics and finite element analysis,” Clin. Orthop., **468**, pp. 19–28.

[15] Baldwin, M. A., Clary, C. W., Fitzpatrick, C. K., Deacy, J. S., Maletsky, L. P., and Rullkoetter, P. J., 2012, “Dynamic finite element knee simulation for evaluation of knee replacement mechanics,” J. Biomech., **45**, pp. 474–483.

[16] Godest, A. C., Beaugonin, M., Haug, E., Taylor, M., and Gregson, P. J., 2002, “Simulation of a knee joint replacement during a gait cycle using explicit finite element analysis,” J. Biomech., **35**(2), pp. 267–275.

[17] Fregly, B. J., Bei, Y., and Sylvester, M. E., 2003, “Experimental evaluation of an elastic foundation model to predict contact pressures in knee replacements,” J. Biomech., **36**, pp. 1659–1668.

[18] Fregly, B. J., Sawyer, W. G., Harman, M. K., and Banks, S. A., 2005, “Computational wear prediction of a total knee replacement from in vivo kinematics,” J. Biomech., **38**, pp. 305–314.

[19] Bergstrom, J. S., Kurtz, S. M., Rimnac, C. M., and Edidin, A. A., 2002, “Constitutive modeling of ultra-high molecular weight polyethylene under large-deformation and cyclic loading conditions,” Biomaterials, **23**(11), pp. 2329–2343.

[20] Fisher, J., and Belytschko, T., 2007, A First Course in Finite Elements, John Wiley & Sons, Ltd.

[21] Hamill, J., and Knutzen, K. M., 2009, Biomechanical Basis of Human Movement, Lippincott Williams & Wilkins, Philadelphia, PA.

[22] Blunn, G. W., Joshi, A., Minns, R. J., Lidgren, L., Lilley, P., Ryd, L., Engelbrecht, E., and Walker, P. S., 1997, “Wear in retrieved condylar knee arthroplasties: A comparison of wear in different designs of 280 retrieved condylar knee prostheses,” J. Arthroplasty, **12**(3), pp. 281–290.

[23] ISO/IEC, 2009, "Implants for surgery - Wear of total knee-joint prostheses - Part 1: Loading and displacement parameters for wear-testing machines with load control and corresponding environmental conditions for test," ISO 14243-1.

[24] Beer, F. P., Johnston, E. R. Jr., DeWolf, J. T., and Mazurek, D. F., 2012, Mechanics of Materials, McGraw Hill, New York, NY.

[25] Stephens, R. I., Fatemi, A., Stephens, R. R., and Fuchs, H. O., 2001, Metal Fatigue in Engineering, John Wiley & Sons, Inc., New York, NY.

[26] Kurtz, S. M., Pruitt, L. P., Jewett, C. W., Crawford, R. P., Crane, D. J., Edidin, A. A., 1998, “The yielding, plastic flow, and fracture behavior of ultra-high molecular weight polyethylene used in total joint replacements,” Biomaterials, **19**, pp. 1989-2003.

[27] Kurtz, S. M., Villarraga, M. L., Herr, M. P., Bergstrom, J. S., Rimnac, C. M., and Edidin, A. A., 2002, “Thermomechanical behavior of virgin and highly crosslinked ultra-high

molecular weight polyethylene used in total joint replacements," Biomaterials, **23**, pp. 3681–3697.

[28] Gnecco, E., and Meyer, E., eds., 2007, Fundamentals of Friction and Wear, Springer, Berlin.

[29] Rullkoetter, P. J., and Gabriel, S., 2000, "Viscoelastic behavior of UHMWPE TKR components," Transactions of the Annual Meeting of the Orthopaedic Research Society, ORS, Orlando, Fla., p. 0562.

[30] Vincent, J., 2012, "Basic elasticity and viscoelasticity," Structural Biomaterials, Princeton University Press, Princeton, NJ, pp. 1–28.

[31] University of Cambridge, 2004, "Viscoelasticity and hysteresis," Dissem. IT Promot. Mater. Sci. [Online]. Available: http://www.doitpoms.ac.uk/tlplib/bioelasticity/viscoelasticity-hysteresis.php. [Accessed: 22-Jul-2014].

[32] 2014, "Plasticity Tresca Model," SolidWorks Help [Online]. Available: http://help.solidworks.com/2012/English/SolidWorks/cworks/Tresca_Plasticity_Model_(Kinematic_Isotropic).htm. [Accessed: 30-Jul-2014].

[33] Quinci, F., Dressler, M., Strickland, A. M., and Limbert, G., 2014, "Towards an accurate understanding of UHMWPE visco-dynamic behaviour for numerical modelling of implants," J. Mech. Behav. Biomed. Mater., **32**, pp. 62–75.

[34] Quinci, F., Dressler, M., Strickland, A. M., and Limbert, G., 2014, "Towards an accurate understanding of UHMWPE visco-dynamic behaviour for numerical modelling of implants," J. Mech. Behav. Biomed. Mater., **32**, pp. 62–75.

[35] Bergstrom, J.S., Rimnac, Clare M., and Kurtz, Steven M., 2004, "An augmented hybrid constitutive model for simulation of unloading and cyclic loading behavior of conventional and highly crosslinked UHMWPE," Biomaterials, **25**(11), pp. 2171–2178.

[36] Bergstrom, J. S., Rimnac, C. M., and Kurtz, S. M., 2003, "Prediction of multiaxial mechanical behavior for conventional and highly crosslinked UHMWPE using a hybrid constitutive model," Biomaterials, **24**, pp. 1365–1380.

[37] Patten, E. W., Van Critters, D. W., Ries, M. D., and Pruitt, L. A., 2014, "Quantifying cross-shear under translation, rolling, and rotation, and its effect on UHMWPE wear," Wear, **313**, pp. 125–134.

[38] O'Brien, S. T., Bohm, E. R., Petrak, M. J., Wyss, U. P., and Brandt, J-M., 2014, "An energy dissipation and cross shear time dependent computational wear model for the analysis of polyethylene wear in total knee replacements," J. Biomech., **47**, pp. 1127–1133.

[39] Strickland, A. M., Dressler, M. R., and Taylor, M., 2012, "Predicting implant UHMWPE wear in-silico: A robust, adaptable computational–numerical framework for future theoretical models," Wear, **274-275**, pp. 100–108.

[40] Abdelgaied, A., Liu, F., Brockett, C., Jennings, L., Fisher, J., and Jin, Z., 2011, "Computational wear prediction of artificial knee joints based on a new wear law and

formulation," J. Biomech., **44**(6), pp. 1108–1116.

[41] Estupinan, J. A., Wright, T. M., and Bartel, D. L., 2001, "Simulation predicts location and orientation of initial cracks in UHMWPE in low conformity sliding contact," Transactions of the Orthopaedic Research Society, ORS, San Francisco, CA, USA, p. 0220.

[42] Sathasivam, S., and Walker, P. S., 1998, "Computer model to predict subsurface damage in tibial inserts of total knees," J. Orthop. Res., **16**, pp. 564–571.

[43] Bartel, D. L., Bicknell, V. L., and Wright, T. M., 1986, "The effect of conformity, thickness, and material on stresses in ultra-high molecular weight components for a total joint replacement," J. Bone Joint Surg. Am., **68**, pp. 1041–1051.

[44] Hurwitz, D. E., Sumner, D. R., Andriacchi, T. P., and Sugar, D. A., 1998, "Dynamic knee loads during gait predict proximal bone distribution," J. Biomech., **31**, pp. 423–430.

[45] Shelbourne, K. B., Torry, M. R., and Pandy, M. G., 2005, "Muscle, ligament, and joint-contact forces at the knee during walking," Med. Sci. Sports Exerc., pp. 1948–1956.

[46] Medlin, D. J., Charlebois, S., Swarts, D., and Shetty, R., 2003, "Metallurgical characterization of a porous tantalum biomaterial (Trabecular Metal^{TM}) for orthopaedic implant applications," Medical Device Materials: Proceedings of the Materials & Processes for Medical Device Conference, Shrivastava, S., ed., ASM International, Anaheim, CA, pp. 394–398.

[47] ASM Materials for Medical Devices Database Committee, 2009, "CoCrMo," Materials and Coatings for Medical Devices: Cardiovascular, ASM International, Materials Park, OH, pp. 79–89.

[48] 2013, "Abaqus Analysis User's Manual, Volume III: Part V, Materials." Online Documentation Help, Dessault Systèmes.

[49] Guedes, R. M., 2011, "Analysis of temperature and aging effects on biomedical ultra-high molecular weight polyethylene's grades using a viscoelastic model," Polym. Test., **30**, pp. 641–650.

[50] Arzoumanidis, G.A., and Liechti, K.M., 2003, "Linear viscoelastic property measurement and its significance for some nonlinear viscoelasticity models," Mech. Time-Depend. Mater., **7**, pp. 209–250.

[51] 2013, "Abaqus Analysis User's Manual, Volume IV: Elements, Three-dimensional solid element library." Online Documentation Help, Dessault Systèmes.

[52] Perez-Gonzalez, A., Fenollosa-Esteve, C., Sancho-Bru, J. L., Sanchez-Marin, F. T., Vergara, M., and Rodriguez-Cervantes, P. J., 2008, "A modified elastic foundation contact model for application in 3D models of the prosthetic knee," Med. Eng. Phys., **30**, pp. 387–398.

[53] Guo, Y., Zhang, X., and Chen, W., 2009, "Three-dimensional finite element simulation of total knee joint in gait cycle," Acta Mech. Solida Sin., **22**(4), pp. 347–351.

[54] Johnson, K. L., 1985, Contact Mechanics, Cambridge University Press, New York, NY. USA.

[55] Deeg, E. W., 1992, “New algorithms for calculating Hertzian stresses, deformations, and contact zone parameters,” AMP J. Technol., **2**, pp. 14–24.

[56] Bell, C., Walker, P. S., Abeysundera, M. R., Simmons, J. M. H., King, P. M., and Blunn, G. W., 1996, “Effect of oxidation on the delamination of ultrahigh-molecular-weight polyethylene tibial components,” J. Arthroplasty, **13**(3), pp. 280–290.

[57] Pruitt, L. A., 2005, “Deformation, yielding, fracture and fatigue behavior of conventional and highly cross-linked ultra high molecular weight polyethylene,” Biomaterials, **26**, pp. 905–915.

CHAPTER 4

COMPARISON BETWEEN EXPERIMENTS AND SIMULATIONS

In this chapter we evaluate how accurately the local stress in the tibial insert simulated with the finite element model (Chapter 3) predicts the fatigue crack damage observed in the knee simulator tested tibial insert (Chapter 2). The applied loading and kinematics are identical in the mechanical knee simulator testing and finite element simulations. The capability of von Mises, principal, and shear stress maxima for predicting fatigue crack damage are examined. Figure 4.1 illustrates the experimentally measured fatigue crack damage contour superimposed with the locations of the maximum von Mises stress results within the tibial insert for each of the twenty output frames during the stance phase of the gait cycle, for the linear elastic (Figure 4.1 A) and linear viscoelastic (Figure 4.1 B) UHMWPE material models. The twenty output frames are spaced 0.0305-second time intervals apart. We observe that for both material models the maximum von Mises stress occurs in the posterior-medial region of the tibial insert for the majority of the simulated stance phase. The maximum von Mises stress within the tibial insert for the first two output frames, which occur at 0.0305 and 0.0610 seconds out of the total 0.6100-second simulation, are situated at the most anterior edge of the measured fatigue crack damage region for each UHMWPE material model simulation. However, von Mises stress magnitudes up to 80 MPa occur elsewhere in the tibial insert during the latter part of the stance phase, indicating that maximum von Mises alone is insufficient for predicting fatigue crack damage.

Figure 4.2 shows the subsurface areas for which the von Mises stress exceeds the yield stress of the material, for the linear elastic model (Figure 4.2 A), and the linear viscoelastic model

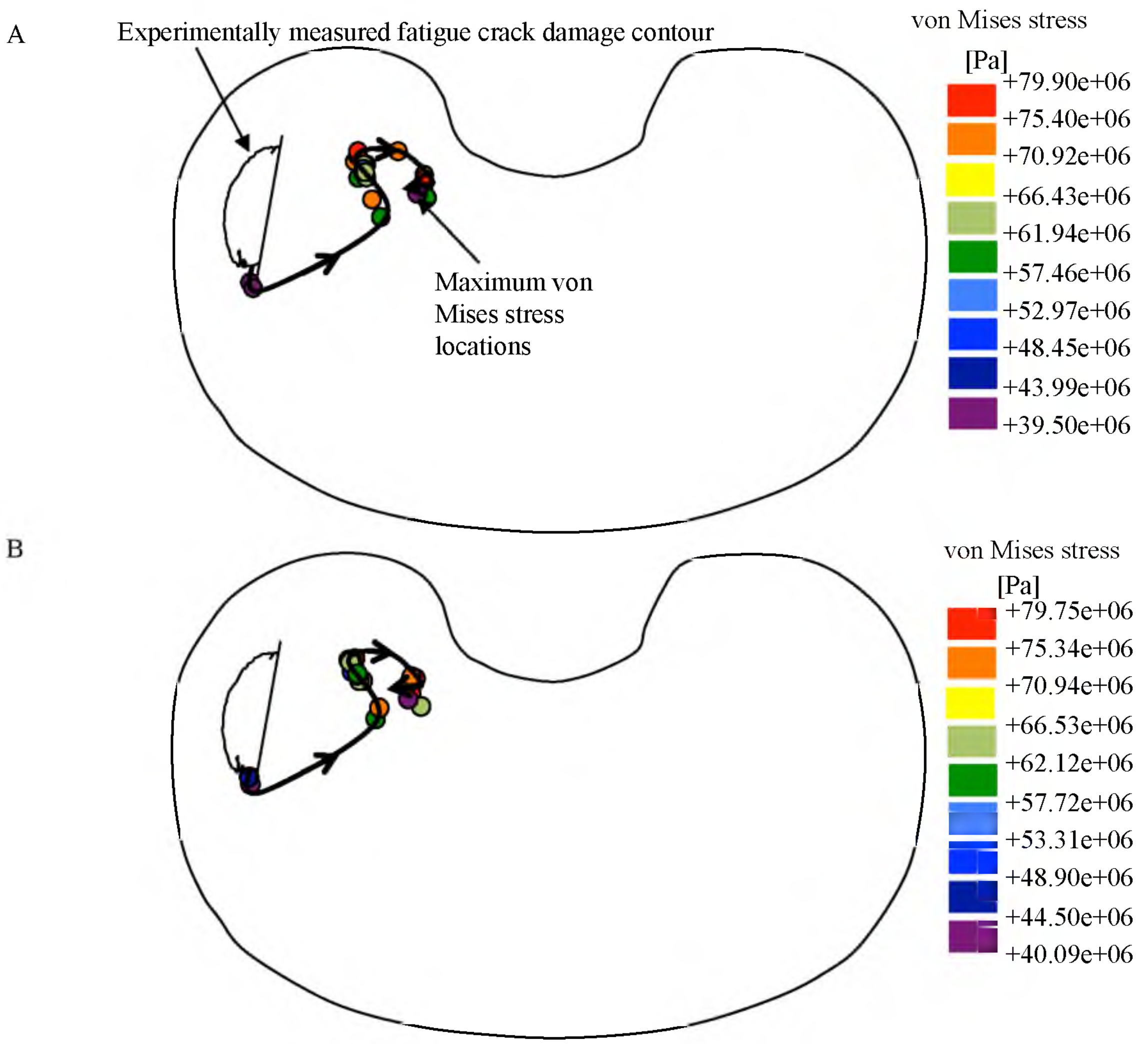

Figure 4.1: Top view of the maximum von Mises stress locations (colored dots) in the medial condyle of the (left) tibial insert stance phase with the experimentally measured fatigue crack damage contour superimposed. The black line and arrowheads indicate the sequence in which the von Mises stress maxima occur. (A) The maximum von Mises stress locations for the linear elastic model. (B) The maximum von Mises stress locations for the linear viscoelastic model.

(Figure 4.2 B), respectively. The subsurface areas were recorded at the depth at which the yield stress-exceeding subsurface area is largest, between approximately 1 and 3 mm below the surface. Partially transparent shaded regions, depicting the locations where the local von Mises stress exceeds the yields stress, are created for each output frame of the simulation and then superimposed for the entire stance phase. Darker areas (more opaque) indicate multiple output frames for which that region exceeds the yield stress, while lighter (more transparent) regions

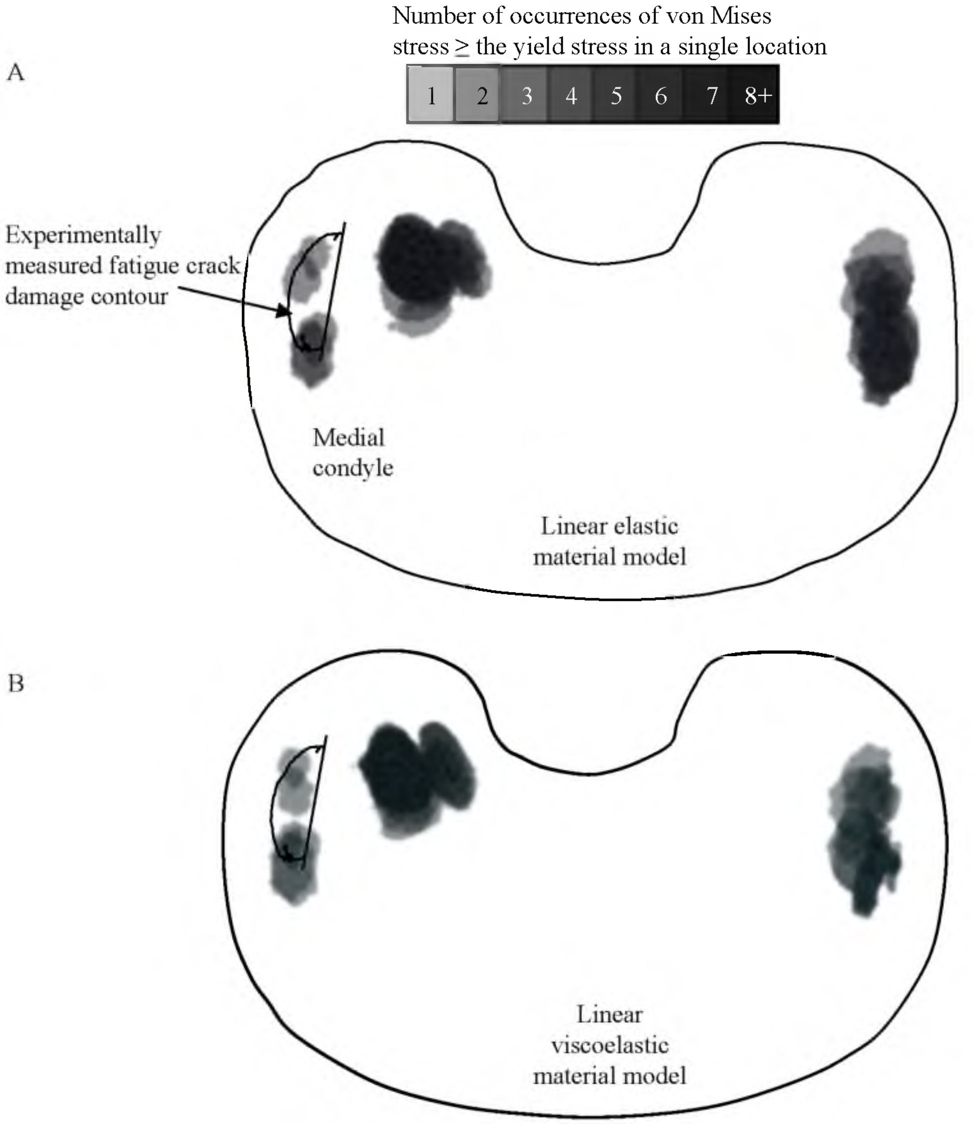

Figure 4.2: Top view of left tibial insert and experimentally determined fatigue crack damage contour superimposed with the magnitude of the simulated von Mises stress in excess of the yield stress (≥ 21 MPa [1]) for each output frame. (A) Linear elastic model and (B) linear viscoelastic material model.

indicate fewer frames for which that region exceeds the yield stress. The experimentally determined fatigue crack damage contour is superimposed on each plot. Figure 4.2 illustrates that this method is only partially predictive of fatigue crack damage. While the fatigue crack damage region is identified by the simulation as a region where the von Mises stress exceeds the yield stress, other regions of the tibial insert also experience multiple instances where the von Mises stress exceeds the yield stress, indicated by darkly shaded regions in the nondamaged region of the tibial insert. We also observe that the predictions of the linear elastic and linear viscoelastic model are quite similar.

Figure 4.3 shows the magnitude of the maximum principal stress in the medial condyle of the tibial insert for each of the twenty output frames of the stance phase simulation. The experimentally measured fatigue crack damage contour is superimposed on the simulation results. Only the viscoelastic model results are shown because of the similarity of the results for both UHMWPE material models. Figure 4.3 A shows the maximum compressive (negative) principal stress locations. The highest magnitude compressive stress occurs in the posterior portion of the medial condyle at approximately 5.7 mm and 9.5 mm lateral to the most lateral point on the fatigue crack damage contour.

In contrast, the maximum tensile (positive) principal stress locations shown in Figure 4.3 B illustrate that the locations of the maximum principal tensile stress are clustered near the posterior portion of the fatigue crack damage contour, approximately 2.9 mm lateral to and 2.1 mm anterior to the most lateral point of the posterior portion of the fatigue crack damage contour. These principal stress maxima have magnitudes up to 140 MPa, substantially higher than the maxima seen elsewhere in the medial condyle. A maximum principal stress with a relatively high magnitude (> 94.8 MPa) also occurs, during a single instance during the stance phase, near the anterior portion of the fatigue crack damage contour at 1.5 mm lateral to and 1.8 mm anterior to the most lateral point on the anterior edge of the fatigue crack damage contour (yellow dot). The maximum principal stress that occurs near the fatigue crack damage is of significantly greater

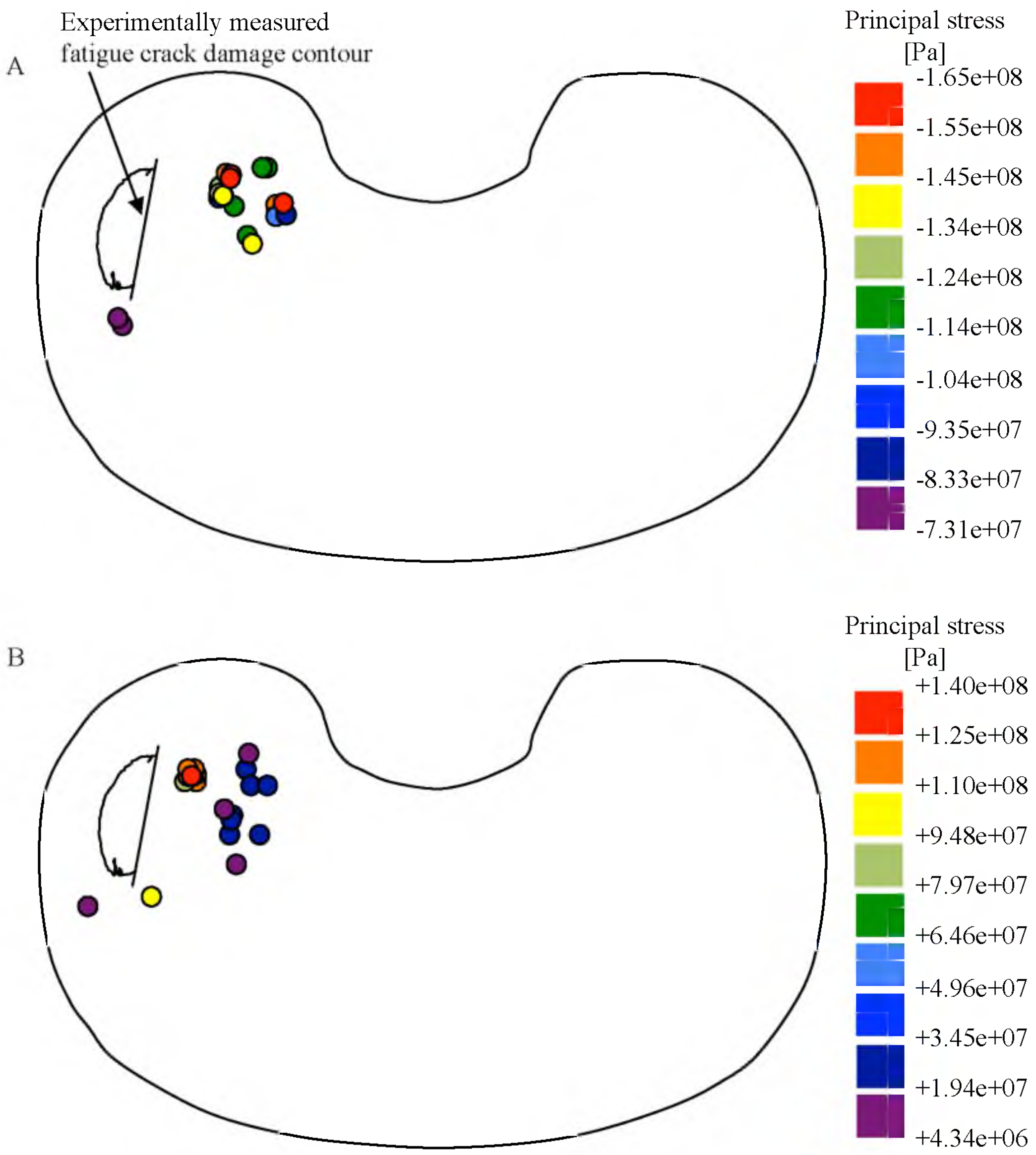

Figure 4.3: Top view of the maximum principal stress locations (colored dots) from each output frame in the medial condyle of the (left) tibial insert during the stance phase with the experimentally measured fatigue crack damage contour superimposed. (A) The maximum compressive principal stress locations, and (B) maximum tensile principal stress locations, both for the linear viscoelastic model.

magnitude, between 79.7 MPa and 140.0 MPa, than the maximum principal stress occurring elsewhere in the tibial insert medial condyle, ranging between 4.34 MPa and 34.5 MPa and generally not exceeding the yield stress of the UHMWPE.

These results indicate that the maximum principal stress may be a more accurate predictor of fatigue crack damage than the von Mises stress, as the maximum principal stress locations are concentrated within < 3 mm outside of the experimentally observed fatigue crack damage, compared to spread over locations ≥ 5.6 mm from the outer edge of the fatigue crack damage for the maximum von Mises stress. The correlation between high tensile principal stress and fatigue crack damage is supported by previous results documented in the literature, where the predicted locations of high tensile principal stress values occurred near the edges of UHMWPE damage induced by a sliding indenter [2].

We also examine the relationship between the location of maximum shear stress during the stance phase and the location of the fatigue crack damage. Figure 4.4 shows the locations of the maximum *x-y* direction shear stress in the medial condyle of the tibial insert for each output frame of the stance phase simulation using the linear viscoelastic model with the experimentally measured fatigue crack damage contour superimposed. Maximum shear stress occurs in the posterior portion of the medial condyle, with the highest magnitude maximum shear stress during the stance phase located at approximately 2.6 mm lateral to and 1.9 mm anterior to the most lateral point on the posterior edge of the fatigue crack damage contour. Figure 4.4 B shows the locations of maximum *x-z* direction shear stress for each output frame, located between 3.3 and 5.0 mm lateral to and between 0.8 and 2.1 mm anterior to the most lateral point on the posterior edge of the fatigue crack damage contour. Figure 4.4 C shows the locations of the maximum *y-z* direction shear stress for each output frame, located in line with, in the anterior posterior direction, and 8.3 mm lateral to, the most lateral point on the posterior edge of the fatigue crack damage contour. The plots of the locations of maximum *x-y* and *x-z* shear stress for each output frame exhibit clustering of the maximum shear stress locations within ≤ 5 mm from the

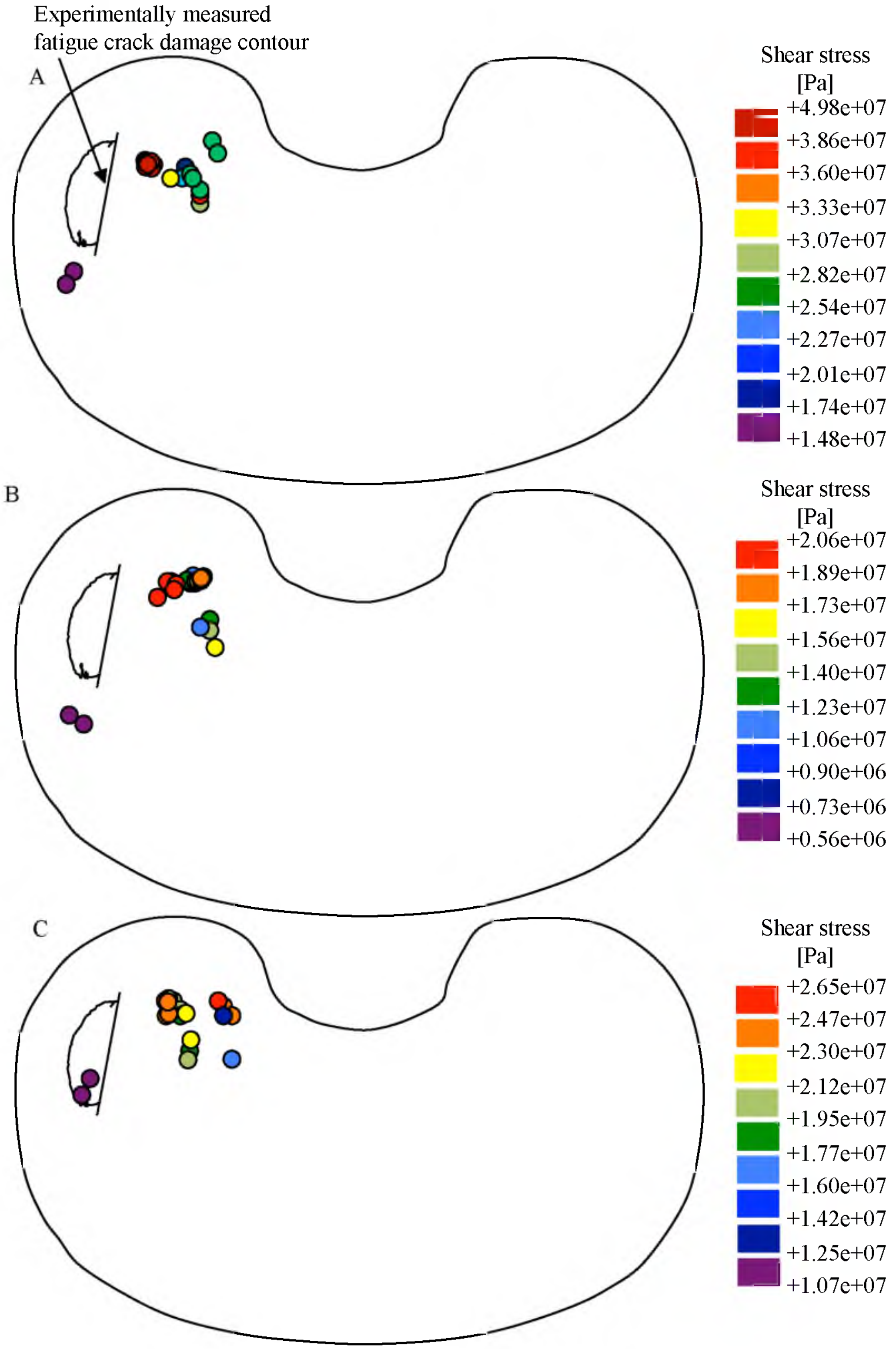

Figure 4.4: Top view of the maximum shear stress locations (colored dots) from each output frame for the linear viscoelastic material model in the medial condyle of the (left) tibial insert during the stance phase with the experimentally measured fatigue crack damage contour superimposed. (A) The maximum *x-y* direction shear stress locations. (B) The maximum *x-z* direction shear stress locations. (C) The maximum *y-z* direction shear stress locations.

fatigue crack damage contour, while the locations of maximum *y-z* shear stress are spread over the posterior portion of the medial condyle.

These high shear stress magnitudes may contribute to the development of the fatigue crack damage, as has been suggested previously in the literature [3,4]. Bartel et al. [4] observed that the depth of the maximum shear stress, 1- 2 mm subsurface, is associated with the depth at which initiation of subsurface cracks in tibial inserts occurs. In this work the initiation location of the subsurface fatigue crack damage is unknown. Further analysis is necessary to determine whether the location of the high shear stress maxima corresponds to the location of fatigue crack initiation.

4.1 References

[1] Pruitt, L. A., 2005, "Deformation, yielding, fracture and fatigue behavior of conventional and highly cross-linked ultra high molecular weight polyethylene," Biomaterials, **26**, pp. 905–915.

[2] Estupinan, J. A., Wright, T. M., and Bartel, D. L., 2001, "Simulation predicts location and orientation of initial cracks in UHMWPE in low conformity sliding contact," Transactions of the Orthopaedic Research Society, ORS, San Francisco, CA, USA, p. 0220.

[3] Blunn, G. W., Walker, P. S., Joshi, A., and Hardinge, K., 1991, "The dominance of cyclic sliding in producing wear in total knee replacements," Clin. Orthop., (274), pp. 253–260.

[4] Bartel, D. L., Bicknell, V. L., and Wright, T. M., 1986, "The effect of conformity, thickness, and material on stresses in ultra-high molecular weight components for a total joint replacement," J. Bone Joint Surg. Am., **68**, pp. 1041–1051.

CHAPTER 5

CONCLUSIONS AND FUTURE WORK

5.1 Conclusions

The goals of this work were to: (1) quantify fatigue crack damage in polyethylene tibial inserts and (2) develop a corresponding finite element model to predict fatigue cracking. For the first objective a fatigue crack damage measurement technique was developed based on transillumination to highlight fatigue crack damage and image processing to identify and measure fatigue crack damage areas. This technique was tested on two tibial inserts. It was determined that this technique allows fatigue crack damage to be successfully identified and measured for the range of fatigue crack damage present in the two tested tibial inserts.

This technique presents a precise, objective method for measuring subsurface fatigue crack damage and improves on existing techniques due to its usability for subsurface damage measurement and reduced reliance on manual damage identification and measurement. The precision of this measurement process is within 1 mm^2 based on the scale bar used in capturing the images. The use of an edge detection and cubic spline-fitting algorithm to measure the fatigue crack damage area reduces the subjectivity present in other image-based wear identification methods. The accuracy has been evaluated qualitatively but has not yet been quantitatively assessed based on previously validated methods, as suggested for future work.

A dynamic finite element model of the tibial insert and femoral component during a single stance phase of the knee simulator testing was created and two UHMWPE material models, linear elastic and linear viscoelastic, were tested to simulate local stress in the tibial insert during the stance phase of the gait cycle. The results of the two simulations demonstrate that including viscoelastic effects influences both the magnitude and location of the predicted maximum stress in the tibial insert.

We determined that there was a root mean square difference of 2.52% of the overall maximum von Mises stress magnitude for the twenty output frame von Mises stress maxima between the linear elastic and linear viscoelastic material models. Although the root mean square difference was small, the maximum differences of 4.38 MPa in the medial condyle and 10.12 MPa in the lateral condyle, or 5.49% and 21.0%, respectively, of the overall maximum in the respective condyles using the linear viscoelastic model, indicates that the material model has a substantial impact on the magnitude of the maximum von Mises stress. The locations of the von Mises stress magnitudes in excess of the yield stress were similar, with an 81% overlap between the areas over which the yield stress is exceeded between the linear elastic and linear viscoelastic material model simulations.

In addition, the results of the two simulations indicate that the plastic behavior of UHMWPE above the yield stress of the material is important for the knee simulator loading conditions simulated in this work. The von Mises stress maxima for both the linear elastic and linear viscoelastic material model simulations were well above the 21 MPa yield stress of the UHMWPE for the majority of the stance phase simulation. Because permanent plastic deformation is not accounted for, the linear elastic and linear viscoelastic models under-predict the UHMWPE deformation in regions where the yield stress is exceeded. This results in under-prediction of the contact area and over-prediction of contact stress.

Finally, it was determined that the magnitude of the local von Mises stress by itself is insufficient for predicting fatigue crack damage. However, maximum tensile principal stress and shear stress were predictive of fatigue crack damage, with maxima for each occurring in close proximity, at distances of < 3 mm and ≤ 5 mm, respectively, to the experimentally determined fatigue crack damage contour.

5.2 Future Work

Further validation of the transillumination-based imaging and fatigue crack damage measurement technique is needed to confirm its robustness and accuracy. Although this technique performed well for the two specimens examined in this work, the method has not been validated for more than a small range of fatigue crack damage characteristics.

One specific validation necessary to confirm the accuracy and robustness of the fatigue crack imaging and measurement method is to confirm the location and depth of the subsurface crack by a previously validated method, such as micro-CT or thin-slice microscopy. It should be confirmed that fatigue crack damage existing at a depth of 1-2 mm subsurface is detectable using the imaging method developed in this work. Because the majority of fatigue cracks initiate and grow at this depth within the tibial insert the ability to detect fatigue cracks at this depth is critical. This validation would also allow the location of the fatigue crack initiation to be confirmed and compared to the modeled tensile principal stress maxima and shear stress maxima, adding additional support to the correlation between high tensile and shear stress magnitudes and fatigue crack damage.

The results of this work indicate that finite element modeling has the potential for predicting fatigue crack damage. However, the stress results for the stance phase simulation, with maximum von Mises stress magnitudes consistently in excess of the UHMWPE yield stress, suggest that consideration of the plastic behavior of UHMWPE is necessary for accurate prediction of the maximum von Mises, principal, and shear stress during the stance phase simulation under knee simulator loading conditions. The simulations performed with the linear elastic and linear viscoelastic UHMWPE material models likely under-predict strain and over-predict maximum von Mises stress.

This weakness will be addressed by performing a third simulation of the stance phase using a linear elastic perfectly plastic UHMWPE material model. The perfectly plastic material model is selected over other isotropic plasticity models based on the lack of available plastic stress-strain data for the specific UHMWPE used in this work. The linear elastic perfectly plastic material model simulation can be performed using the measured material parameters listed in Table 3.1 and a yield stress of 21 MPa [57]. This third material model will allow the influence of permanent plastic deformation at stress in excess of the yield stress to be evaluated. More accurate simulation of the UHMWPE behavior at stress in excess of the yield stress will provide a more accurate picture of the relationship between simulated tibial insert stress and the experimentally observed fatigue crack damage.

APPENDIX A

DISPLACEMENTS AND LOADS APPLIED DURING KNEE SIMULATOR TESTING

Table A.1: Flexion-extension angle and pneumatically applied loads during knee simulator testing

Percent of gait cycle [%]	Flexion-extension* angle [degrees]	Axial force [N]	Anterior-posterior* force [N]	Internal-external* torque [Nm]
0	0.00	168	0.00	0
1	0.17	598	-25.31	-0.02
2	0.69	1457	-91.56	-0.10
3	1.53	1887	-173.44	-0.21
4	2.65	1783	-239.69	-0.35
5	4.00	1531	-265.00	-0.50
6	5.53	1279	-246.43	-0.65
7	7.16	1175	-194.40	-0.79
8	8.84	1270	-119.22	-0.90
9	10.47	1531	-35.78	-0.98
10	12.00	1887	39.40	-1.00
11	13.35	2244	91.43	-0.99
12	14.47	2505	110.00	-0.96
13	15.31	2600	109.62	-0.90
14	15.83	2570	108.47	-0.83
15	16.00	2482	106.57	-0.73
16	15.96	2342	103.92	-0.62
17	15.83	2160	100.53	-0.48
18	15.61	1947	96.43	-0.33
19	15.32	1719	91.64	-0.16
20	14.95	1491	86.18	0.03
21	14.51	1279	80.08	0.23
22	14.01	1096	73.37	0.44
23	13.45	956	66.10	0.67
24	12.84	868	58.29	0.91
25	12.20	838	50.00	1.16
26	11.53	848	41.25	1.42
27	10.85	877	32.11	1.68
28	10.15	925	22.62	1.95
29	9.47	991	12.83	2.23
30	8.80	1072	2.80	2.50
31	8.16	1167	-7.44	2.77
32	7.55	1274	-17.81	3.05
33	6.99	1389	-28.26	3.32
34	6.49	1511	-38.74	3.58
35	6.05	1636	-49.19	3.84
36	5.68	1761	-59.56	4.09
37	5.39	1882	-69.80	4.33
38	5.17	1998	-79.83	4.56
39	5.04	2105	-89.62	4.77
40	5.00	2200	-99.11	4.97
41	5.13	2281	-108.25	5.16
42	5.51	2347	-117.00	5.33

Table A.1: Continued

Percent of gait cycle [%]	Flexion-extension* angle [degrees]	Axial force [N]	Anterior-posterior* force [N]	Internal-external* torque [Nm]
43	6.14	2394	-125.29	5.48
44	7.02	2424	-133.10	5.62
45	8.13	2434	-140.37	5.73
46	9.47	2409	-147.08	5.83
47	11.02	2336	-153.18	5.90
48	12.76	2217	-158.64	5.96
49	14.69	2059	-163.43	5.99
50	16.78	1867	-167.53	6.00
51	19.01	1651	-170.92	5.93
52	21.36	1419	-173.57	5.74
53	23.81	1182	-175.47	5.43
54	26.33	950	-176.62	5.01
55	28.90	734	-177.00	4.50
56	31.50	542	-171.40	3.93
57	34.10	384	-155.13	3.31
58	36.67	266	-129.80	2.69
59	39.19	192	-97.88	2.07
60	41.64	168	-62.50	1.50
61	43.99	168	-27.12	0.99
62	46.22	168	4.80	0.57
63	48.31	168	30.13	0.26
64	50.24	168	46.40	0.07
65	51.98	168	52.00	0
66	53.53	168	51.90	0
67	54.87	168	51.58	0
68	55.98	168	51.06	0
69	56.86	168	50.34	0
70	57.49	168	49.43	0
71	57.87	168	48.32	0
72	58.00	168	47.03	0
73	57.82	168	45.58	0
74	57.27	168	43.97	0
75	56.37	168	42.21	0
76	55.13	168	40.32	0
77	53.56	168	38.32	0
78	51.67	168	36.22	0
79	49.51	168	34.03	0
80	47.08	168	31.79	0
81	44.43	168	29.49	0
82	41.58	168	27.17	0
83	38.58	168	24.83	0
84	35.45	168	22.51	0
85	32.25	168	20.21	0

Table A.1: Continued

Percent of gait cycle [%]	Flexion-extension* angle [degrees]	Axial force [N]	Anterior-posterior* force [N]	Internal-external* torque [Nm]
86	29.00	168	17.97	0
87	25.75	168	15.78	0
88	22.55	168	13.68	0
89	19.42	168	11.68	0
90	16.42	168	9.79	0
91	13.57	168	8.03	0
92	10.92	168	6.42	0
93	8.49	168	4.97	0
94	6.33	168	3.68	0
95	4.44	168	2.57	0
96	2.87	168	1.66	0
97	1.63	168	0.94	0
98	0.73	168	0.42	0
99	0.18	168	0.10	0

* Positive direction is listed first

APPENDIX B

MOTION RESTRAINT FORCES APPLIED DURING KNEE SIMULATOR TESTING AVERAGED OVER 19 SIMULATOR CYCLES AND ACROSS 4 TEST STATIONS

Table B.1: Buffer forces and torques applied during knee simulator testing

Percent of gait cycle [%]	Right buffer force for internal-external* torque [N]	Left buffer force for internal-external* torque [N]	Total anterior-posterior* buffer force [N]
0	-1.98	-2.87	-144.29
1	-1.38	-2.62	-185.12
2	-0.78	-2.37	-225.94
3	-0.87	-2.07	-249.90
4	-0.96	-1.76	-273.85
5	0.56	-0.74	-273.56
6	2.07	0.29	-273.27
7	1.68	-0.39	-264.08
8	1.30	-1.06	-254.89
9	-0.37	-1.83	-159.01
10	-2.05	-2.59	-63.14
11	-2.25	-3.18	-4.58
12	-2.44	-3.76	53.97
13	-3.30	-4.17	66.01
14	-4.15	-4.57	78.06
15	-5.82	-4.23	91.33
16	-7.49	-3.89	104.60
17	-8.93	-3.74	117.32
18	-10.36	-3.59	130.05
19	-10.85	-3.76	127.26
20	-11.34	-3.93	124.47
21	-11.21	-2.29	115.99
22	-11.08	-0.65	107.51
23	-11.42	-0.35	106.27
24	-11.77	-0.05	105.03
25	-12.07	0.42	91.00
26	-12.37	0.90	76.98
27	-12.92	1.57	60.75
28	-13.47	2.24	44.52
29	-14.57	1.91	36.32
30	-15.67	1.57	28.11
31	-14.87	2.70	19.08
32	-14.08	3.82	10.05
33	-13.78	3.86	-0.39
34	-13.47	3.90	-10.84
35	-13.10	3.73	-23.73
36	-12.73	3.56	-36.63
37	-12.66	3.37	-52.68
38	-12.58	3.19	-68.73
39	-13.24	2.43	-87.56
40	-13.90	1.67	-106.39
41	-13.40	2.10	-123.08
42	-12.90	2.54	-139.76

Table B.1: Continued

Percent of gait cycle [%]	Right buffer force for internal-external* torque [N]	Left buffer force for internal-external* torque [N]	Total anterior-posterior* buffer force [N]
43	-13.51	1.93	-151.11
44	-14.12	1.32	-162.46
45	-13.95	2.25	-151.33
46	-13.78	3.19	-140.21
47	-13.86	3.74	-133.74
48	-13.94	4.30	-127.27
49	-14.60	5.43	-132.64
50	-15.26	6.56	-138.02
51	-15.97	9.16	-146.82
52	-16.68	11.76	-155.62
53	-16.78	15.89	-164.71
54	-16.89	20.01	-173.79
55	-14.97	25.16	-175.23
56	-13.04	30.31	-176.67
57	-11.29	31.29	-174.29
58	-9.53	32.27	-171.91
59	-8.18	29.08	-124.49
60	-6.82	25.90	-77.08
61	-7.88	17.93	-42.51
62	-8.93	9.96	-7.95
63	-10.31	2.73	3.49
64	-11.70	-4.51	14.93
65	-12.68	-6.11	11.46
66	-13.66	-7.71	7.98
67	-13.30	-7.78	20.60
68	-12.95	-7.84	33.23
69	-15.17	-9.06	41.44
70	-17.40	-10.27	49.65
71	-16.61	-9.48	54.38
72	-15.83	-8.69	59.11
73	-15.34	-8.65	54.89
74	-14.85	-8.62	50.67
75	-12.44	-6.61	51.20
76	-10.02	-4.60	51.73
77	-9.63	-4.26	50.35
78	-9.24	-3.92	48.97
79	-8.64	-3.81	40.81
80	-8.04	-3.70	32.65
81	-7.07	-3.01	28.92
82	-6.10	-2.32	25.20
83	-5.28	-2.21	22.01
84	-4.45	-2.10	18.81
85	-3.04	-1.23	16.22

Table B.1: Continued

Percent of gait cycle [%]	Right buffer force for internal-external* torque [N]	Left buffer force for internal-external* torque [N]	Total anterior-posterior* buffer force [N]
86	-1.63	-0.36	13.63
87	-2.72	-1.37	11.91
88	-3.81	-2.39	10.20
89	-4.42	-2.80	6.27
90	-5.04	-3.21	2.33
91	-4.99	-3.30	-0.54
92	-4.95	-3.40	-3.41
93	-4.44	-2.82	-6.74
94	-3.92	-2.24	-10.07
95	-3.76	-2.07	-14.07
96	-3.60	-1.90	-18.07
97	-2.41	-1.10	-37.99
98	-1.21	-0.30	-57.91
99	-1.55	-1.56	-100.46

* Positive direction is listed first

APPENDIX C

DISPLACEMENTS AND LOADS USED IN FINITE ELEMENT MODEL

Table C.1: Displacements and pressure applied to prosthetic knee joint within finite element simulation of the knee-simulator stance phase

Time [s]	Flexion-extension* angle [rad]	Axial pressure [Pa]	Anterior-posterior* displacement [m]	Internal-external* rotation [rad]
0.000	0.00	0.00	0.00E+00	0.00
0.001	0.01	574573.37	2.93E-04	0.04
0.005	0.02	758807.69	2.48E-04	0.03
0.015	0.03	943042.01	2.04E-04	0.02
0.025	0.04	1003305.33	3.38E-05	0.01
0.035	0.05	1063568.64	-1.36E-04	0.00
0.045	0.08	931140.98	-3.24E-04	-0.01
0.055	0.11	798713.61	-5.13E-04	-0.01
0.065	0.14	757464.35	-7.22E-04	-0.01
0.075	0.17	716215.09	-9.31E-04	-0.02
0.085	0.19	898132.84	-6.86E-04	-0.02
0.095	0.22	1080050.30	-4.42E-04	-0.02
0.105	0.23	1251664.80	-1.75E-06	-0.02
0.115	0.25	1423279.29	4.38E-04	-0.02
0.125	0.26	1483331.36	9.35E-04	-0.01
0.135	0.27	1543383.73	1.43E-03	-0.00
0.145	0.28	1483390.68	1.84E-03	0.01
0.155	0.28	1423397.34	2.24E-03	0.02
0.165	0.28	1286826.04	2.41E-03	0.03
0.175	0.28	1150254.59	2.58E-03	0.04
0.185	0.28	1011667.75	2.63E-03	0.05
0.195	0.28	873080.92	2.67E-03	0.05
0.205	0.27	758223.67	2.68E-03	0.06
0.215	0.26	643366.12	2.68E-03	0.06
0.225	0.25	589843.93	2.67E-03	0.07
0.235	0.24	536321.45	2.67E-03	0.07
0.245	0.23	519996.30	2.61E-03	0.08
0.255	0.22	503671.15	2.55E-03	0.08
0.265	0.20	513992.90	2.46E-03	0.09
0.275	0.19	524314.65	2.37E-03	0.10
0.285	0.17	550153.11	2.25E-03	0.11
0.295	0.15	575991.57	2.13E-03	0.12
0.305	0.14	631892.46	2.10E-03	0.12
0.315	0.13	687793.49	2.06E-03	0.13
0.325	0.12	751787.72	2.04E-03	0.13
0.335	0.12	815781.51	2.02E-03	0.13
0.345	0.11	884082.54	1.98E-03	0.13
0.355	0.11	952383.58	1.95E-03	0.13
0.365	0.10	1022431.95	1.93E-03	0.12
0.375	0.10	1092480.47	1.90E-03	0.12
0.385	0.10	1159980.77	1.92E-03	0.12
0.395	0.10	1227480.77	1.93E-03	0.12

Table C.1: Continued

Time [s]	Flexion-extension* angle [rad]	Axial pressure [Pa]	Anterior-posterior* displacement [m]	Internal-external* rotation [rad]
0.405	0.10	1292960.65	1.97E-03	0.12
0.415	0.11	1358440.53	2.02E-03	0.12
0.425	0.12	1406592.75	2.07E-03	0.12
0.435	0.13	1454744.97	2.12E-03	0.12
0.445	0.15	1467568.94	2.14E-03	0.12
0.455	0.18	1480392.90	2.16E-03	0.12
0.465	0.20	1455757.84	2.06E-03	0.12
0.475	0.23	1431122.63	1.96E-03	0.13
0.485	0.26	1281214.05	1.81E-03	0.13
0.495	0.30	1131305.33	1.66E-03	0.14
0.505	0.33	977212.87	1.55E-03	0.15
0.515	0.37	823120.41	1.44E-03	0.16
0.525	0.41	707674.85	1.18E-03	0.17
0.535	0.45	592229.14	9.15E-04	0.18
0.545	0.49	512082.69	5.18E-04	0.20
0.555	0.53	431935.95	1.23E-04	0.21
0.565	0.58	373453.55	-2.33E-04	0.21
0.575	0.62	314971.01	-5.88E-04	0.21
0.585	0.67	260915.38	-5.11E-04	0.19
0.595	0.71	206859.91	-4.35E-04	0.18
0.605	0.75	162385.21	1.99E-04	0.16

* Positive direction is listed first

APPENDIX D

FINITE ELEMENT ANALYSIS STRESS RESULTS FOR TIBIAL INSERT

Table D.1: Maximum von Mises stress results in the tibial insert, with UHMWPE modeled using a linear elastic material model, for the twenty output frames during the finite element simulation of the prosthetic knee joint components during the stance phase of walking gait.

Time [s]	Maximum von Mises stress including surface maxima [MPa]	Maximum subsurface von Mises stress, medial condyle [MPa]	Maximum subsurface von Mises stress, lateral condyle [MPa]
0	0	0	0
0.0305	70.72	43.81	38.45
0.0610	39.73	39.73	32.41
0.0915	60.17	60.17	31.39
0.1220	74.41	74.41	39.86
0.1525	64.01	64.01	50.61
0.1830	61.97	61.97	42.47
0.2135	79.81	59.98	35.89
0.2440	86.49	53.11	32.22
0.2745	87.18	60.35	30.15
0.3050	88.84	63.23	35.73
0.3355	114.7	69.52	36.96
0.3660	116.5	73.32	40.47
0.3965	129.3	75.85	44.46
0.4270	126.6	76.13	49.28
0.4575	121.6	74.02	51.38
0.4880	124.7	73.69	41.64
0.5185	133.5	76.66	33.12
0.5490	141.6	79.82	21.69
0.5795	141.8	58.35	15.36
0.6100	142.0	39.58	19.57

Table D.2: Maximum von Mises stress results in the tibial insert, with UHMWPE modeled using a linear viscoelastic material model, for the twenty output frames during the finite element simulation of the prosthetic knee joint components during the stance phase of walking gait.

Time [s]	Maximum von Mises stress including surface maxima [MPa]	Maximum subsurface von Mises stress, medial condyle [MPa]	Maximum subsurface von Mises stress, lateral condyle [MPa]
0	0	0	0
0.0305	70.00	45.09	40.49
0.0610	43.50	40.09	43.50
0.0915	72.11	60.16	32.10
0.1220	74.60	74.60	40.67
0.1525	85.35	62.91	44.94
0.1830	84.87	64.44	40.22
0.2135	85.78	60.53	35.60
0.2440	83.40	50.61	22.10
0.2745	84.24	64.76	28.65
0.3050	86.07	58.85	30.93
0.3355	84.65	69.07	38.61
0.3660	83.50	73.70	39.91
0.3965	331.60	76.82	46.12
0.4270	334.80	74.70	48.17
0.4575	338.30	72.16	47.41
0.4880	317.30	73.13	40.23
0.5185	316.00	76.73	29.25
0.5490	313.40	79.75	20.68
0.5795	312.60	62.75	15.21
0.6100	311.30	40.23	19.07